Univerzita Karlova v Praze
Matematicko-fyzikální fakulta

DISERTAČNÍ PRÁCE

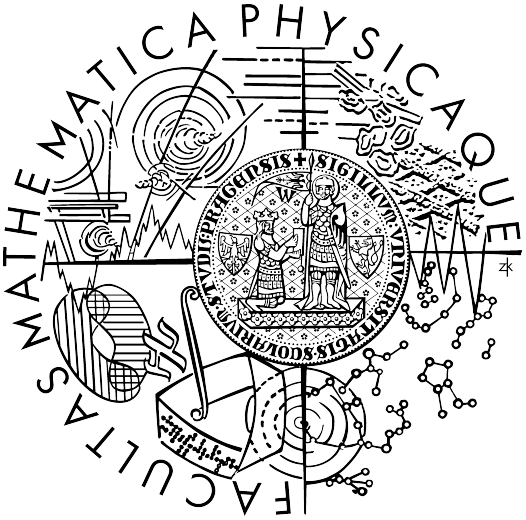

Pavel Cahyna

DIFUZE ČÁSTIC Z TOKAMAKU VLIVEM STOCHASTIZACE MAGNETICKÝCH SILOČAR

Vedoucí disertační práce : Doc. Ing. Ladislav Krlín, DrSc.
Studijní program: fyzika
Studijní obor: teoretická fyzika, astronomie a astrofyzika (F1)

Charles University in Prague
Faculty of Mathematics and Physics

PhD THESIS

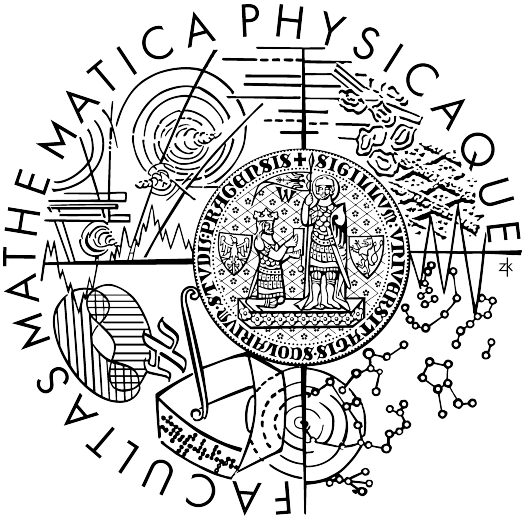

Pavel Cahyna

DIFFUSION OF PARTICLES FROM TOKAMAK BY STOCHASTIZATION OF MAGNETIC FIELD LINES

Thesis supervisor : Doc. Ing. Ladislav Krlín, DrSc.

I would like to thank everybody who helped me during my study and the research which led to this thesis. Especially my parents who supported me, my supervisor Ladislav Krlín for all his generous effort which made this thesis possible, the former head of the tokamak department at the Institute of Plasma Physics Jan Stöckel and the current head and my consultant Radomír Pánek for their deep interest in my work and the constant inspiration and invaluable help with all the scientific and administrative issues. All other colleagues at IPP Prague deserve thanks for having helped me and creating a friendly work environment. International collaboration, in particular with Marina Becoulet and Eric Nardon from CEA Cadarache, was essential to my work. Sharing of their numerical codes was an important help and is deeply appreciated, as well as the introduction into the field of magnetic perturbations that they gave me, and the numerous enlightening discussions with Eric which provided an invaluable source of inspiration.

Prohlašuji, že jsem svou disertační práci napsal samostatně a výhradně s použitím citovaných pramenů. Souhlasím se zapůjčováním práce.

Contents

Název práce: Difuze částic z tokamaku vlivem stochastizace magnetických siločar
Autor: Pavel Cahyna
Školicí pracoviště: Ústav fyziky plazmatu AV ČR, v.v.i.
Vedoucí disertační práce: Doc. Ing. Ladislav Krlín, DrSc., Ústav fyziky plazmatu
e-mail vedoucího: krlin@ipp.cas.cz
Abstrakt: Práce shrnuje současný stav výzkumu termojaderné fúze s magnetickým udržením a popisuje možnou roli stochastizace magnetických siločar a magnetických perturbací při řešení některých problémů, se kterými se využití fúze potýká. Podává teoretický úvod do problematiky deterministického chaosu a vysvětluje souvislost této teorie s magnetickými perturbacemi v tokamaku. Výsledky jsou prezentovány převážně formou publikací v časopisech a sbornících. Patří mezi ně: srovnání chaotické difuze siločar a částic, kde byly nalezeny podstatné rozdíly, aplikace chaotické difuze částic na problém relativistických elektronů vznikajících při disrupcích, kde naše simulace přispěly k vysvětlení experimentálních výsledků z tokamaku JET, výpočet spekter perturbací a stochastizace siločar pro tokamak COMPASS, sloužící jako příprava na budoucí experimenty, a modelování stínění perturbací plazmatem, kde se pozorování tzv. otisků (footprints) na divertoru ukazuje být slibnou metodou pro detekci stínění.
Klíčová slova: tokamak, deterministický chaos, magnetické ostrovy, okrajově lokalizovaný mód (edge localized mode).

Title: Diffusion of particles from tokamak by stochastization of magnetic field lines
Author: Pavel Cahyna
Tutoring institution: Institute of plasma physics AS CR, v.v.i.
Supervisor: Doc. Ing. Ladislav Krlín, DrSc., Institute of plasma physics
Supervisor's e-mail address: krlin@ipp.cas.cz
Abstract: The thesis summarizes the current state of research of thermonuclear fusion with magnetic confinement and decribes the possible role of stochastization of magnetic field lines and magnetic perturbations in solving some of the problems that are encountered on the road to the exploitation of fusion. It presents a theoretical introduction to deterministic chaos and explains the connection of this theory to magnetic perturbations in tokamak. The results are presented mainly in the form of publications in journals and conference proceedings. Among them are: the comparison of chaotic diffusion of particles and field lines, where significant differences were found; the application of chaotic diffusion of particles to the problem of runaway electrons originating in disruptions, where our simulations contributed to explaining the experimental results from the JET tokamak; the calculation of spectra of perturbations for the COMPASS tokamak, done as a preparation for the upcoming experiments; and modelling of screening of perturbations by plasma, where the observations of divertor footprints show as a promising method to detect the screening.
Keywords: tokamak, deterministic chaos, magnetic islands, edge localized mode

Part I

Background

Chapter 1

Introduction

1.1 Thermonuclear fusion — nuclear power from plasma[1]

Controlled fusion of light nuclei, if mastered, would be one of the best methods of energy production. Compared to chemical reactions (burning of fossil fuels) it has the advantage of much higher energy density: the most favorable reaction of deuterium and tritium nuclei releases 17.6 MeV for a single reaction, or 338×10^6 MJ for a kilogram of fuel, above million times more than burning of oil. This advantage is shared with fission of heavy nuclei like uranium which provides similar amount of energy per unit of fuel. Compared to fission fusion has several other important advantages:

- Fusion reactions are inherently safe because, unlike fission, they are not chain reactions so there is no risk of a runaway reaction and explosion.
- Fission reaction uses uranium, which is a fairly rare element, while for fusion there is a nearly limitless supply of deuterium in water. The most favorable deuterium-tritium reaction would be limited by the supply of lithium which would be used to produce the required tritium. Still, the estimated reserves of lithium would suffice for tens thousands years of extensive exploitation of fusion energy.
- Fusion reactions do not produce long-living radioactive waste which is a serious concern for fission. The only waste is the result of irradiation of reactor components and its lifetime can be minimized by the choice of materials. The ultimate product of the deuterium-tritium reaction is just helium.

[1] This section follows mainly the derivations in [21].

A fusion reaction involves two nuclei while a fission of a nucleus is triggered by a neutron – a neutral particle. This difference has fundamental implications for the design of fusion reactors. The neutron can reach the nucleus easily and thus a fission reaction is fairly easy to achieve. In contrast for a fusion reaction the nuclei must overcome the repulsive Coulomb force before they approach enough for the strong nuclear force to take over and make the reaction happen. A crude estimate of the required kinetic energy can be done classically by evaluating the electrostatic potential energy at the distance of the nuclei where the attractive strong nuclear force overcomes the Coulomb force. This estimate gives 288 keV for the deuterium-tritium reaction. In practice the quantum effects can not be neglected at this scale and thanks to the tunneling effect reaction can happen even for lower energies. The reaction rate is proportional to the square of density n and the product of velocity v and the cross-section of the reaction σ. This quantity has to be averaged over the velocity distribution (the averaging is denoted by angle brackets) to obtain the total reaction rate per unit of volume:

$$R \propto n^2 \langle v\sigma \rangle. \tag{1.1}$$

The deuterium-tritium (D-T) reaction is preferable because it has by far the largest cross-section σ among the reactions of light nuclides. For a Maxwell distribution of particle velocities the D-T reaction rate has a maximum at a temperature of 70 keV[2], where most of the reactions occur for particles from the tail of the energy distribution. At this temperature (about 8×10^8 K) the light elements exist only in a ionized state – plasma, as the corresponding energy is much higher than the ionization energy. The operation of fusion reactors is thus governed by plasma physics.

To maintain the required temperature the fusion plasma will need a source of energy to compensate the thermal losses. The energy source can be either external (induction of current, heating by microwaves or injection of energetic particles) or internal – the fusion reactions themselves. This energy will be used to compensate the inevitable loss of energy from the plasma associated with the enormous temperature gradient from the temperature in the plasma core needed for the fusion reactions down to the temperature of the solid structures of the reactor. It follows that the plasma must have a very low thermal conductivity in order to minimize this loss and make a practical fusion reactor possible. We will note this loss as P_κ in the following discussion.

For a fusion energy source it is necessary to make the fusion output power significantly larger than the input power of the external heating sources. This

[2]As usual in fusion, temperature is given in the units of energy: T [J] $= k_\mathrm{B}T$ [K], T [eV] $= k_\mathrm{B}/e \cdot T$ [K] where k_B is the Boltzmann constant and e the value of elementary charge in Coulombs.

is quantified by the fusion gain factor Q defined as the ratio of the fusion power to the input power:

$$Q = \frac{P_{\text{fus}}}{P_{\text{in}}}. \tag{1.2}$$

If the fusion power is sufficiently high, it can heat the plasma itself, thus the external heating can be switched off and $Q = \infty$. This condition is called *ignition*. An economically viable fusion reactor shall have the fusion power close to ignition, with Q on the order of 30 or more so that the fusion power, taking into account all the losses associated with power conversion (thermal to electric and electric to the beams or electromagnetic waves used to heat the plasma) is able to supply the input power P_{in} and enough net power remains as the output of the power plant.

As a concrete example we will take again the D-T reaction

$$\text{D} + \text{T} \longrightarrow \alpha + \text{n} + 17.6 \text{ MeV}.$$

The kinetic energies of the reaction products are inversely proportional to their masses, so the neutron carries away 4/5 of the energy and the alpha particle 1/5. The neutron can escape the plasma freely – it is not bound by the electromagnetic field that is used to confine the plasma, nor it interacts with the charged particles. The fact that 4/5 of fusion output is carried by fast neutrons has profound implications for the construction of the reactor. The first wall will have to sustain this high neutron flux which is damaging to the structure of materials and creates radioactive nuclides. Behind the first wall a blanket will capture the neutrons and protect the rest of the plant from them. It will also convert their energy to thermal and provide the heat to the conventional steam turbines of the power plant. Another important function of the blanket will be the breeding of the required tritium by nuclear reactions of the incoming neutrons with lithium.

Only the alpha particles remain in the plasma and are available to supply the energy to maintain its temperature. The losses of energy from the plasma are equal to the external input plus the alpha power: $P_{\text{in}} + P_\alpha = P_\kappa$ and we have seen that $P_\alpha = P_{\text{fus}}/5$. In the fusion gain (1.2) we can substitute for P_{in}:

$$Q = \frac{P_{\text{fus}}}{P_\kappa - P_{\text{fus}}/5}. \tag{1.3}$$

It is clear that to maximize Q one has to minimize the losses P_κ and maximize the fusion power P_{fus}. This can be formulated as a requirement on the plasma parameters. The global parameter corresponding to the losses is the energy confinement time τ_{e}. If the thermal losses are proportional to the temperature gradient, thus (for a given density) to the stored energy in the plasma, the

plasma temperature and its energy would fall exponentially if power sources are absent. The energy confinement time τ_e is defined as the time constant of the exponential decrease. The losses P_κ are inversely proportional to τ_e:

$$P_\kappa = \frac{VU}{\tau_\mathrm{e}} \tag{1.4}$$

where U is the plasma energy per unit of volume V. If we normalize all the power-related quantities per unit of volume, thus defining power densities $S_\kappa \equiv P_\kappa/V$, $S_\mathrm{fus} \equiv P_\mathrm{fus}/V$ etc., we may use the relation between plasma pressure p and the energy density U:

$$U = \frac{3}{2}p \tag{1.5}$$

to express S_κ in terms of pressure:

$$S_\kappa = \frac{3p}{2\tau_\mathrm{e}}. \tag{1.6}$$

According to (1.1), the fusion power density S_fus is proportional to the square of density[3] n, which is related to the total pressure p:

$$p = 2nT. \tag{1.7}$$

The relations (1.6) and (1.7) allow us to rewrite (1.3) using the pressure p:

$$Q = \frac{K_\mathrm{fus} p^2 \frac{\langle\sigma v\rangle}{T^2}}{\frac{3p}{2\tau_\mathrm{e}} - \frac{K_\mathrm{fus}}{5} p^2 \frac{\langle\sigma v\rangle}{T^2}}. \tag{1.8}$$

The quantity $\langle\sigma v\rangle/T^2$ is a function of temperature only. Its maximum determines the optimum temperature for the reaction. For the D-T reaction the maximum is reached at $T_\mathrm{min} = 15$ keV. The condition for ignition is

$$p\tau_\mathrm{e} \geq \frac{15}{2K_\mathrm{fus}} \frac{T^2}{\langle\sigma v\rangle},$$

it sets the critical required value of the product $p\tau_\mathrm{e}$, which is minimized for $T = T_\mathrm{min}$. The actual value at this temperature is $p\tau_\mathrm{e} = 8.3$ atm.s.

The derivation summarized above assumed that the losses of energy from the plasma are all thermal conductive losses P_κ, proportional to the temperature gradient. In reality there are also radiative Bremsstrahlung losses P_B associated with the collisions of charged particles in the plasma. Their scaling with temperature is different: $P_\mathrm{B} \propto T^{1/2}$ for a given density. In the regime of interest the thermal losses dominate over the Bremsstrahlung losses, which justifies our approach.

[3]Density is electron density (number of electrons per unit of volume) unless stated otherwise. The total density of particles (electrons and ions) is $2n$ for a plasma consisting of hydrogen isotopes.

1.2 Scope of this work

The present thesis explores several examples of application of deterministic chaos to fusion plasmas. The unifying theme is chaos arising from small non-axisymmetric perturbations of the originally symmetric fusion plasma configuration – the tokamak. This situation corresponds to the nearly integrable Hamiltonian dynamical systems studied in the chaos theory. The symmetric tokamak equilibrium corresponds to an integrable system and the perturbation causes non-integrability, however it is considered small enough that a perturbative approach is justified. The general theory of integrable and nearly-integrable Hamiltonian dynamical systems is summarized in Appendix A.

A particular attention is given to the case when the perturbation is introduced artificially to exploit its beneficial effects. A strong motivation is the recent installation of the tokamak COMPASS in IPP Prague. COMPASS is equipped with a set of coils which can create non-axisymmetric perturbations and a large part of this thesis is dedicated to preparation of experiments with these coils. Many results are however generally applicable to devices with similar coil systems.

The following sections will introduce the tokamak – the most advanced concept of a fusion reactor. It will be shown what is the role of deterministic chaos in solving some of the problems that tokamaks face on the road to achieving the basic requirements of a working fusion power source, given in section 1.1. The author's own results will be presented mainly in the form of published papers with comments.

Chapter 2

Magnetic confinement and the tokamak

In section 1.1 it was shown how obtaining a net power from fusion requires conditions at (or close to) ignition, which is reached when $p\tau_e \geq 8.3$ atm.s at a temperature close to $T = 15$ keV. There are two ways to achieve this goal:

- *Inertial confinement fusion* which seeks to maximize p by maximizing the density n. The high pressure leads to rapid instabilities and the quickly expanding plasma is maintained for some time only thanks to its inertia. The whole process is inherently non-stationary and explosive and the confinement time is very short. The plasma must be compressed into the initial high-density state by powerful energy sources such as lasers. An example of inertial confinement fusion is the hydrogen bomb where a nuclear (fission) bomb is used for this purpose. For electric power generation the pulsed operation is a disadvantage, another one is the poor efficiency of lasers used to start the reaction.

- *Magnetic confinement fusion* which aims at achieving a stable, ideally steady state plasma. This requirement sets the limit on the pressure p which must be low enough to not cause instabilities. The typical pressure is at the order of 1 atm and energy confinement time at the order of 1 s. This is the most developed road to fusion energy.

In the magnetic confinement fusion a magnetic field is used to confine the plasma. It is able to do so because, as will be shown in section 2.1, the charged particles in the plasma are constrained to follow the magnetic field lines. In this way it is possible to prevent the plasma from being lost by touching the wall of the vessel of the reactor. Plasma still can escape along the field lines and a linear device with straight magnetic field lines would

lose the plasma at its ends. It is thus necessary to bend the field lines into a toroidal shape where they stay inside the vessel and never intersect its wall. The basic configuration of a magnetic confinement fusion experiment is a toroidal plasma ring around a central axis, called the major axis. Any plane containing the major axis and intersecting the plasma column is called a poloidal plane. The angle around the major axis is called the toroidal angle ϕ and specifies the position of a given point along the plasma ring. In a poloidal plane one may introduce two coordinates. The simplest choice is (R, Z) where the major radius R is the distance from the major axis while Z is the vertical position relative to a plane perpendicular to the major axis and passing through the center of the vessel (the midplane). (R, ϕ, Z) form together a cylindrical coordinate system.

If one field line is followed for many toroidal turns, it will eventually either cover a 2-D surface or densely fill a 3-D volume. In the second case the plasma parameters (like density, temperature, pressure) can be expected to stay approximately constant across this 3-D volume because by following the field lines the particles can get from any point in the volume to the vicinity to any other point. In the first case the plasma parameters will stay constant only on the surface, which will act as a barrier to the transport of energy and particles. The first case is clearly preferable for achieving a long energy confinement time τ_{e}. Magnetic confinement fusion devices shall thus have their magnetic field forming a set of toroidal, nested magnetic surfaces in most of the plasma volume. The detailed requirements of the magnetic configuration are among others determined by the properties of single particle motion which are briefly summarized below.

2.1 Charged particle motion in a magnetic field

In a magnetic field $\vec{\mathbf{B}}$, a particle with mass m, charge q and speed $\vec{\mathbf{v}}$ is subject to the Lorentz force $\vec{\mathbf{F}} = q\vec{\mathbf{v}} \times \vec{\mathbf{B}}$. As the force is always perpendicular to the field lines and the particle velocity, the particle rotates around the field line on a helix with angular frequency (the *cyclotron frequency* or *Larmor frequency*)[1] $\omega_c = qB/m$. The particle velocity can be decomposed in the component parallel to the field, which is not affected by the Lorentz force, and the component perpendicular to the field: $\vec{\mathbf{v}} = \vec{\mathbf{v}}_{\parallel} + \vec{\mathbf{v}}_{\perp}$. The radius of the circle the particle makes in the plane perpendicular to the field (the *Larmor radius*) is $r_{\mathrm{L}} = mv_{\perp}/(|q|B)$. The center of the circle is known as

[1] The sign of ω_c expresses the direction of the rotation, which depends on the sign of q.

the *guiding center* and the particle motion in a homogeneous magnetic field can be described as gyration around the guiding center with the Larmor frequency ω_c while the guiding center moves along the field line with the velocity $v_\parallel$.

In a non-uniform magnetic field or in the presence of an electric field the guiding center motion does not follow exactly the field lines. There are several contributions to the drift motion of the guiding centers across the magnetic field, among them:

- $\vec{\mathbf{E}} \times \vec{\mathbf{B}}$ drift in the electric field with the drift speed

$$\vec{\mathbf{v}}_{E\times B} = \frac{\vec{\mathbf{E}} \times \vec{\mathbf{B}}}{B^2}. \tag{2.1}$$

  It is a flow of the whole plasma because it is the same for all the particles.

- Curvature drift when the magnetic field lines are not straight, with the drift speed

$$\vec{\mathbf{v}}_r = \frac{v_\parallel^2}{\omega_c} \frac{\vec{\mathbf{R}} \times \vec{\mathbf{B}}}{BR^2} \tag{2.2}$$

  where the vector $\vec{\mathbf{R}}$ is the radius of curvature of the field lines.

- Gradient B drift in an inhomogeneous field, with the drift speed

$$\vec{\mathbf{v}}_{\nabla B} = \frac{v_\perp^2}{2\omega_c} \frac{\vec{\mathbf{B}} \times \nabla B}{B^2} \tag{2.3}$$

In addition, it can be shown that the magnetic moment $\mu \equiv m v_\perp^2/(2B)$ is an approximate constant of motion (it is a conserved quantity when the variation of field is slow compared to the Larmor frequency). The kinetic energy $E = m(v_\parallel^2 + v_\perp^2)/2$ is also a constant of motion, so for a field whose strength increases along the field lines, a particle coming along a field line in the direction of ∇B with a given E and μ may arrive to the point where all its energy is in the perpendicular velocity $v_\perp$ and $v_\parallel = 0$. This happens when $B = E/\mu$. At this point the particle stops and is reflected back to the region of weaker field.

2.2 Safety factor

Consider now a very simple toroidal magnetic confinement device with purely toroidal magnetic field produced by coils wound around the vacuum chamber.

The field lines form simple horizontal circles, so it is a degenerate case of magnetic surfaces, where a field line does not densely cover a surface but rather closes on itself. This configuration does not really confine the plasma because of the drift motions. If there are no significant currents in the plasma contributing to the toroidal field, the toroidal field decreases with the distance R from the main axis of symmetry of the torus as $B \propto 1/R$. (The inner side of the torus is thus known as the *high field side (HFS)* and the outer side as the *low field side (LFS)*.) This dependence causes a grad B drift $\vec{\mathbf{v}}_{\nabla B}$ (2.3). R is at the same time the radius of curvature of the field line and the drift from field curvature (2.2) is present in addition to the grad B drift. From $\nabla \times \vec{\mathbf{B}} = 0$ one can derive the relation between the curvature of field lines and the gradient of the field: $(\nabla B)/B = -\vec{\mathbf{R}}/R^2$. The total drift is then:

$$\vec{\mathbf{v}}_{\nabla B} + \vec{\mathbf{v}}_r = \frac{1}{\omega_c} \frac{\vec{\mathbf{R}} \times \vec{\mathbf{B}}}{BR^2} \left(v_\parallel^2 + \frac{1}{2} v_\perp^2 \right) \tag{2.4}$$

The $\vec{\mathbf{v}}_r$ and $\vec{\mathbf{v}}_{\nabla B}$ drift velocities are vertical and from (2.4) it can be seen that they have the same direction for every particle species, so the total drift $\vec{\mathbf{v}}_r + \vec{\mathbf{v}}_{\nabla B}$ is always nonzero. For electrons this total drift is in the opposite direction than for ions because of the charge dependence in (2.4). This will lead to a vertical separation of electrons and ions and the appearance of a vertical electrical field. The resulting $\vec{\mathbf{E}} \times \vec{\mathbf{B}}$ drift (2.1) will be horizontal and will eject the plasma outwards to the wall of the chamber.

To eliminate this instability, the field lines may be helically twisted to connect the regions of opposite charge at the top and the bottom of the plasma. Particles may return along the field lines and eliminate the voltage created by the charge separation. This way a return current is produced, called *Pfirsch-Schlüter current*.

In the center of the plasma there is one circular field line at a major radius R_0, called the *magnetic axis*. Around the magnetic axis there are nested magnetic surfaces, covered by the helical field lines.

To twist the field lines a field component perpendicular to the toroidal field is required, called the *poloidal field* B_P. The twisting of field lines can be expressed using the *safety factor* q defined as the number of toroidal turns of the field line after whose the field line returns to the starting position in a poloidal plane (makes one poloidal turn around the magnetic axis). However it does not necessarily return to the poloidal plane at the same toroidal position – this happens only if q is an integer. If q is a rational number, $q = m/n$ for m, n integers, the field line will return to the same point in the starting plane after m toroidal and m poloidal turns. If q is irrational, the field line will never return to the same position in space and will densely

cover the whole magnetic surface. The safety factor is by its construction a function of the magnetic surface. Surfaces with a rational value of q are called rational surfaces. Rational surfaces with low values of m and n are important because many plasma instabilities develop on them.

If we follow a field line on one full poloidal turn around the magnetic axis and note ϑ the angle in the poloidal plane with respect to the magnetic axis, the distance $\Delta\phi$ in the toroidal direction the field line traverses is

$$\Delta\phi = \int_0^{2\pi} \frac{\vec{\mathbf{B}} \cdot \nabla\phi}{\vec{\mathbf{B}} \cdot \nabla\vartheta} \,\mathrm{d}\vartheta \tag{2.5}$$

where the integral is taken along the field line. By the definition of the safety factor $q = \Delta\phi/(2\pi)$.

If the configuration is toroidally symmetric, the integral along a field line in (2.5) can be replaced by an integral along a closed curve in a poloidal plane because there is no ϕ dependency:

$$q = \frac{1}{2\pi} \oint \frac{\vec{\mathbf{B}} \cdot \nabla\phi}{\vec{\mathbf{B}} \cdot \nabla\vartheta} \,\mathrm{d}\vartheta. \tag{2.6}$$

The term $\vec{\mathbf{B}} \cdot \nabla\phi$ corresponds to the toroidal field: $\vec{\mathbf{B}} \cdot \nabla\phi = B_\mathrm{T}/R$. The term $\vec{\mathbf{B}} \cdot \nabla\vartheta$ corresponds to the poloidal field: $\vec{\mathbf{B}} \cdot \nabla\vartheta = B_\mathrm{P}\,\mathrm{d}\vartheta/\,\mathrm{d}l$ where l is the distance along the magnetic surface in the poloidal plane ($\int_0^{2\pi} \mathrm{d}l/\,\mathrm{d}\vartheta \;\mathrm{d}\vartheta$ is the circumference of the surface). Substituting into (2.6) gives

$$q = \frac{1}{2\pi} \oint \frac{B_\mathrm{T}}{RB_\mathrm{P}} \frac{\mathrm{d}l}{\mathrm{d}\vartheta} \,\mathrm{d}\vartheta. \tag{2.7}$$

The integral (2.7) can be simplified by taking the toroidal field term as approximately constant: $B_\mathrm{T}/R \approx B_0/R_0$, where $B_0 \equiv B_\mathrm{T}(R_0)$ is the value of the toroidal field B_T at the magnetic axis. Moreover, if we consider flux surfaces with an approximately circular cross section with a distance r from the magnetic axis and a constant poloidal field, then $B_\mathrm{P}\,\mathrm{d}\vartheta/\,\mathrm{d}l \approx B_\mathrm{P}/r$. We obtain

$$q \approx \frac{rB_0}{R_0 B_\mathrm{P}}. \tag{2.8}$$

The poloidal field is linked to the current I flowing in the plasma inside the flux surface: $B_\mathrm{P} = \mu_0 I/(2\pi r)$, so

$$q \approx \frac{2\pi r^2 B_0}{\mu_0 R_0 I}. \tag{2.9}$$

It follows that in order to have helically twisted field lines, corresponding to a finite q, there must be a nonzero toroidal current I in the plasma.

The distance of the plasma edge from the magnetic axis is called the *minor radius* a. The value R_0/a is called the *aspect ratio*. The foregoing approximations were derived using the assumption of large aspect ratio, or small inverse aspect ratio $\varepsilon \equiv a/R_0$. This is an often used assumption in magnetic fusion theory.

The magnetic confinement device with toroidal symmetry, significant toroidal current I and toroidal field B_T imposed by coils around the vessel is called the *tokamak*. Its safety factor is at the order of unity, so according to (2.8) the poloidal field is smaller than the toroidal field by an order of ε.

The toroidal current in the tokamak is traditionally formed by varying the magnetic flux through the torus, as in a transformer. In order to allow steady-state operation, another solution which does not involve time-varying fields will have to be used. Another drawback is the energy stored in this current, which has a potential to cause instabilities. If an instability abruptly terminates the plasma (a so-called *disruption*), the current can not flow anymore, but the release of the huge magnetic energy associated with it can cause damage to the tokamak structures.

2.3 Stellarators and 3D fields

If we want to obtain a configuration with twisted field lines but without the toroidal current which complicates the tokamak, the toroidal symmetry has to be abandoned. The passage from the field line integral (2.5) to the integral along a closed contour in the poloidal plane (2.6) is then not valid and a finite value of the safety factor q (or equivalently a nonzero value of the *rotational transform* $\iota \equiv 2\pi/q$ which is the poloidal angle the field line performs in one toroidal turn) may exist even with $I = 0$. The nonaxisymmetric field required for the rotational transform is produced by three-dimensional shaping of the coils and/or different coils along the torus. The complexity of those coils is a disadvantage in comparison to the tokamak, whose toroidal field coils are planar (each coil lying in one poloidal plane) and all identical. Another disadvantage is the complexity of the magnetic field and the associated complexity of modelling a stellarator. In a tokamak many problems can be reduced to two dimensions thanks to the symmetry. In particular, the symmetry of a tokamak automatically ensures the existence of magnetic surfaces (see section 4). This is not the case for a stellarator whose magnetic field has to be carefully optimized to form magnetic surfaces in most of the volume. An analogous issue arises with the particle orbits. Due to the drifts mentioned in the previous section, the particle orbits deviate from the magnetic surfaces. Thanks to the symmetry of the tokamak, the particle orbits

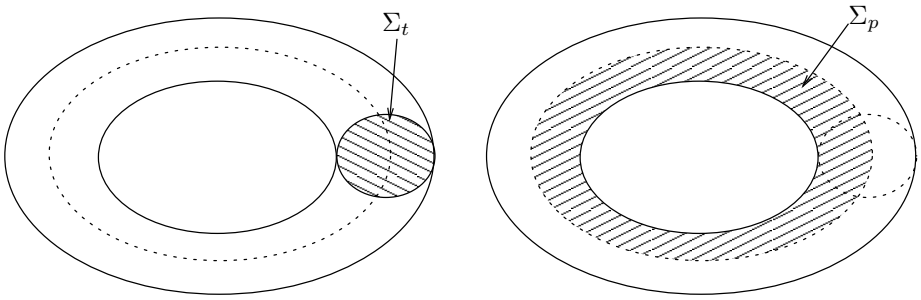

(a) toroidal flux (b) poloidal flux

Figure 2.1: Definition of the flux functions.

are closed, which is not a priori guaranteed for a stellarator, where a particle might drift from the plasma completely [22]. The modern stellarators are again optimized to minimize this effect. If the tokamak field deviates from perfect symmetry, many of the stellarator issues apply to it too.

2.4 Magnetic fluxes

When magnetic surfaces are present, they allow to define functions which express the fluxes of magnetic field through the surfaces [23]. One such function is the toroidal flux Φ_t, defined as the flux of the toroidal field $\vec{\mathbf{B}}_\mathrm{T}$ through the inside of a magnetic surface, i.e. as the surface integral

$$\Phi_\mathrm{t} \equiv \frac{1}{2\pi} \int_{\Sigma_t} \vec{\mathbf{B}}_\mathrm{T} \cdot \mathrm{d}\vec{\mathbf{S}} \tag{2.10}$$

where the surface Σ_t (Fig. 2.1a) is the part of the poloidal plane delimited by the given magnetic surface.

Analogously the poloidal flux ψ is defined as the flux of the poloidal field $\vec{\mathbf{B}}_\mathrm{P}$ through the surface Σ_p reaching from the magnetic axis up to the chosen magnetic surface (Fig. 2.1b) :

$$\psi \equiv \frac{1}{2\pi} \int_{\Sigma_p} \vec{\mathbf{B}}_\mathrm{P} \cdot \mathrm{d}\vec{\mathbf{S}}. \tag{2.11}$$

Both Φ_t and ψ are conventionally defined as fluxes per radian, this is the reason for the division by 2π in the defining formulae. They depend only on the choice of a magnetic surface by definition, i.e. they are constant functions on every magnetic surface. As such they can be used to label

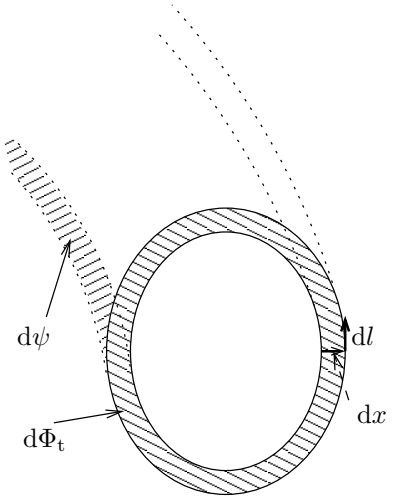

Figure 2.2: The differentials of the flux functions. According to [23].

magnetic surfaces (which are often called flux surfaces). This is useful for arbitrary, non-circular magnetic surfaces, as the distance r from the magnetic axis is constant only on circular surfaces. Sometimes the fluxes normalized to their value at the edge are used for this purpose, e.g. $\psi_N \equiv \psi/\psi_{\text{edge}}$, which then lie in the range $(0, 1)$ inside the plasma. Other option is to use square roots of the normalized fluxes: $\rho \equiv \sqrt{\Phi_\text{t}/\Phi_{\text{tedge}}}$, $s \equiv \sqrt{\psi_N}$. The reason is that those functions are close to the normalized geometric minor radius r/a in the approximation of circular magnetic surfaces.

Consider two close magnetic surfaces, separated by a distance $\mathrm{d}x$ (Fig. 2.2). The toroidal flux enclosed between them is

$$\mathrm{d}\Phi_\text{t} = \frac{1}{2\pi}\int_0^{2\pi} B_\text{T}\,\mathrm{d}x\frac{\mathrm{d}l}{\mathrm{d}\vartheta}\,\mathrm{d}\vartheta \tag{2.12}$$

where l is the same as in (2.7). The enclosed poloidal flux is

$$\mathrm{d}\psi = B_\text{P} R\,\mathrm{d}x. \tag{2.13}$$

By substituting for $\mathrm{d}x$ in (2.12) from (2.13), we obtain

$$\frac{\mathrm{d}\Phi_\text{t}}{\mathrm{d}\psi} = \frac{1}{2\pi}\int_0^{2\pi}\frac{\mathrm{d}l}{\mathrm{d}\vartheta}\frac{B_\text{T}}{B_\text{P}R}\,\mathrm{d}\vartheta$$

which is exactly the expression (2.7) for the safety factor. Thus

$$q = \frac{\mathrm{d}\Phi_\text{t}}{\mathrm{d}\psi}. \tag{2.14}$$

2.5 Divertor

Beyond a certain distance from the magnetic axis the flux surfaces must intersect the wall of the vacuum vessel. The flux surface which separates the inner closed flux surfaces and the outer flux surfaces intersecting the solid components is called the *last closed flux surface* (LCFS). The LCFS is not usually left to interact with a significant area of the wall. It is rather defined by a solid component protruding from the wall inside the vacuum vessel, called the *limiter* [23]. Beyond the LCFS there is a region of cold plasma connected by the field lines to the limiter, called the *scrape-off layer* (SOL). The limiter, being in contact with the LCFS, is the focus of the plasma-wall interaction. It must be able to withstand the high power fluxes from the inner plasma and its role is to protect the rest of the wall which can then be less tolerant to high temperatures. The disadvantage of the limiter is that it acts as a source of impurities close to the core plasma.

This disadvantage is eliminated by the *divertor*, which moves the LCFS-wall interaction far from the core plasma. The key part of the divertor is an axisymmetric coil under the plasma with a current parallel to the plasma current. At one point at the plasma edge called the *X-point* the field of this coils compensates the field of the plasma current and the total poloidal field is zero. The flux surface passing through the X-point is called the *separatrix*. The upper branches of the separatrix join together and encircle the magnetic axis, forming the LCFS. The lower branches intersect the wall in two circles, the *strike points*. Plasma particles which pass the LCFS are carried by the field lines to the vicinity of the strike points, where they deposit their energy. This area is reinforced by the divertor plates, which, like the limiters, have to sustain high power fluxes. The strike points are far from the core plasma, so any impurities released from there have less probability to diffuse to the core plasma and contaminate it.

The divertor changes significantly the edge magnetic field. Due to the null of the poloidal field in the X-point the safety factor q is infinite at the separatrix. This can be seen from (2.7) because in the X-point B_P in the denominator of the integrand is zero. Close to the separatrix q diverges logarithmically [24]. The edge profile of q can not be characterized by its value at the separatrix, as it is always infinite. Instead the value at $\psi_N = 0.95$ is conventionally used, called q_{95}.

2.6 Magnetic coordinates

Any of the surface flux functions defined in the section 2.4 can be used as a coordinate in the poloidal plane. An additional coordinate to specify the position on the magnetic surface is needed. In (2.5) we have used the geometric poloidal angle ϑ. Other choices of the poloidal angle coordinate are possible. Especially advantageous are those where the generalized poloidal angle θ^* is a linear function of ϕ along a field line:

$$q\,\mathrm{d}\theta^* = \mathrm{d}\phi. \tag{2.15}$$

The factor q ensures that θ^* is always in the range $(0, 2\pi)$ on any magnetic surface. Field lines look as straight lines when drawn in the (θ^*, ϕ) plane. The functions $\psi(R, Z), \theta^*(R, Z)$ form together a coordinate system in the poloidal plane and (ψ, θ^*, ϕ) are a complete coordinate system for the plasma. Any coordinates with the property (2.15) are called *magnetic coordinates* [25] or straight field line coordinates. The coordinate θ^* is uniquely determined by (2.15) up to an additive constant which gives the origin $\theta^* = 0$. By convention $\theta^* = 0$ at the outboard midplane. Those coordinates are called PEST coordinates [25] after the code using them [26]. Other choices of magnetic coordinates are possible by using another toroidal coordinate ϕ' instead of the geometric angle ϕ. The new toroidal coordinate differs from ϕ by an additive term which is a function of the poloidal position [25]: $\phi' = \phi + f(R, Z)$. Examples of such coordinates are the Boozer or Hamada coordinates. In this work we will use the PEST coordinates because of the simplicity arising from using the geometric toroidal angle as the toroidal coordinate.

Chapter 3

The road to a tokamak fusion reactor

As shown in the introductory section 1.1, obtaining a significant net power output from fusion in a plasma requires sufficient value of the product of pressure p and confinement time τ_e. Additional requirements come from the engineering of the reactor. In a tokamak the plasma is confined by the magnetic field which serve to limit the transport and to balance the internal pressure p. The attainable p and τ_e both scale favorably with the magnetic field, therefore the field shall be as high as possible from the engineering point of view. Mechanical load on the coils at this field is one engineering constraint of the fusion reactor. Another one comes from the neutron power flux which carries 4/5 of the power output. The blanket must be thick enough to shield the rest of the machine from the neutron irradiation, and it must be located between the plasma and the coils which will be superconductive and thus sensitive to irradiation. Nuclear physics constraints lead to an estimate of blanket thickness of about 1.2 m and the mechanical stress requires the coil thickness of about 0.8 m. The plasma minor radius shall be comparable to those values in order to obtain a favorable ratio of the volume of plasma (which determines the power output) relative to the volume of the expensive coils and blanket. It follows that a fusion reactor shall be a large device, a quantitative estimate based on the foregoing reasoning is $a \approx 2$ m, $R_0 \approx 5$ m.

The requirement on τ_e necessary to obtain a significant power amplification Q also favors a large device. The thermal flux associated with the temperature gradient can be expected to decrease with the plasma diameter. This is indeed the case, experiments show a favorable scaling of τ_e with R_0.

In the introduction it was explained how a significant power amplification Q (see (1.2)) is required for a viable fusion energy source. Even for an experimental reactor achieving high Q is desirable. Given that only 1/5 of the

fusion power remains in the plasma[1], the fraction f_α of the self-heating power of the plasma P_α to the total required heating power P_κ is (cf. equation (1.3):

$$f_\alpha \equiv \frac{P_\alpha}{P_\kappa} = \frac{1}{5}\frac{P_{\text{fus}}}{P_\kappa}. \tag{3.1}$$

In terms of the fusion gain Q we may express f_α as

$$f_\alpha = \frac{Q}{Q+5}. \tag{3.2}$$

The domain of high values of f_α needs to be explored. In this regime (*burning plasma*) plasma will be heated predominantly by its own fusion power and determine its profiles itself, as opposed to the external heating used on present devices which provides a means of control. This will be a qualitatively new regime, not an extrapolation from the present devices.

The highest Q to date was achieved on the JET tokamak, $Q = 0.62$, corresponding to $f_\alpha = 0.11$. From (3.2) it follows that one needs to achieve $Q = 5$ in order to have the plasma supply half of the needed power on its own, $f_\alpha = 0.5$. For the investigation of the burning plasma regime with $f_\alpha \geq 0.5$ an experimental reactor much more performing than JET is clearly necessary, with a significant increase in size.

In the following sections it will be discussed what problems are encountered when trying to achieve the desired power amplification. We may divide them in two areas:

- equilibrium and stability, which determine the achievable pressure p,
- transport, which sets the confinement time τ_{e}.

3.1 MHD equilibrium and stability

3.1.1 Equilibrium

The fusion plasma must be first of all in a force equilibrium in order to be maintained. Equilibrium is usually studied using the *magnetohydrodynamic (MHD)* model of plasma. Plasma is here considered as a conductive fluid in an electromagnetic field and is described by Maxwell's equations coupled with the momentum conservation equation of the fluid

$$\rho\frac{\mathrm{d}\vec{\mathbf{v}}}{\mathrm{d}t} = \vec{\mathrm{j}} \times \vec{\mathbf{B}} - \nabla p \tag{3.3}$$

[1] in the form of kinetic energy of the α particles which is eventually transferred to the rest of the plasma by collisions.

and the Ohm's law

$$\vec{\mathbf{E}} + \vec{\mathbf{v}} \times \vec{\mathbf{B}} = \eta \vec{\mathrm{j}} \tag{3.4}$$

where ρ is the plasma mass density, $\vec{\mathrm{j}}$ the current density and η the resistivity.

In the equilibrium the equation (3.3) becomes

$$\vec{\mathrm{j}} \times \vec{\mathbf{B}} = \nabla p \tag{3.5}$$

which is a force balance equation: the force originating from the pressure gradient is balanced by the electromagnetic force $\vec{\mathrm{j}} \times \vec{\mathbf{B}}$. According to (3.5) $\vec{\mathbf{B}} \perp \nabla p$, so the magnetic surfaces are also surfaces of constant pressure and $\vec{\mathrm{j}}$ is also tangent to them.

The force balance equation (3.5) can be reformulated using the Ampère's law $\mu_0 \vec{\mathrm{j}} = \nabla \times \vec{\mathbf{B}}$ and the identity $\nabla(B^2/2) = \vec{\mathbf{B}} \times (\nabla \times \vec{\mathbf{B}}) + \vec{\mathbf{B}} \cdot \nabla \vec{\mathbf{B}}$. We obtain [27]

$$\nabla_\perp \left(p + \frac{B^2}{2\mu_0} \right) - B^2 \vec{\mathbf{b}} \cdot \nabla \vec{\mathbf{b}} = 0 \tag{3.6}$$

where $\nabla_\perp$ is the perpendicular component of the gradient and $\vec{\mathbf{b}} \cdot \nabla \vec{\mathbf{b}}$ is the curvature of field lines. The pressure gradient is thus balanced by the gradient of the quantity $B^2/(2\mu_0)$ which by the analogy with pressure is called the *magnetic pressure*, and by the force originating from the curvature of field lines. The ratio of the plasma pressure p to the magnetic pressure is called *beta*: $\beta \equiv 2\mu_0 p/B^2$. Beta is related to the economic efficiency of the fusion reactor: p determines the power output while the cost increases with B since the coils are one of the most expensive parts of the tokamak.

The force balance equation must be in general solved numerically. Many tokamaks use the code EFIT to reconstruct the MHD equilibrium from the magnetic field measurements and other experimental quantities obtained during the discharge. EFIT determines the dependence of the poloidal flux $\psi(R, Z)$ and other functions describing the equilibrium, such as the toroidal field and current density.

3.1.2 Stability

Ideal and resistive MHD

If one takes a curl of the Ohm's law (3.4), one may substitute for $\nabla \times \vec{\mathbf{E}}$ from the Faraday's law

$$\nabla \times \vec{\mathbf{E}} = -\frac{\partial \vec{\mathbf{B}}}{\partial t} \tag{3.7}$$

and for $\vec{\mathrm{j}}$ from the Ampère's law, obtaining an equation of the time evolution of the magnetic field

$$\frac{\partial \vec{\mathbf{B}}}{\partial t} = \nabla \times (\vec{\mathbf{v}} \times \vec{\mathbf{B}}) + \frac{\eta}{\mu_0} \triangle \vec{\mathbf{B}}. \tag{3.8}$$

Resistivity in tokamak plasmas is very low, which justifies considering it to be zero and using only the first term. The approximation of zero resistivity is called *ideal MHD*. It can be shown that under this assumption two points which move with the plasma and are on the same field line will remain always in the plasma. In other words, field lines are carried by the plasma flow, it is said that they are *frozen in*.

If we do not neglect plasma resistivity (*resistive MHD*) and consider a situation without plasma flows, $\vec{\mathbf{v}} = 0$, we obtain from (3.8)

$$\frac{\partial \vec{\mathbf{B}}}{\partial t} = \frac{\eta}{\mu_0} \triangle \vec{\mathbf{B}} \tag{3.9}$$

which is a diffusion equation for $\vec{\mathbf{B}}$, analogous to the classical equation of heat conduction.

The conclusion is that the magnetic field is advected by the plasma flow (first term of (3.8)) and diffuses across the field with the diffusion coefficient η/μ_0 (second term of (3.8)). In the ideal MHD, the frozen-in law for magnetic field lines prohibits certain types of magnetic field evolution – the magnetic field lines can not tear and reconnect, the topology of magnetic surfaces thus can not be changed. Only non-zero resistivity allows the *magnetic reconnection* to occur. The importance of resistive MHD is in the inclusion of qualitatively different phenomena compared to the ideal MHD, even if they occur on much slower time scales than the ideal phenomena due to smallness of the resistivity η.

Instabilities

Stability is the property of a system with respect to perturbations from an equilibrium state. If the system returns to the equilibrium, it is *stable*. If the initial perturbation increases, it is *unstable*. The stability of MHD equilibria are typically studied using the ideal MHD. The linear approach to stability analysis consists of analyzing the force caused by a displacement from equilibrium in a linear approximation. If the force acts to diminish any displacement, the equilibrium is stable, otherwise if there is a displacement which gets augmented by the resulting force, the equilibrium is unstable. The linear stability theory is valid for displacements small enough to allow

a linear approximation. A linear instability grows exponentially until non-linear effects become important, which may act against the linear instability drive and stop the growth, in this case one speaks of *saturation*. Resistive instabilities have much slower growth rate than ideal instabilities, their importance is that they can present qualitatively different plasma behavior than ideal instabilities, consisting of changes in magnetic topology, as explained in section 3.1.2. An example change of magnetic topology is the opening of *magnetic islands*, as described in section 4.1. The instabilities based on formation of islands are called *tearing modes*.

In a plasma the most important MHD instabilities are driven by the gradient of pressure and by the current. In a tokamak the former occur preferentially on the low field side. A displacement of the flux surface away from the plasma on the low field side is in the direction of decreasing toroidal field, thus decreasing magnetic pressure. This increases the force imbalance between the plasma pressure and the magnetic pressure. This is called *ballooning instability*. The current-driven instability is called *kink instability*.

An example of instability which is not primarily of MHD origin is the *radiative instability*. In section 1.1 we have neglected the radiative losses while deriving the fusion reactor power balance. This assumption relies on sufficient purity and temperature of the plasma. Impurities with a high atomic number Z may be only partly ionized even at temperatures where hydrogen is fully ionized. The resulting line radiation may become a significant energy loss channel. If it leads to a decrease of plasma temperature, the amount of incompletely ionized atoms increases and so does the line radiation. The plasma edge is most susceptible to this instability because of lower temperatures and higher impurity concentration. If the edge cools as a result of the radiative instability, the current becomes more peaked in the hotter core region and the resulting change of the safety factor profile can lead to other instabilities of MHD origin.

In addition to be in equilibrium, the fusion plasma shall avoid instabilities. This places additional constraints on the equilibrium, in particular the value of β, because the pressure is a destabilizing factor and the magnetic field a stabilizing one, as the magnetic pressure compensates the plasma pressure and bending the field lines produces a force which opposes the instability. The most important limits are [21]:

- The upper limit on the plasma current, caused by kink modes, which can be restated as the lower limit of the edge safety factor. This is known as the Kruskal-Shafranov limit.

- The β limit, which is determined by coupled peeling-ballooning modes. The maximum allowable value of β is proportional to $I/(aB)$. The

value $\beta_N \equiv \beta aB/I$ is known as the *normalized beta*. The limit on β_N is known as the Troyon limit and has the value of $\beta_N = 0.028$ when the current is measured in MA.

- The density limit, caused by the radiative instability at the plasma edge if the rise of density at a given pressure results in a decrease of temperature.

MHD stability can be improved by the presence of a conducting wall. Field lines can not diffuse through a perfectly conducting material, so a perfectly conductive wall repels plasma displacements associated with the instabilities and stabilizes them. A realistic resistive wall will only slow down the instability to the timescale required for field penetration through the wall (caused by resistive dissipation of the eddy current). As an example, the β limit is lower for a plasma without a wall than for a plasma with a perfectly conducting wall. For values of β_N between the no-wall limit and ideal wall limit the instability may develop thanks to the resistivity of the wall and is caused *resistive wall mode (RWM)*. This can be alleviated by rotating the plasma. If the toroidal rotation is fast enough, the perturbation associated with the instability does not penetrate through the resistive wall. The toroidal rotation has thus a beneficial effect on MHD stability and braking it is undesirable.

3.2 Transport and confinement

The plasma confinement in a tokamak is ensured by the magnetic field. Confinement is reduced when the particles can diffuse across the field lines. The transport can be measured using the transport coefficients. Assuming that the fluxes are proportional to the gradients, the diffusion can be expressed using equations analogous to the classical equation of heat conductivity:

$$\frac{\partial T}{\partial t} = \nabla \cdot (\chi \nabla T) \tag{3.10}$$

$$\frac{\partial n}{\partial t} = \nabla \cdot (D \nabla n) \tag{3.11}$$

The equation (3.10) expresses transport of heat and equation (3.11) the transport of particles. χ is the thermal diffusivity and D the particle diffusion coefficient. Both have the units $[\mathrm{m^2 s^{-1}}]$. If the diffusion is a simple random walk with step size Δl and duration τ, the diffusion coefficient is $D = (\Delta l)^2/\tau$.

3.2.1 Classical transport

An elementary reason why the plasma particles may diffuse across the field are their collisions [22]. If a particle performing gyro motion changes its perpendicular velocity significantly as a result of a collision, its gyration center moves by a distance on the order of its Larmor radius r_{L} (section 2.1). The diffusion coefficient shall then be $D \sim r_{\mathrm{L}}^2/\tau$ where τ is the average time between collisions. A more precise analysis shows that only collisions between unlike particles cause particle diffusion and that the diffusion coefficients for electrons and ions are the same (the transport is *ambipolar*). A similar estimate can be done for the heat diffusivity, which is greater than the particle diffusion coefficient because even collisions between like particles exchange energy and contribute to heat conduction. For a fusion-relevant plasma the classical diffusion coefficients are at the order of $\chi \approx 10^{-3}$, $D \approx 10^{-5}$.

3.2.2 Neoclassical transport

In a toroidal plasma the transport is significantly enhanced due to the particle drifts described in section 2.1 which make the particles deviate from the field lines [22]. The particle orbits are closed due to the toroidal symmetry, but they deviate from the flux surfaces. The drift is always vertical (see section 2.2), but it moves the particle either inwards or outwards relative to the magnetic axis. If the drift points downwards, the particle moves outwards when below the midplane and inwards when above. Depending on the direction of the particle motion in the poloidal plane (which in turn depends on the helicity of field lines and the toroidal direction of particle motion) the particle orbit is shifted with respect to the flux surface outwards on the LFS and inwards on the HFS, or vice versa. The radial distance Δr of the inner and outer position is the drift velocity (given by equation (2.4)) divided by the frequency of the poloidal motion, and is expressed by the formula

$$\Delta r = 2\frac{q}{\omega_c}\frac{v_\parallel^2 + v_\perp^2/2}{v_\parallel} \tag{3.12}$$

If a collision reverses the direction of the particle velocity, its new orbit is shifted in the opposite direction than the original orbit and the maximum displacement between the new and the original orbit is Δr. Such collisions cause a diffusion with a diffusion coefficient $D \sim \Delta r^2/\tau$. As Δr is larger than r_{L}, this leads to significant increase of the diffusion compared to the classical estimation.

The conservation of the magnetic moment μ (section 2.1) causes a fraction of particles to be trapped on the low field side of the torus. The parallel

velocity of these particles is low enough to cause them to be reflected by the increasing magnetic field as they move along a field line back to the low field side. The turning point is at a position where $B = E/\mu$. On the way back the particle orbit is displaced in an opposite direction relative to the flux surfaces than on the way forward, and thus does not return on the same path. The full orbit is called *banana orbit* because of its shape. Its width is

$$\Delta r = 2\frac{q}{\omega_c}\frac{v^2}{v_\parallel} \tag{3.13}$$

(we use the fact that the perpendicular velocity dominates, $v^2 \approx v_\perp^2$, and the average parallel velocity is $v_\parallel/2$, $v_\parallel$ being the maximum parallel velocity at the LFS).

It turns out that the transport by banana particles dominates. While they represent only a fraction on the order ϵ of the particles, their step size Δr is greater than for the trapped particles and due to the smallness of $v_\parallel$ the collisions reverting its direction are more likely (τ needs to be replaced by an effective collision time which is the characteristic time between such collisions and is smaller than τ).

3.2.3 Anomalous transport and H-mode

The actual transport coefficients in tokamaks are on the order of 1 $\mathrm{m^2 s^{-1}}$, larger than the neoclassical estimation. This discrepancy is explained by the existence of small-scale instabilities, or microinstabilities. Unlike the large instabilities they do not terminate the plasma, but produce a turbulence whose characteristic property is varying electrostatic potential. The electrostatic turbulence causes a significant transport due to the $E \times B$ (cf. section 2.1) convection along the equipotential surfaces. The confinement regime characterized by anomalous transport is called the *L-mode* (low confinement mode). Its poor confinement necessitates a large size of a reactor operating in L-mode, even larger than the optimum size for a fusion reactor (cf. the introduction of the chapter 3), which would lead to increase in cost.

It was first discovered on the tokamak ASDEX that when a sufficient external heating power is reached, the plasma transitions into a regime with higher confinement, called the *H-mode* [28]. In the H-mode the energy confinement time is increased with respect to the L-mode by a factor of about two. The transport coefficients in the H-mode are not reduced in the whole volume of the plasma, the transport is decreased only in a layer near the edge, called the *transport barrier*. In the transport barrier there are strong gradients of the temperature and density profiles, corresponding to low transport coefficients. Inside the transport barrier the profiles are similar to the

L-mode. In this way, H-mode profiles are raised with respect to the L-mode profiles on a so-called *pedestal*. The pedestal values determine the values in the plasma center, as outside the transport barriers the gradients are difficult to increase (the profiles are *stiff*). The energy which the plasma would have if the profiles had the pedestal values everywhere inside the transport barrier is called *pedestal energy*.

The transition between L-mode and H-mode is not gradual but is has a character of a bifurcation, with no stable intermediate state. It is facilitated by several conditions, among them [28]:

- Magnetic configuration with a divertor instead of a limiter (see section 2.5). In particular, the ion drift (section 2.1) should have a direction towards the divertor.
- Clean plasma (low impurity level) which can be achieved by special wall conditioning procedures (boronization).
- Operation with deuterium.

The H-mode is believed to be a result of shear flows in the pedestal, corresponding to a strong gradient of the radial electric field. The shear flow reduces the turbulent "eddies" by decorrelating them in the radial direction ("tearing them apart"). The reason for the appearance of a radial electric field gradient is not yet well known, although several explanations exist [29].

3.2.4 ELMs

The reduced turbulent transport in H-mode is partially compensated by periodic events, called *edge localized modes (ELMs)* [30, 31]. An ELM causes a sudden release of a part of the pedestal energy and particles which eventually hit the divertor. It could be expected that a H-mode without ELMs would have the best confinement. This is indeed the case, but the good particle confinement causes the density and impurity levels to rise, eventually leading to a radiative instability (cf. section 3.1.2). The ELMs, by ejecting part of the plasma particles, maintain stable density and impurity levels and are thus essential for the H-mode operation. The ELMs are classified into many types. One classification is phenomenological: after the L-H transition, the smaller type III ELMs appear, with frequency decreasing as the heating power increases. With the increasing heating power they eventually disappear and the plasma enters an ELM-free regime. Above a certain threshold in the external heating power (about twice the threshold needed for the L-H transition) ELMs again appear, called type I ELMs. Their frequency increases

with the applied heating power. There are other ELM types accessible at special conditions, such as type II ELMs in strongly shaped plasmas. The H-mode with type I ELMs is the favored regime for a reactor because of its good confinement.

Another criterion is to consider the origin of the ELMs. ELMs are associated with MHD instabilities, as proven by magnetic fluctuations measured during the ELMs. It is believed that the good confinement of the H-mode causes an increase of the pressure gradient in the pedestal above a point where it triggers a MHD instability. Type I ELMs are believed to be ideal instabilities, so-called peeling-ballooning modes, which are in addition to the pressure gradient triggered by the edge current. Indeed, plasma exhibiting type I ELMs are located at the boundary of a region stable to peeling-ballooning modes. Type III ELMs occur in plasmas inside the stable region so their mechanism may be different, e.g. a resistive instability.

While the linear ideal MHD stability calculations can predict when the plasma will exhibit type I ELMs by determining the onset of the instability, the evolution of the ELM is eventually a nonlinear process and is much more difficult to simulate theoretically. From the experimental observations it is known that the ELMs have filamentary nature [32] — hot filaments are being ejected from the plasma and eventually lose their energy to the divertor and wall. The complete dynamics of the ELM is important because it determines the amount of losses during the ELM. While a progress in nonlinear simulations of the ELM evolution is being made, quantitative estimates of the ELM size (the amplitude of the ELM loss) still rely on experimental studies. A good parameter governing the relative ELM size is the pedestal electron collisionality ν_e^* which is a dimensionless parameter inversely proportional to the electron mean free path and normalized to the tokamak parameters: $\nu_e^* \equiv \pi R q_{95}/\lambda_{e,e}$ where $\lambda_{e,e}$ is the mean free path between electron-electron collisions. The ELM energy loss relative to the pedestal energy increases with decreasing ν_e^* [33]. Predicting the ELM energy loss is important because a large enough loss could lead to unacceptably high transient power loads on the divertor plasma-facing components.

3.3 ITER

In the introduction of this chapter the need for a tokamak experiment significantly larger than the present experiments to explore the burning plasma regime (at or near ignition) was mentioned. This planned device is called ITER. Its original design is presented in [34]. The goal of this design was to achieve ignition. Since then the design was scaled down for cost reasons.

The new design [35] has a goal of achieving the power amplification $Q = 10$, which will still allow investigation of a regime predominantly heated by its own fusion power. ITER will have a major radius of 6.2 m, minor radius of 2.0 m and superconducting coils providing a toroidal field of 5.3 T. Its dimensions will be about twice as great as those of the present largest tokamak JET. Its aspect ratio is however similar to many existing tokamaks, including JET, DIII-D, ASDEX and COMPASS. The required power amplification (corresponding to the absolute fusion power of 500 MW) will be made possible by the H-mode (section 3.2.3), more precisely the type I ELM H-mode (section 3.2.4) which has the required confinement. (This prediction is however based on an extrapolation from the present experiments.) The construction has started at the chosen site in Cadarache, southern France, while the ITER design is being refined.

One of the most serious issues with the ITER design are the transient power loads on the plasma-facing components caused by the type I ELMs. Type I ELMs (also called "giant" ELMs) have the disadvantage of being large compared to the other ELM types. The scaling with the pedestal electron collisionality (section 3.2.4) predicts a larger fraction of the pedestal energy to be lost compared to the present tokamaks, as the ITER collisionality will be lower. At the same time the absolute pedestal energy will be greater. Both factors contribute to the large expected ELM energy. The problem of ELMs and plasma-facing components in ITER is reviewed in [36, 37] and references therein. The ELM energy according to the scaling is expected to be about 20 MJ, but intolerable damage (erosion, melting, crack formation) to the divertor plasma-facing components is expected to occur at ELM energies above 1 MJ. Clearly, type I ELMs are unacceptable and the fact that at the same time they are the standard operating scenario for ITER presents a serious obstacle to achieving ITER's goals.

A solution to this problem involves finding an operating scenario which would have the same desirable properties of type I ELM H-mode while avoiding the giant ELMs. Many such scenarios wit small or no ELMs have been proposed, but their applicability to ITER is a question, as they usually require some set of special conditions.

Another possible solution is some sort of active control of the ELMs. As the ELM size decreases with their increased frequency, if they could be driven fast enough, their size might be reduced to a benign scale. It is known that injection of pellets of frozen fuel and fast vertical movements ("kicks") trigger ELMs, so those methods might be used to drive the ELMs to the desired frequency. Finally, one promising method is the application of nonaxisymmetric magnetic perturbations to the plasma by external coils. This method is the motivation of much of the work presented in this thesis. To explain

the role of magnetic perturbations we shall return to the configuration of the tokamak magnetic fields and present the magnetic perturbations as an application of the theory of dynamical systems, in particular the theory of chaos in hamiltonian systems.

Chapter 4

Field lines as a dynamical system

A field line can be considered as a trajectory of a dynamical system. The independent variable, which in physical dynamical systems has usually the meaning of time, is here instead a suitable parameter ξ increasing along the field line. The dynamical system is given by first-order ordinary differential equations of evolution of the space variables along the field line. As a concrete example, in the (R, Z, ϕ) coordinate system, those equations are:

$$\begin{aligned} \frac{\mathrm{d}R}{\mathrm{d}\xi} &= B^R \\ \frac{\mathrm{d}Z}{\mathrm{d}\xi} &= B^Z \\ \frac{\mathrm{d}\phi}{\mathrm{d}\xi} &= B^\phi \end{aligned}$$

where (B^R, B^Z, B^ϕ) are the *contravariant components* of the field $\vec{\mathbf{B}}$.

In a magnetic confinement device with a strong toroidal field B^ϕ is always nonzero, which allows us to factor out ξ using the third equation and use instead ϕ as the field line parameter:

$$\frac{\mathrm{d}R}{\mathrm{d}\phi} = \frac{B^R}{B^\phi} \tag{4.1}$$

$$\frac{\mathrm{d}Z}{\mathrm{d}\phi} = \frac{B^Z}{B^\phi}. \tag{4.2}$$

Analogous equations hold for any other choice of coordinates in the poloidal plane instead of (R, Z).

The solution of the equations (4.1), (4.2) is a function $T((R_0, Z_0); \phi)$ with values in the (R, Z) space which gives the position at ϕ of a field line started at a position (R_0, Z_0) for $\phi = 0$.

The evolution of field lines in the toroidal direction given by $T((R_0, Z_0); \phi)$ has a remarkable property: for a set of field lines starting in a surface Σ_0 in the poloidal plane at $\phi = 0$, the flux of the magnetic field through Σ_0 is the same as the flux through the surface Σ_ϕ formed by those field lines at any other toroidal angle ϕ: $\Sigma_\phi = T(\Sigma_0; \phi)$. This is a consequence of zero divergence of the magnetic field. In other words, the transformation by $T((R_0, Z_0); \phi)$ conserves the differential form $B_\mathrm{T}\ \mathrm{d}R \wedge \mathrm{d}Z$ which expresses the flux of the toroidal field B_T through the infinitesimal surface $\mathrm{d}R\ \mathrm{d}Z$. It can be shown that one can find new coordinates $(p(R, Z, \phi), x(R, Z, \phi))$ where this property is simplified to conservation of surface in the (p, x) plane, or the volume form $\mathrm{d}p \wedge \mathrm{d}x$ in the language of differential forms. The choice of (p, x) (called *canonical coordinates*[1]) is not unique. The coordinate x can be chosen e.g. as the vertical position Z and the corresponding p will be noted p_z. Another special choice will be given below.

Moreover it can be shown that for any choice of coordinates (p, x) in which the evolution of field lines satisfies the condition of conserving the surface in the (p, x) plane, the equations (4.1), (4.2) can be rewritten in the form

$$\frac{\mathrm{d}p}{\mathrm{d}\phi} = -\frac{\partial H}{\partial x} \tag{4.3}$$

$$\frac{\mathrm{d}x}{\mathrm{d}\phi} = \frac{\partial H}{\partial p} \tag{4.4}$$

for a suitable scalar function H, called the *hamiltonian*. Equations of the form ((4.3),(4.4)) are called *canonical equations* or *Hamilton's equations* and are of fundamental importance in classical mechanics, where the physical time t instead of ϕ is used as the independent variable. In a toroidally symmetrical situation, the transformation $(R, Z) \to (p, x)$ is the same for every poloidal plane[2] and H is independent on ϕ. Then H is conserved along field lines[3]: $\mathrm{d}H/\,\mathrm{d}\phi = 0$ and the surfaces of constant H are flux surfaces. It follows that in an axisymmetric configuration flux surfaces always exist.

[1] The canonical coordinates are usually labeled p, q. Here x is used instead of q to avoid confusion with the safety factor q.

[2] This holds even for a weaker assumption: it is enough that the toroidal field B_T be independent on ϕ.

[3] An equivalent statement in the language of classical mechanics is that the total energy of the system which is equal to the hamiltonian is conserved when the hamiltonian does not depend explicitly on time.

It has been know for a long time that the canonical coordinates and the hamiltonian in the mechanical analogy of the field lines are related to the magnetic fluxes defined in 2.4. As shown in [1], when the magnetic field is expressed using the vector potential, the equations of field lines have the form ((4.3),(4.4)):

$$\frac{\mathrm{d}A_{\theta^*}}{\mathrm{d}\phi} = -\frac{\partial A_\phi}{\partial \theta^*} \tag{4.5}$$

$$\frac{\mathrm{d}\theta^*}{\mathrm{d}\phi} = \frac{\partial A_\phi}{\partial A_{\theta^*}} \tag{4.6}$$

where A_{θ^*}, A_ϕ are the *covariant components* of the vector potential $\vec{\mathbf{A}}$ corresponding to the coordinates θ^*, ϕ. A_ϕ is expressed using the physical component $A_{\hat{\phi}}$ as $A_\phi = RA_{\hat{\phi}}$. A_{θ^*} is used as a coordinate in the poloidal plane together with θ^*. It follows that the field lines are equivalent to a hamiltonian dynamical system, where (A_ϕ, θ^*) are canonical coordinates, A_ϕ takes the role of hamiltonian and ϕ the role of time. Moreover, when flux surfaces exist, the magnetic flux functions are equal to the covariant components of the vector potential: $A_\phi = \psi$, $A_{\theta^*} = \Phi_\mathrm{t}$. We will use those relations to generalize the flux functions ψ, Φ_t to the non-axisymmetric case when the magnetic surfaces may not exist. Using this notation, the canonical equations ((4.5), (4.6)) may be written as

$$\frac{\mathrm{d}\Phi_\mathrm{t}}{\mathrm{d}\phi} = -\frac{\partial \psi}{\partial \theta^*} \tag{4.7}$$

$$\frac{\mathrm{d}\theta^*}{\mathrm{d}\phi} = \frac{\partial \psi}{\partial \Phi_\mathrm{t}}. \tag{4.8}$$

In particular, in the case of toroidal symmetry and magnetic surfaces, ψ depends only on Φ_t and using (2.14) the equations ((4.7), (4.8)) reduce to

$$\frac{\mathrm{d}\Phi_\mathrm{t}}{\mathrm{d}\phi} = 0 \tag{4.9}$$

$$\frac{\mathrm{d}\theta^*}{\mathrm{d}\phi} = \frac{1}{q}. \tag{4.10}$$

The first equation (4.9) expresses that the field line stays on the flux surface, which is a surface of constant Φ_t, while the second (4.10) is consistent with the definition of θ^* (section 2.6, equation (2.15)).

The poloidal flux ψ determines the poloidal field. By the definition of flux surfaces $\vec{\mathbf{B}}_\mathrm{P} \perp \nabla\psi$. As ψ is related to the vector potential, $\vec{\mathbf{B}}_\mathrm{P}$ can be

easily determined explicitly:

$$B_R = -\frac{1}{R}\frac{\partial \psi}{\partial Z} \tag{4.11}$$

$$B_Z = \frac{1}{R}\frac{\partial \psi}{\partial R} \tag{4.12}$$

Any variables (I, ϑ) of a hamiltonian system which are canonical and moreover have the property that the hamiltonian H depends only on I are called *action-angle variables*, I being the action and ϑ the angle. In our case Φ_t is the action and θ^* is the angle. When a transformation to the action-angle variables has been found, the canonical equations are essentially solved because in the action-angle variables they have a particularly simple form – in our case the equations (4.9), (4.10).

4.1 Magnetic islands

The equations ((4.9), (4.10)) are valid for the toroidally symmetrical situation where $(\Phi_\mathrm{t}, \theta^*)$ are exact action-angle variables. Let us now consider an almost-axisymmetric case, assuming that the non-axisymmetry is a small perturbation to the axisymmetric one. We will assume further that only the poloidal field is perturbed, i.e. the perturbation can be expressed using the poloidal flux. The poloidal flux can be written as

$$\psi = \psi_0(\Phi_\mathrm{t}) + L\delta\psi(\Phi_\mathrm{t}, \theta^*, \phi) \tag{4.13}$$

where ψ_0 is the toroidally symmetrical and exactly integrable part, while $L\delta\psi(\Phi_\mathrm{t}, \theta^*, \phi)$ is the perturbation. L is a small parameter expressing the amplitude of the perturbation. The unperturbed part defines field line dynamics given by equations ((4.9), (4.10)) where q is now defined as $q = \mathrm{d}\Phi_\mathrm{t}/\,\mathrm{d}\psi_0$. For the perturbed dynamics the general equations ((4.7), (4.8)) are applicable. Using (4.13) they can be written as

$$\frac{\mathrm{d}\Phi_\mathrm{t}}{\mathrm{d}\phi} = -L\frac{\partial\,\delta\psi(\Phi_\mathrm{t}, \theta^*, \phi)}{\partial\,\theta^*} \tag{4.14}$$

$$\frac{\mathrm{d}\theta^*}{\mathrm{d}\phi} = \frac{1}{q} + L\frac{\partial\,\delta\psi(\Phi_\mathrm{t}, \theta^*, \phi)}{\partial\,\Phi_\mathrm{t}}. \tag{4.15}$$

The relation (4.13) is an exact analogy of the perturbed hamiltonian (A.11) from Appendix A. In the presence of a toroidally asymmetric perturbation the field lines are thus a dynamical system with $1\,\frac{1}{2}$ degrees of freedom. Analogously to (A.12) we may decompose the perturbation in a sum of harmonic

modes:

$$\delta\psi(\Phi_{\mathrm{t}}, \theta^*, \phi) = \sum_{(m,n)} \delta\psi_{m,n}(\Phi_{\mathrm{t}}) \cos(m\theta^* - n\phi + \phi_{m,n}). \tag{4.16}$$

The sum is over all pairs of integers (m, n) with n being conventionally non-negative, $\phi_{m,n}$ are the phases of the modes.

From the results summarized in Appendix A it follows that the perturbation will strongly modify field lines in the vicinity of a resonance. The resonance condition is here $q = m/n$, because due to (4.10) the expression $q\theta^* - \phi$ is constant on an unperturbed field line, and for $q = m/n$ is constant also the corresponding term in the series (4.16). The perturbation thus disrupts magnetic surfaces in the vicinity of the resonance in a way which can be also deduced from the results of Appendix A. Magnetic surfaces are a special case of invariant tori in an integrable system – they are determined by constant values of the action Φ_{t}. In the vicinity of the resonance a different type of magnetic surfaces are thus formed, called *magnetic islands*. They are a special case of the islands mentioned in section A.2.1 and have, in the coordinates Φ_{t} and ζ:

$$\zeta \equiv m\theta^* - n\phi \tag{4.17}$$

(ζ is defined to be constant on an unperturbed field line), the form of phase trajectories of the pendulum. From (4.17) it follows that the island is helically wound around the magnetic axis and during m turns around the major axis it turns n times around the magnetic axis and returns to the same point in the poloidal plane, which it have intersected m times, showing as a chain of m islands. Each of these has an elliptic fixed point in the center and they are separated by hyperbolic fixed points.

Depending of field line position relative to the island separatrix it can be trapped in the island – a periodic libration around the elliptic fixed point occurs, or it may remain in the mostly unperturbed invariant tori (KAM tori) farther from the resonance. A limiting case is the movement in the chaotic layer around the separatrix. Here one can not speak about a flux surface, because the field line densely fills the volume of the chaotic layer, delimited by the KAM tori. As a general perturbation is a sum of harmonic modes (4.16), there are many island chains, one corresponding to every mode which has a corresponding safety factor $q = m/n$ in the plasma. If the perturbation is strong enough, the magnetic surfaces (KAM tori) separating the island chains may be destroyed and the chaotic layers around the island separatrices merge to form a global chaotic region. One speaks about transition to global stochasticity[38]. The onset of global stochasticity can be estimated using the Chirikov criterion (see section A.2.3): the neighboring island chains shall be so wide that they overlap.

The behavior of a field line is well observable by plotting the points of its intersections during many toroidal turns with a given poloidal plane, which has a role of a Poincaré section (section A.2.4).

Magnetic islands can appear due to several causes: the perturbation can be either internal or external to the plasma.

- On the rational surfaces an instability may develop which, in the linear approximation, occurs when a perturbation causes its own growth in a positive feedback loop. The perturbation is produced by a helical current layer which develops around the resonant surface. The growth of magnetic islands is accompanied by tearing and reconnection of magnetic surfaces (change of the topology) which is not possible in an ideally conductive plasma. This instability is thus an example of a resistive instability (cf. section 3.1.2) and is called a *tearing mode*.

  The field lines inside an island connect its inside edge to the outside and facilitate the transport across the island. The island thus causes flattening of plasma profiles. In some situations this can drive an instability. The pressure gradient in the plasma drives a parallel current due to neoclassical effects, called the *bootstrap current*. The flattening of pressure profile make the bootstrap current disappear inside the island, effectively producing a helical current perturbation aligned with the island. The magnetic field perturbation caused by the current perturbation acts to enlarge the island and thus an instability develops. This variant of tearing mode is called the *neoclassical tearing mode*.

- Perturbation external to the plasma may be caused by deviations from a perfect symmetry of the tokamak. Examples are misalignments of the coils and the presence of current conductors supplying the coils. Perturbation fields from such sources are called *error fields*.

  The presence of error fields aggravates the plasma instabilities. By interaction with the plasma they can stop the rotation. An instability which does not rotate is called a *locked mode*. Locking of an instability cancels the stabilizing effect of the conductive wall (cf. section 3.1.2).

  The existing error fields shall be compensated by error field correction coils (EFCCs) which produce a perturbation opposing the natural error field.

- Magnetic perturbations can be introduced artificially, as it turns out that in some cases they have beneficial effects, in particular on the ELMs (section 3.3). We speak often about *resonant magnetic perturbations (RMPs)* as it is the resonant component of the perturbation

which is responsible for the island formation. The perturbations are produced by coils outside the plasma, which create mostly radial perturbation field (to break the magnetic surfaces a perturbation perpendicular to them is the most efficient). Care must be taken however to not trigger locked modes. The applications of such magnetic perturbations are described in the next chapter.

Chapter 5

Resonant magnetic perturbations from coils

5.1 Ergodic divertor

The first application of resonant magnetic perturbations was to provide an alternative to the limiter. If the stochastic zone is located at the edge and connected to the wall, it will define a LCFS at its inner edge. Beyond the LCFS, however, the plasma does not immediately touch the wall but is separated from it by the stochastic zone. Here the field lines are eventually connected to the wall, but at a rather large distance. (The areas where the field lines connect to the wall after a short distance form the *laminar zone*.) The ergodic divertor has similar benefits as the axisymmetric divertor with an X-point (cf. section 2.5) — it reduces the contamination of plasma by the impurities from the wall. In particular, the plasma flows along the field lines in the stochastic layer towards the wall will drag with itself the impurities, thus screening the core plasma from them [39]. However, the ergodic divertor does not facilitate the transition to H-mode [40], unlike the axisymmetric divertor.

Two best known examples is the ergodic divertor on the Tore Supra tokamak and the dynamic ergodic divertor (DED) on the TEXTOR tokamak. Both are formed by helical coils inside the vessel aligned with the characteristic pitch of field lines (the safety factor). In the case of Tore Supra the coils were modular [41], while in the DED, they are continuous and cover all the HFS. The DED coils can be wired in several configurations with varying toroidal and poloidal mode numbers (n, m), but the ratio m/n determining the resonant value of q can not be changed, as it is determined by the pitch angle of the coils. In practice the spectra do not contain only the corre-

sponding poloidal mode but also some sidebands, which allow the formation of several island chains and their overlap into a stochastic layer. The divertor on TEXTOR is *dynamic* because it can be supplied with alternating currents, producing a rotating perturbation.

The ergodic divertors have contributed significantly to the understanding of the stochastic layers. Especially on the DED which is still in operation (the ergodic divertor on Tore Supra was replaced by a standard limiter) many interesting experiments and comparisons with theory have been done. It was confirmed on both machines that the stochastic zone leads to a reduction of the temperature gradient [42] because of the parallel transport of heat by the fast moving electrons [43]. Changes in the radial electric field [42] and plasma rotation [44] were observed. This is consistent with the theoretical picture that the electrons which are faster escape along the stochastic field lines and create a positive radial electric field. This results in an enhanced transport of ions in order to maintain plasma quasineutrality, however as the ions are slower, their parallel transport is slower and the transport is partly perpendicular to the field lines, which produces a force spinning up the plasma.

On TEXTOR many investigations were dedicated to examining the structure of the edge magnetic field. The complicated pattern of interwoven stochastic and laminar zones near the DED coils was observed, as were structures corresponding to the magnetic islands . The heat flux patterns on the divertor plates have been shown to correspond to the invariant manifolds of the island X-points, which guide the field lines.

5.2 RMPs in tokamaks with poloidal divertor

One characteristics of the poloidal (axisymmetric) divertor is the divergence of the safety factor q near the separatrix (section 2.5). The safety factor passes through infinitely many resonant values m/n for a given n, creating infinitely many island chains. This situation is favorable to island overlap at the edge. The island width scales with the radial derivative q' of q as $1/\sqrt{q'}$, while the distance of the neighboring island chains scales as $1/q'$. The Chirikov parameter then scales as $\sqrt{q'}$ This means that sufficiently close to the separatrix (where q' is also divergent) the islands will always overlap and create a stochastic layer.

The ergodic divertor in a circular plasma is tuned to one resonant value of q and its near sidebands. In contrast, at the edge of a configuration with an X-point, one geometric mode is resonant with all the rational values of q. This is because the divergence of q is caused by the X-point, outside the

X-point region the field line pitch angle varies slowly. If the coils are placed in such a region (typically the LFS), their field may be resonant with the rational surfaces of a given n because it is the alignment with the local pitch angle which matters. This is explained in more detail in our works [9, 14].

Moreover, the presence of perturbations in a separatrix configuration causes the separatrix to split into two surfaces (invariant manifolds of the X-point) in a similar way as for the separatrix of an island chain. The invariant manifolds intersect each other infinitely many times and this complicated structure (homoclinic tangle) leads to the formation of a stochastic layer (thinner than the stochastic layer formed by the island overlap [45]) around the separatrix. The invariant manifolds also guide the field lines coming from the plasma core to the divertor plates, creating a splitting of the divertor strike points into structures known as *divertor footprints*.

For those reasons the divertor configuration is more susceptible to creating an edge stochastic region than a circular configuration such as Tore Supra or TEXTOR.

The first divertor tokamak where the RMPs were applied to create a stochastic edge was JFT-2M [46]. Improvement of the density limit was observed. The observed formation of a positive radial electric field and the change of toroidal rotation seem to be consistent with the ergodic divertor results, however the reduction of the edge temperature gradient was not observed [47]. An interesting result was the impact on ELMs: the RMPs triggered frequent ELMs in an ELM-free H-mode [46]. A similar result was observed on COMPASS-D [48]. The RMPs were then proposed as a solution to the ELM problem of ITER [49]. It was supposed that they would allow to control the edge temperature and thus pressure gradients, similarly to the ergodic divertor, in order to suppress the instability which is driven by the pressure gradient. Successful experiments have been indeed performed on the DIII-D tokamak.

5.3 ELM control with RMPs

The DIII-D tokamak is equipped with a set of twelve coils, called I-coils, inside the vacuum vessel in two horizontal rows of six coils each. By alternating the currents one can produce a $n = 3$ perturbation. Two configurations are possible: either the lower row has the same polarity as the upper row and the configuration is vertically symmetric (called *even parity*), or the rows have opposite polarities (or shifted phase by π) and the configuration is vertically antisymmetric (called *odd parity*). The odd parity configuration was tested first in high collisionality ($\nu_e^* \approx 1$) experiments. Most of type I ELMs dis-

appeared, although some isolated events remained. It is interesting that the odd parity perturbation field is not resonant with the field lines and thus the effect is not due to the resonance. Since then further experiments have been done at a more ITER-relevant lower collisionality $\nu_e^* \approx 0.1$ and mostly with even coil parity which is resonant with the safety factor at the edge [50, 51]. In those experiments the ELMs are completely suppressed for a narrow range in the edge safety factor q_{95}. An empirical criterion was derived for the onset of the effect on ELMs [51]: the edge region where the Chirikov parameter is greater than one shall have a width at least 0.165 in terms of ψ_N. If q_{95} is outside the resonant window for ELM suppression and the stochastic region is narrower, ELMs remain, but they are smaller and more frequent than in the case without perturbation. Application of RMPs results in changes in the edge radial electric field [52] and increase of the plasma toroidal rotation [50], similar to the ergodic divertor.

This criterion supports the picture of ELM suppression cited in the previous section: creation of a stochastic region and reduction of the pressure gradient in the pedestal under the critical value which triggers the ELM instability. Indeed, when ELMs are suppressed, the ideal MHD stability analysis shows that the pedestal has moved to a stable region [52]. However the edge profiles does not correspond to this theory, as the pressure reduction is caused by a reduction of density and the expected flattening of the temperature profile is not observed [51]. The density pump-out is not as sensitive to the value of q_{95} as the ELM suppression, indicating that there is some additional cause of the ELM suppression, such as current profile changes [51], to which the peeling-ballooning modes are also sensitive. The density pump-out is an unwanted effect, as the reduction of density would decrease the fusion power output of a reactor.

Following these successful experiments there were attempts to reproduce the ELM suppression on other tokamaks. Coils similar to the ones on DIII-D were not available, so other coils capable of producing the RMPs were used. On JET and MAST there are the error field correction coils (EFCCs) — four large coils around the machine, able to produce $n = 1$ or $n = 2$ perturbation fields. The JET experiments succeeded in obtaining smaller and more frequent ELMs [53], accompanied by a density pump-out. A complete suppression of ELMs has not been observed so far. The effect is also correlated with the width of a region where the Chirikov parameter is greater than 1 [11]. On MAST coils similar to the DIII-D I-coils were later installed [11], but ELM suppression was not observed despite having satisfied the Chirikov parameter criterion [54]. In L-mode the RMPs produce a density pump-out [10], which resembles the DIII-D and JET results, but this effect has not been observed in H-mode. In L-mode changes in turbulence [55] and

the electric field [55, 56] are also observed. In ELM-free H-mode discharges the RMPs trigger ELMs similarly to the earlier COMPASS-D and JFT-2M results.

As the potential of the RMPs to suppress ELMs is very promising, similar experiments on other tokamaks are planned. On ASDEX the installation of an extensive set of coils is in progress [57]. JET is considering the installation of additional RMP coils which would be able to produce more localized perturbation and higher n. There are plans to install RMP coils on TCV [58]. Experiments with the existing coils on COMPASS are a significant element of its scientific programme. Installation of a flexible set of RMP coils on ITER [37] is under discussion in the hope that they could solve the problem of ELM-caused heat loads.

5.4 Plasma response to RMPs

The picture of ELM suppression by the creation of a stochastic region relies on the vacuum approximation of the perturbation field: the total magnetic field is assumed to be the sum of the field without the RMPs and the vacuum field of the perturbation coils. The vacuum approximation is also used to evaluate the empirical criterion for ELM suppression. It has been known that the RMPs may interact strongly with the plasma, especially with rotating plasma. The perturbation induces parallel eddy currents at the resonant surfaces which produce an opposing perturbation. At the same time the interaction of this current with the perturbation field leads to a localized braking of the rotation [59]. The braking can be compensated by the viscosity transferring the momentum to the plasma at the resonant surface. The balance of forces is nonlinear and has two bifurcated solutions [60]: in one the resonant mode of the perturbation is mostly screened at the resonant surface and the braking is weak, in the other the plasma rotation is stopped and a magnetic island appears. The transition from the former to the latter at a sufficient RMP strength is called *mode penetration*. Mode penetration is facilitated by high resistivity and slow rotation.

If the RMPs used to control ELMs do not penetrate, the vacuum approximation is clearly invalid. This topic has thus been a subject of intense modelling effort. High resistivity and slow toroidal rotation at the edge seemed to indicate that the perturbations should penetrate, and such was the result of nonlinear MHD modelling [8]. However in H-mode the situation is complicated by the strong gradients in the pedestal. The rotation considered shall be the electron rotation, which has an important diamagnetic component due to the pressure gradient. The electric field associated with the H-mode also

contributes to the rotation and screening of the perturbation. With those effects included, the total electron rotation shall be so fast that perturbation should be mostly screened [61, 62]. Screening of the perturbation would mean that the wide stochastic layer predicted by the vacuum approximation is absent, which would explain the lack of effect on the electron temperature profile. If however the level of screening is different on different machines, it may explain why the effects on ELMs are different despite having reached the DIII-D criterion.

5.5 The role of COMPASS

The COMPASS tokamak, originally from UKAEA Culham, started recently operation in IPP Prague [12]. COMPASS is a small tokamak (major radius $R = 0.56$ m) and has a divertor configuration similar to ITER with a similar aspect ratio, and the ability to enter H-mode. In Culham COMPASS was used for the study of locked modes and mode penetration and is equipped with a rich set of coils for producing magnetic perturbations. In Prague we plan to focus on the edge region [63] and the ELM suppression by RMPs will be among the research topics thanks to the availability of the perturbation coils. One of the main enhancements with respect to the original operation in Culham will be the installation of two neutral beam injectors (NBIs) [64]. The additional heating provided by them may enable us to obtain type I ELMs and so test the ELM mitigation technique directly. Even if type I ELMs are not obtained, we may use the perturbation coils to study the basic physics of the RMPs, especially the unsolved problem of plasma response to RMPs. The toroidal momentum input provided by tangential NBI will be useful for such studies as the toroidal rotation is an important factor. Varying of the momentum input is foreseen by making possible to install one beam in the opposite direction than the other, thus balancing the momentum imparted to the plasma.

Part II

Results

Chapter 6

Particle motion in a perturbed magnetic field

The first topic of the present thesis is the investigation of the difference in field lines and trajectories of the particles from the point of view of the formation of a stochastic layer. It is usually the stochasticity of field lines that is studied (e.g. the studies on relation of the ELM suppression effect to the stochastic layer width, see section 5.3). However the particle transport may be different because they (especially the ions) do not follow precisely the field lines (section 2.1). The question arises if the transition to chaos and the associated transport is not qualitatively different for particle trajectories and field lines. We tried to answer this question by numerically following particle trajectories in a simple model of perturbed toroidal magnetic field. We did the simulations using the full hamiltonian formulation (with three degrees of freedom) of particle motion. There are methods of simplifying the problem by averaging over the fast gyro motion and calculating the trajectory of the particle gyration center (the *drift approximation*). We avoided this method because one reason for different behavior of particle trajectories might be the finite Larmor radius. One inspiration for our work was the fact that in a simple periodic electrostatic potential [65] used to model the electrostatic turbulence (cf. section 3.2.3) the dynamics of ions is very different if drift approximation is not used. In the drift approximation the ions are confined, while using the full hamiltonian their trajectories become chaotic and diffuse across the potential structures [66, 67, 65]. Another factor which might contribute to a difference in field line and particle dynamics is the particle drift (cf. section 2.1) which makes the trajectories deviate from the flux surfaces.

Our results are presented in the following three papers [1, 2, 3]. In addition, the first one presents a summary of the hamiltonian formalism for

field lines (cf. section 4). It should be noted that all the calculations were done for passing particles. The trapped (banana) particles (section 3.2.2) have trajectories completely different from the field lines so a comparison was not considered worthwhile. We thus avoided the parameters corresponding to trapped particles in the velocity scan in the third paper. The third paper also presents a comparison of the impact of chaotic behavior due to the electrostatic turbulence with the magnetic perturbations.

Full Hamiltonian description of the interaction of particles with magnetic islands in tokamak

P. Cahyna

Institute of Theoretical Physics, Faculty of Mathematics and Physics, Charles University, V Holešovičkách 2, 180 00 Praha 8, Czech Republic

L. Krlín

Institute of Plasma Physics, Acad. Sci. CR, Praha, Czech Republic

Received 7 December 2005;
final version 9 March 2006

In this letter, the effect of full Hamiltonian approach to plasma particle dynamics, in the presence of magnetic islands in a tokamak, is discussed. Usually, for the estimation of the diffusion of particles, the stochasticity regime of magnetic field lines is considered as sufficient. We have found that for ions in Hamiltonian description, the diffusive character of their trajectories considerably differs from the diffusive character of magnetic field lines. This then could have, among others, an influence on the performance of the ergodic divertor.

PACS: 52.65.Cc, 52.25.Gj
Key words: plasma, tokamaks, magnetic islands, deterministic chaos

1 Introduction

In the pioneering period of the study of Hamiltonian deterministic chaos, the possibility of generation of chaos of static magnetic field lines was found [1]. This appeared due to the formal identity of equations, describing the geometry of magnetic field lines with the canonical Hamiltonian equations. Such possibility follows from the two following equations:

$$\nabla \cdot \mathbf{B} = 0\,, \quad \mathbf{B} \cdot \nabla\psi = 0\,. \tag{1}$$

Here, $\psi(x)$ is a function which is constant on the magnetic surfaces (specifically, the toroidal flux inside a surface) and the second equation in (1) expresses the tangency of $\mathbf{B}$ to the magnetic surface $\psi(x) = \text{const}$.

The equilibrium magnetic field, which satisfies the condition (1), may be represented by the Clebsch form [2, 3]

$$\mathbf{B} = \nabla\psi \times \nabla\theta^* - \nabla F(\psi) \times \nabla\zeta\,. \tag{2}$$

Here, $F(\psi)$ is the dimensionless poloidal flux and θ^* is the intrinsic coordinate standing for the poloidal angle. (The definition of θ^* will be precised later.) Using the toroidal angle ζ as a running parameter [2, 4], field lines can be represented by the following equations:

$$\frac{\mathrm{d}\psi}{\mathrm{d}\zeta} = -\frac{\partial F}{\partial\theta^*}\,, \quad \frac{\mathrm{d}\theta^*}{\mathrm{d}\zeta} = \frac{\partial F}{\partial\psi}\,. \tag{3}$$

The field line equations have a Hamiltonian structure [2], the role of Hamiltonian is taken over by F, the role of time by ζ. ψ and θ^* represent here canonical variables (ψ as a radial coordinate). In the simplest form, the first term is equal to zero, as F only depends on ψ. The field line dynamics is then regular with ψ and θ^* as action-angle variables. (The magnetic field is considered independent of the physical time.)

In the general non-equilibrium state, the description is still valid, if a dependency of the Hamiltonian F on the variable θ^* is allowed. Due to that, the space development of field lines can have a form of Hamiltonian deterministic chaos, assuming that the corresponding Hamiltonian is non-integrable. This chaotic behavior is a basic property of ergodic divertors. Here, namely, the stochastic behavior of field lines is identified with stochastic behavior of particles, and with their stochastic diffusion [4–6].

Neglecting the drift due to the curvature of field lines, the drift motion of particles can be indeed identified in many cases with the corresponding field lines. A question appears, whether this possibility is general. In the present paper, a difference between the field line and particle behavior is documented, especially, in the simple case of a nonstochastic magnetic field, a particle was found to behave stochastically.

2 Hamiltonian formalism for the behavior of magnetic field lines

We shall start from the standard definition of toroidal coordinates (ζ, θ, r), where θ is the poloidal angle and r is the radius in the poloidal plane. We denote the major radius of the torus by R_0. Using the calibration freedom in the choice of the vector potential $\mathbf{A}$, we can choose it in a form which leads to the Clebsch form of the magnetic field $\mathbf{B}$:

$$\mathbf{A} = A_\theta \nabla\theta + A_\zeta \nabla\zeta\,, \tag{4}$$

$$\mathbf{B} = \nabla A_\theta \times \nabla\theta + \nabla A_\zeta \times \nabla\zeta\,. \tag{5}$$

Our goal is to identify the covariant components of $\mathbf{A}$ with the fluxes ψ and F from the previous section [4]. (The reason is that the meaning of magnetic fluxes is not well defined when the magnetic surfaces cease to exist, because the fluxes are defined as surface functions. On the other hand, the vector potential $\mathbf{A}$ preserves its meaning and will be also used in the particle motion Hamiltonian.) For this, it is useful, instead of the poloidal angle θ, to define a new poloidal coordinate θ^*as a function $\theta^*(r, \theta)$. (Those coordinates are called *intrinsic coordinates* [4].) We require that

$$\theta^*(r, \theta + 2\pi) = \theta^*(r, \theta) + 2\pi\,. \tag{6}$$

The coordinate system (ζ, θ^*, r) is generally non-orthogonal. The θ^*coordinate is chosen so that the covariant components of $\mathbf{A}$ in this coordinate system are: $A_{\theta^*} = \psi$ and $A_\zeta = -F$. We shall outline a proof that such choice of θ^*, A_{θ^*}, and A_ζ is possible. (A more detailed description was presented e.g. in [7].)

Here, $\nabla\theta^*$ is given as

$$\nabla\theta^* = \left(\frac{\partial\theta^*}{\partial\theta}\right)_{\zeta,r}\nabla\theta + \left(\frac{\partial\theta^*}{\partial r}\right)_{\zeta,\theta}\nabla r \tag{7}$$

$$= \left(\frac{\partial\theta^*}{\partial\theta}\right)_{\zeta,r}\frac{\hat{\mathbf{e}}_\theta}{h_\theta} + \left(\frac{\partial\theta^*}{\partial r}\right)_{\zeta,\theta}\hat{\mathbf{e}}_r\,, \tag{8}$$

where $(\hat{\mathbf{e}}_\zeta, \hat{\mathbf{e}}_\theta, \hat{\mathbf{e}}_r)$ is the orthonormal basis, connected with the geometrical basis $(\mathbf{e}_\zeta, \mathbf{e}_\theta, \mathbf{e}_r)$ by means of the transformation

$$\begin{aligned}\mathbf{e}_\zeta &= h_\zeta\hat{\mathbf{e}}_\zeta\,,\\ \mathbf{e}_\theta &= h_\theta\hat{\mathbf{e}}_\theta\,,\\ \mathbf{e}_r &= \hat{\mathbf{e}}_r\,.\end{aligned}$$

(See Appendix for the definition of the coefficients h_i.)

Assuming that the A_{θ^*} component is independent of the toroidal angle, that is, $(\partial A_{\theta^*}/\partial\zeta)_{\theta,r} = 0$, the magnetic field $\mathbf{B}$ is given as

$$\begin{aligned}\mathbf{B} &= \nabla A_{\theta^*}\times\nabla\theta^* + \nabla A_\zeta\times\nabla\zeta\\ &= \frac{\partial(A_{\theta^*},\theta^*)}{\partial(r,\theta)}\hat{\mathbf{e}}_r\times\frac{\hat{\mathbf{e}}_\theta}{h_\theta} + \left(\left(\frac{\partial A_\zeta}{\partial r}\right)_{\zeta,\theta}\hat{\mathbf{e}}_r + \left(\frac{\partial A_\zeta}{\partial\theta}\right)_{\zeta,r}\frac{\hat{\mathbf{e}}_\theta}{h_\theta}\right)\times\frac{\hat{\mathbf{e}}_\zeta}{h_\zeta}\\ &= \frac{\partial(A_{\theta^*},\theta^*)}{\partial(r,\theta)}\frac{\hat{\mathbf{e}}_\zeta}{h_\theta} - \left(\frac{\partial A_\zeta}{\partial r}\right)_{\zeta,\theta}\frac{\hat{\mathbf{e}}_\theta}{h_\zeta} + \left(\frac{\partial A_\zeta}{\partial\theta}\right)_{\zeta,r}\frac{\hat{\mathbf{e}}_r}{h_\theta h_\zeta}\\ &= \frac{1}{h_\theta h_\zeta}\left(\frac{\partial(A_{\theta^*},\theta^*)}{\partial(r,\theta)}\mathbf{e}_\zeta - \left(\frac{\partial A_\zeta}{\partial r}\right)_{\zeta,\theta}\mathbf{e}_\theta + \left(\frac{\partial A_\zeta}{\partial\theta}\right)_{\zeta,r}\mathbf{e}_r\right),\end{aligned} \tag{9}$$

where $\partial(A_{\theta^*},\theta^*)/\partial(r,\theta)$ is the Jacobi determinant.

Using the transformation between (ζ,θ,r) and (ζ,θ^*,r) we get the following expression for components of $\mathbf{B}$ in the basis $(\mathbf{e}_\zeta{}', \mathbf{e}_{\theta^*}{}', \mathbf{e}_r{}')$ of the (ζ,θ^*,r) coordinate system:

$$\mathbf{B} = \frac{1}{h_\theta h_\zeta}\left(\frac{\partial\theta^*}{\partial\theta}\right)_{\zeta,r}\left(\left(\frac{\partial A_{\theta^*}}{\partial r}\right)_{\zeta,\theta^*}\mathbf{e}_\zeta{}' - \left(\frac{\partial A_\zeta}{\partial r}\right)_{\zeta,\theta^*}\mathbf{e}_{\theta^*}{}' + \left(\frac{\partial A_\zeta}{\partial\theta^*}\right)_{\zeta,r}\mathbf{e}_r{}'\right). \tag{10}$$

The components of $\mathbf{B}$ can be interpreted as derivatives of the coordinates of a field line with respect to a suitable parameter ξ (which is related to the length parameter s by $\mathrm{d}\xi/\mathrm{d}s = \|\mathbf{B}\|$). The differential equations of the field line are then

$$\begin{aligned}\frac{\mathrm{d}\zeta}{\mathrm{d}\xi} &= \frac{1}{h_\theta h_\zeta}\left(\frac{\partial\theta^*}{\partial\theta}\right)_{\zeta,r}\frac{\partial A_{\theta^*}}{\partial r}\,,\\ \frac{\mathrm{d}\theta^*}{\mathrm{d}\xi} &= -\frac{1}{h_\theta h_\zeta}\left(\frac{\partial\theta^*}{\partial\theta}\right)_{\zeta,r}\frac{\partial A_\zeta}{\partial r}\,,\\ \frac{\mathrm{d}r}{\mathrm{d}\xi} &= \frac{1}{h_\theta h_\zeta}\left(\frac{\partial\theta^*}{\partial\theta}\right)_{\zeta,r}\frac{\partial A_\zeta}{\partial\theta^*}\,.\end{aligned}$$

Using the first equation, we can eliminate the parameter ξ and use ζ as the field line parameter instead:

$$\frac{\mathrm{d}\theta^*}{\mathrm{d}\zeta} = -\frac{\partial A_\zeta}{\partial r}\left(\frac{\partial A_{\theta^*}}{\partial r}\right)^{-1}, \tag{11}$$

$$\frac{\mathrm{d}r}{\mathrm{d}\zeta} = \frac{\partial A_\zeta}{\partial \theta^*}\left(\frac{\partial A_{\theta^*}}{\partial r}\right)^{-1}. \tag{12}$$

Taking the coordinate A_{θ^*} as the radial coordinate instead of r and transforming equations (11), (12) to the $(\zeta, \theta, A_{\theta^*})$ coordinate system, we obtain the differential equations for the magnetic field lines in the form

$$\frac{\mathrm{d}\theta^*}{\mathrm{d}\zeta} = -\frac{\partial A_\zeta}{\partial A_{\theta^*}}, \tag{13}$$

$$\frac{\mathrm{d}A_{\theta^*}}{\mathrm{d}\zeta} = \frac{\partial A_\zeta}{\partial \theta^*}. \tag{14}$$

We recognize the Hamiltonian form of equations (3) presented above, with the desired meaning of the components of $\mathbf{A}$: $A_{\theta^*} = \psi$ and $A_\zeta = -F$ (up to additive constants). To prove that such identification of vector potential components with fluxes is possible, we shall consider a toroidally symmetrical case, where A_ζ is independent of ζ. It is then possible to choose θ^* so that A_ζ only depends on A_{θ^*} [3]. Equation (14) is then zero, so the field line remains in a surface of constant A_ζ and A_{θ^*}, which is then a magnetic surface and A_ζ and A_{θ^*} are surface functions. The toroidal flux ψ, being defined as the flux of the toroidal component of $\mathbf{B}$ inside a magnetic surface [3, 8], can be expressed as a surface integral

$$\psi = \frac{1}{2\pi}\int_{\Sigma_\mathrm{t}} \mathbf{B}\cdot\mathrm{d}\mathbf{S}, \tag{15}$$

where the surface Σ_t is a section of the poloidal plane contained in the chosen magnetic surface. Using $\mathbf{B} = \nabla\times\mathbf{A}$ and the Stokes theorem, we get

$$\psi = \frac{1}{2\pi}\oint_\xi \mathbf{A}\cdot\mathrm{d}\mathbf{s}, \tag{16}$$

with the curve ξ being the boundary of Σ_t and $\mathrm{d}\mathbf{s}$ being the line element. Only the $A_{\theta^*}\nabla\theta^*$ component contributes to this integral, as the projection of $A_\zeta\nabla\zeta$ to the poloidal plane vanishes. The differential of θ^* corresponding to $\mathrm{d}\mathbf{s}$ is $\mathrm{d}\theta^* = \nabla\theta^*\cdot\mathrm{d}\mathbf{s}$; thus, Eq. (16) can be expressed as

$$\psi = \frac{1}{2\pi}\int_0^{2\pi} A_{\theta^*}\mathrm{d}\theta^* = A_{\theta^*}, \tag{17}$$

where the integral was substituted by a simple multiplication. As A_{θ^*} is constant on a magnetic surface, it is also constant on the curve ξ. To prove that the poloidal

flux surface function F, defined analogically to ψ as the flux of the poloidal field inside a magnetic surface, is equivalent to $-A_\zeta$, we can compare equation (13) with the usual equation [8]

$$\frac{\mathrm{d}\theta^*}{\mathrm{d}\zeta} = \frac{\mathrm{d}F}{\mathrm{d}\psi}\,. \tag{18}$$

From the comparison we see that F is equal to $-A_\zeta$ up to an additive constant which is not important in the case of vector potential.

The meaning of ψ and F variables can now be extended to the case where magnetic surfaces do not exist so the flux functions are not well defined. We note $\psi = A_{\theta^*}$ and $F = -A_\zeta$. (Those variables usually continue to be called toroidal and poloidal fluxes.)

The explicit form of equations requires a choice of the toroidal and poloidal magnetic fields. For the toroidal field, we choose the standard form [3]

$$B_\mathrm{t} = \frac{B_0}{1 + \dfrac{r}{R_0}\cos\theta} \approx B_0\left(1 - \frac{r}{R_0}\cos\theta\right) \tag{19}$$

(in the following we shall use the linear approximation). The poloidal field is given by the function $F(\psi)$.

From equation (19) and the assumption of circular cross section of magnetic surfaces it follows that the toroidal flux is given as

$$\psi(r) = \tfrac{1}{2}B_0 r^2\,. \tag{20}$$

To obtain this toroidal field we choose the function θ^* in the approximate form

$$\theta^*(\theta, r) = \theta - \frac{r}{R_0}\sin\theta \tag{21}$$

and the function ψ as (20). (To verify that (21) and (20) lead to (19), we note that from the third line of (9) follows that $B_\mathrm{t} = [\partial(A_{\theta^*}, \theta^*)/\partial(r,\theta)]h_\theta^{-1}$, and for a circular cross section $\partial(A_{\theta^*}, \theta^*)/\partial(r,\theta) = (\mathrm{d}\psi/\mathrm{d}r)\partial\theta^*/\partial\theta$.)

Using the definition of the safety factor q [2, 8],

$$q = \frac{\mathrm{d}\psi}{\mathrm{d}F}\,, \tag{22}$$

the function $F(\psi)$ is given as

$$F(\psi) = \int q^{-1}\mathrm{d}\psi\,. \tag{23}$$

This description is valid in the equilibrium case, when every field line remains on a 2-dimensional magnetic surface. To introduce effects of magnetic islands, we shall choose the poloidal flux function according to [2, 4] in a perturbed form

$$F(\psi, \theta, \zeta) = F_0(\psi) + L\delta F(\psi, \theta^*, \zeta)\,, \tag{24}$$

where L is the small parameter representing the perturbation created by a system of magnetic islands and F_0 is the unperturbed part introduced above (Eq. (23)). The perturbation can be expressed in a Fourier form

$$\delta F(\psi, \theta^*, \zeta) = \sum_{(m,n)} \delta F_{m,n}(\psi) \cos(m\theta^* - n\zeta + \phi_{m,n}) . \tag{25}$$

The choice of integers m, n then determines a periodic chain of magnetic islands.

3 Hamiltonian formalism for particle dynamics in a system of magnetic islands

Motion of charged particles in a magnetic field is generally described by the Hamiltonian[1])

$$H(\mathbf{p}, \mathbf{q}) = \frac{1}{2M} \left((p_\zeta - eA_\zeta)^2 g^{\zeta\zeta} + (p_\theta - eA_\theta)^2 g^{\theta\theta} + (p_r - eA_r)^2 \right) . \tag{26}$$

(In this paper we only deal with single-particle motion in a magnetic field, not taking into account the particle collisions and the electrostatic potential.)

Here, M and e are mass and charge of the particle, respectively, p_i are generalized momentum and g^{ii} are components of the metric tensor. The generalized coordinates q_i are the toroidal coordinates ζ, θ, and r. Since the toroidal system is orthogonal, the metric tensor is diagonal.

In the previous section we choose a particular form of the potential $\mathbf{A}$ in the coordinates ζ, θ^*, and r. Using again the magnetic flux notation $\psi \equiv A_{\theta^*}$ and $F \equiv -A_\zeta$ and transforming to the (ζ, θ, r) coordinates, we may express the final form of the Hamiltonian with this potential as

$$\begin{aligned} H(\mathbf{p}, \mathbf{q}) = \frac{1}{2M} \left[(p_\zeta + eF)^2 g^{\zeta\zeta} + \left(p_\theta - e\psi \left(1 - \frac{r}{R_0} \cos\theta \right) \right)^2 g^{\theta\theta} \right] \\ + \frac{1}{2M} \left(p_r + e\psi \frac{\sin\theta}{R_0} \right)^2 . \end{aligned} \tag{27}$$

Substituting for $g^{\theta\theta}$ and for ψ using formula (20), the corresponding equations of motion are

$$\frac{\mathrm{d}\zeta}{\mathrm{d}t} = \frac{1}{M}(p_\zeta + eF) g^{\zeta\zeta} , \tag{28}$$

$$\frac{\mathrm{d}\theta}{\mathrm{d}t} = \frac{p_\theta}{Mr^2} - \frac{eB_0}{2M} \left(1 - \frac{r}{R_0} \cos\theta \right) , \tag{29}$$

$$\frac{\mathrm{d}r}{\mathrm{d}t} = \frac{p_r}{M} + \frac{eB_0 r^2 \sin\theta}{2MR_0} , \tag{30}$$

[1]) See Appendix for the explicit form of the metric components g^{ii}.

$$\frac{\mathrm{d}p_\zeta}{\mathrm{d}t} = -\frac{e}{M}(p_\zeta + eF)\frac{\partial F}{\partial \zeta}g^{\zeta\zeta}\,, \tag{31}$$

$$\begin{aligned}\frac{\mathrm{d}p_\theta}{\mathrm{d}t} = &-\frac{e}{M}(p_\zeta + eF)\frac{\partial F}{\partial \theta}g^{\zeta\zeta} - \frac{1}{2M}(p_\zeta + eF)^2\frac{\partial g^{\zeta\zeta}}{\partial \theta} \\ &+ \left[\frac{p_\theta}{r^2} - \frac{eB_0}{2}\left(1 - \frac{r}{R_0}\cos\theta\right)\right]\frac{eB_0 r^3 \sin\theta}{2MR_0} \\ &- \left(p_r + \frac{eB_0 r^2 \sin\theta}{2R_0}\right)\frac{eB_0 r^2\cos\theta}{2MR_0}\,,\end{aligned} \tag{32}$$

$$\begin{aligned}\frac{\mathrm{d}p_r}{\mathrm{d}t} = &-\frac{1}{2M}\left((p_\zeta + eF)^2\frac{\partial g^{\zeta\zeta}}{\partial r}\right. \\ &- 2\frac{p_\theta^2}{r^3} + eB_0 p_\theta\frac{\cos\theta}{R_0} + \frac{e^2B_0^2 r}{2} \\ &\left.- \frac{3e^2B_0^2r^2\cos\theta}{2R_0} + \frac{e^2B_0^2r^3\cos^2\theta}{R_0^2}\right) \\ &- \frac{e}{M}(p_\zeta + eF)\frac{\partial F}{\partial r}g^{\zeta\zeta} - \frac{e}{M}\left(p_r + \frac{eB_0r^2\sin\theta}{2R_0}\right)\frac{B_0 r\sin\theta}{R_0}\,.\end{aligned} \tag{33}$$

In this system, only the function F has to be defined. The unperturbed part F_0 depends on the q radial profile (see Eq. (23), which in turn depends on the current profile. The perturbed part defines the form of magnetic islands.

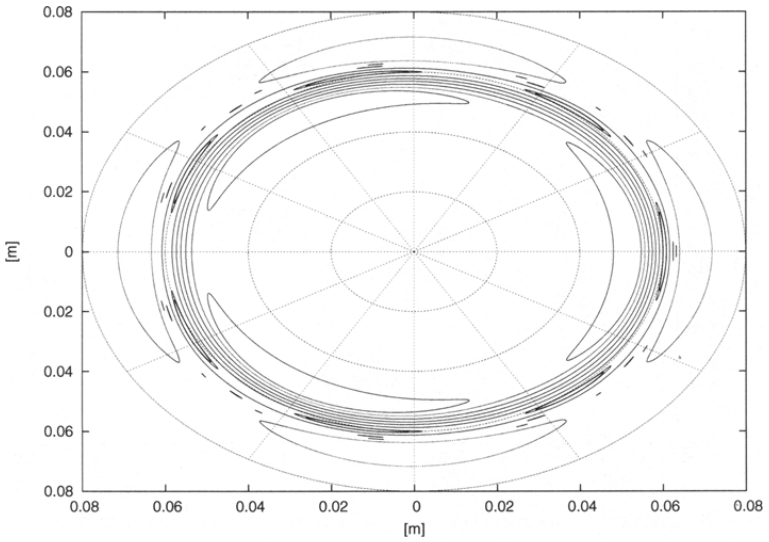

Fig. 1. Magnetic surfaces in the system of two-island chains, $q = 3$ and $q = 4$: $L = 0.0007$.

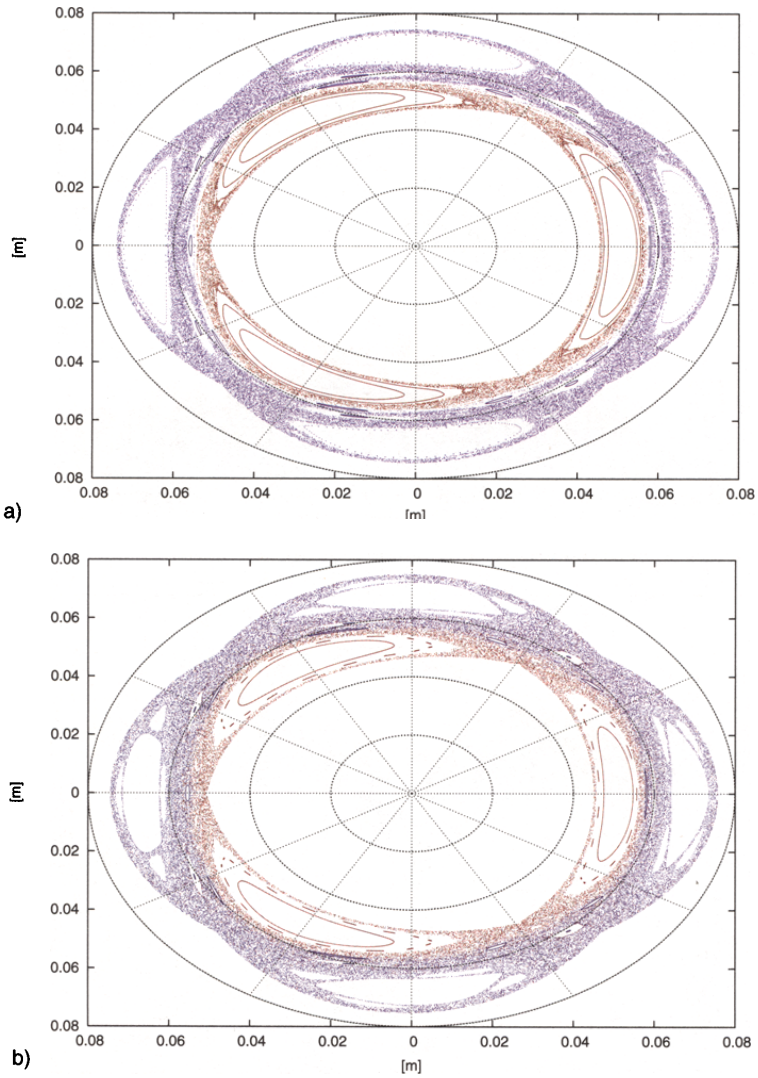

Fig. 2. Stochasticity of magnetic field lines in the system of two-island chains, $q = 3$ and $q = 4$: a) $L = 0.0017$, b) $L = 0.0020$.

4 Numerical simulations of field lines and particle trajectories

To compare the difference between particle and field line dynamics, we computed trajectories of both of them and examined their intersection with a poloidal plane (perpendicular to the minor axis of the torus). For field lines, this cross section is directly the Poincaré surface of section. For the computation the Runge–Kutta method, as implemented by the `ode45` subroutine of the Matlab package, was used to integrate the differential equations of the field line (3) and of the particle trajectory (28)–(33).

The equations must be completed by a choice of the function F. We derive the unperturbed part F_0 from the expression of q given in [2] for a parabolic density profile. From this assumption, a profile of q in the form

$$q(x) = \frac{4}{w(2-x^2)(2-2x^2+x^4)} \tag{34}$$

is derived in the cited work, where $x \equiv r/a$ is a dimensionless radial coordinate (a is the minor radius of the tokamak). The parameter w determines the value of q at the edge. The F_0 profile is then given by the integral (23). For the parameters, we used values of the CASTOR tokamak (see e.g. [10]): major radius $R_0 = 0.4$ m, minor

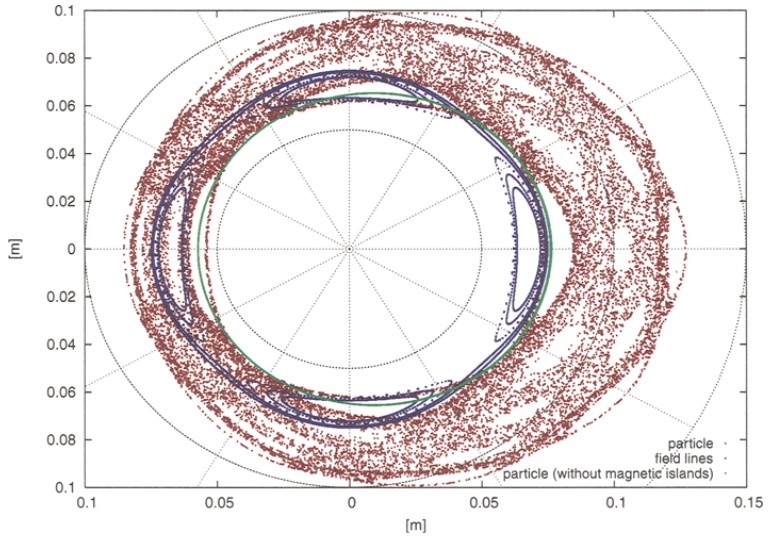

Fig. 3. Magnetic field lines (blue) and stochasticity of particle trajectory (red) in one magnetic island chain for $q = 4$, and nonstochastic motion of a particle without magnetic islands (green), all for energy of particles 20 eV and for CASTOR parameters.

radius $a = 0.1\,\mathrm{m}$, and central toroidal magnetic field $B_0 = 1\,\mathrm{T}$. The parameter w was set to $1/2$, corresponding to $q = 8$ at the edge.

For the perturbation field we choose the simplest model where magnetic islands can appear. This is already satisfied for a single Fourier component of the perturbation (25). We choose $m = 4$ and $n = 1$, corresponding to one magnetic island which appears as four structures in the poloidal plane in the area where the field lines are resonant with the perturbation. We further choose a quadratic dependency of F on the radial coordinate r, which leads to a linear increase of the perturbation field with r. The complete expression for the perturbation is then

$$\delta F(\psi, \theta^*, \zeta) = \psi \cos(4\theta^* - \zeta). \tag{35}$$

For field lines, this Hamiltonian is integrable, as could be demonstrated by a canonical transformation to suitable action-angle variables. (The system is equivalent to the dynamics of a pendulum.) Therefore, there is no chaos in the field line dynamics in this case. For particles, the answer is not *a priori* clear.

To demonstrate the effect of chaos in magnetic field lines, we choose another perturbation with two harmonic components

$$\delta F(\psi, \theta^*, \zeta) = \psi(\cos(4\theta^* - \zeta) + \cos(3\theta^* - \zeta))\,. \tag{36}$$

Such Hamiltonian leads to formation of two different chains of magnetic islands, three- and four-island structures in the poloidal plane. In Figs. 1 and 2, results for three values of the stochasticity parameter L are presented, each of which was computed for several initial values and for 20000 turns of each field line around the major axis. Figure 1 shows the poloidal section for $L = 0.0007$. The perturbation is not sufficiently strong for stochasticity to appear, all plotted field lines remain on magnetic surfaces. For $L = 0.0017$, areas of stochasticity around island chains appear (Fig. 2a). Two sets of initial conditions were distinguished by color, one closer to the minor axis (red) and one farther (blue). We can see that there is no remarkable mixing between those two areas. The boundary marks a remaining magnetic surface (*KAM torus* after Kolmogorov, Arnold, and Moser) acting as an impenetrable barrier [11]. Finally, for even greater value of $L = 0.002$, the two areas merge in a large chaotic "sea" (Fig. 2b). Similar results already appeared in numerous papers (see e.g. [2, 9]), usually using the method of Poincaré mappings.

To investigate the main topic of our work, which concerns comparison of field lines with particle trajectories (discussed in Hamiltonian approach from Sect. 3), we return to the one-island case given by Eq. (35). Even in this simple model, interesting results can be derived. In particular, a chaotic regime in particle dynamics appears, contrary to field lines regularity. Particles chosen were singly-ionized ions of carbon.

In the integration of the particle motion, choice of the time step is important. A distinctive feature of the motion of a charged particle in a magnetic field is the Larmor gyration with the frequency eB/M. To obtain a faithful picture of the particle motion including the Larmor circles, the time step must be smaller than the Larmor gyration period. We used $1/12$ of the Larmor period as the maximum time

step. This value was determined empirically: for larger values we observed significant loss of energy during computations. (Since the Hamiltonian is conservative, conservation of energy can be used to check accuracy.)

Figure 3 presents the intersection of both the particle trajectory and several field lines with the poloidal plane. 20000 intersections were plotted. In the case of a particle, we plot the position of gyration center, not the actual particle position. The particle energy is 10 eV for both the perpendicular and parallel energy. An important and clearly visible feature is the particle drift with the velocity [12]

$$\mathbf{v}_{\mathrm{d}} = \frac{M}{e}\frac{\mathbf{R}\times\mathbf{B}}{B^2R^2}\left(v_{\parallel}^2 + \frac{1}{2}v_{\perp}^2\right), \tag{37}$$

where $v_{\parallel}$ and $v_{\perp}$ are respectively the parallel and perpendicular velocities and $\mathbf{R}$ describes the actual particle position relative to the major axis. Due to the cross product in (37), the drift velocity has a vertical direction. If the particle is above the poloidal plane, this drift has a radial component oriented to the minor axis, and causes a decrease of the r coordinate. After the particle passes below the poloidal plane, the drift will carry it away from the minor axis, that is, the r coordinate increases. After one turn in the poloidal direction, the particle will return to the same position in the poloidal plane (but not necessarily to the same toroidal position ζ) where it started. This cancellation of drift is one of the reasons why a helically curved field is necessary in a toroidal configuration. As the drift carries the particle to the center of the poloidal plane, when it moves from the outer side to the inner side (the poloidal movement is counterclockwise in 4), and to the edge, when it returns, it results in a shift of the trajectory to the outer side relative to the center of symmetry and to the field lines, which do not exhibit this behavior. This shift is well visible in the figure. To illustrate the effect of the drift more clearly, we also plotted the case without magnetic islands ($L = 0$), where the particle motion is regular.

As was said above, field lines show no stochasticity at all in the one-island case. Thus the presence of strong stochasticity for particles in this case is remarkable. Particle motion shows a chain of four islands corresponding to the one seen in the field line dynamics, but there are also the 5-island, 6-island chains, and so on. All those island chains merge to form a large stochastic sea extending beyond the edge of the torus. We did not include the effect of the edge in our model, but rather extended the model beyond the edge, setting the current density to 0 outside. Overlap of trajectories with the edge (located at $r = 0.1$ m) gives an idea about the importance of particle transport towards the edge, where, in reality, they would be stopped.

To find more about the mechanism of this surprising result, we carried more computations for different models. A question appears, whether the difference between particle and field line dynamics is caused by the Larmor gyration of the particles, or is due to the drift motion. To distinguish between those two effects, we choose a model totally neglecting the toroidal curvature. Instead of a toroidal

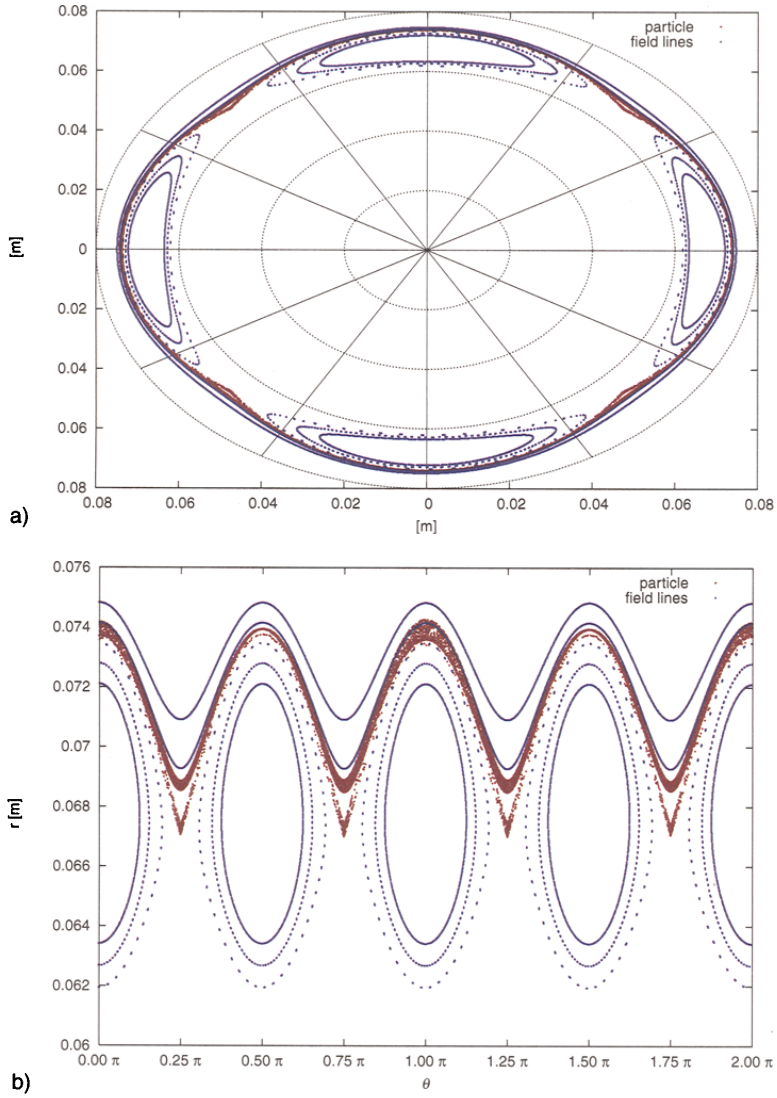

Fig. 4. Magnetic field lines (blue) and a particle trajectory (red) in cylindrical model, using Cartesian (a) and cylindrical (b) coordinates.

system, we consider a cylindrical geometry with periodic boundary conditions. If a particle or field line leaves at one face of the cylinder, it is returned at the other face. In this way, we simulate a toroidal configuration in which the effects of curvature are excluded. In spite of the fact that this model is unrealistic, it allows us to estimate the effect of drift, as drift is virtually nonexistent in such field. Results are shown in Fig. 4a, where the positions of the particle gyration center and field lines are plotted. Despite the changed geometry, the parameters are identical to the toroidal case. We see that the picture for gyration centers is similar to the one of field lines — there is no offset due to drift motion, and also, there is no visible stochasticity. Figure 4b shows the same, but in cylindrical coordinates, with the poloidal angle θ on horizontal axis and radial coordinate r on vertical axis.

Those results show that stochasticity is caused by the interaction between magnetic islands and drift motion. From the previous paragraph it follows that magnetic islands alone do not lead to stochasticity in a model without drift motion, and the result for a case without magnetic perturbation (as shown in Fig. 3) shows that the drift motion alone is also regular.

5 Summary

In widely used approach of taking into account only magnetic field lines dynamics, at least two-island chains are necessary for chaotic behavior of field lines. Contrary to that, we have found that in a more precise Hamiltonian description of charged particle motion, chaos appears already in the case of one-island chain.

We shall discuss this phenomena more thoroughly in a following paper, together with examination of differences in more complicated cases, such as two-island chains.

Appendix: Metric of a toroidal coordinate system

In the toroidal coordinate system (ζ, θ, r), the contravariant components of the metric tensor are

$$\begin{aligned} g^{\zeta\zeta} &= \frac{1}{(R_0 + r\cos\theta)^2}\,, \\ g^{\theta\theta} &= \frac{1}{r^2}\,, \\ g^{rr} &= 1 \end{aligned}$$

and the coefficients h_i which express lengths of the base vectors are

$$\begin{aligned} h_\zeta &= (g^{\zeta\zeta})^{-1/2} = R_0 + r\cos\theta\,, \\ h_\theta &= (g^{\theta\theta})^{-1/2} = r\,, \\ h_r &= (g^{rr})^{-1/2} = 1\,. \end{aligned}$$

This work was supported by the grant of the Academy of Sciences of the Czech Republic IAA100430502.

Numerical simulations were carried out with facilities contributed by the School of Computer Science, Faculty of Mathematics and Physics, Charles University, Prague.

References

[1] M.N. Rosenbluth, R.Z. Sagdeev, J.B. Taylor, and G.M. Zaslavskii: Nucl. Fusion **6** (1966) 207.

[2] J.H. Misguich, J.-D. Reuss, D. Constantinescu, G. Steinbrecher, M. Vlad, F. Spineau, B. Weyssow, and R. Balescu: *EUR-CEA-FC Report 1724*. Cadarache, 2002.

[3] R. Balescu: *Transport processes in plasmas*. North Holland, Amsterdam, 1988.

[4] Ph. Ghendrih, H. Capes, F. Nguyen, and A. Samain: Contrib. Plasma Phys. **32** (1992) 179.

[5] A. Samain, A. Grosman, and W. Feneberg: J. Nucl. Mater. **111/112** (1982) 408.

[6] A. Samain, T. Blenski, Ph. Ghendrih, and A. Grosman: Contrib. Plasma Phys. **30** (1990) 157.

[7] P. Cahyna: Diploma thesis. Charles University, Faculty of Mathematics and Physics, Prague, 2005.

[8] J. Wesson: *Tokamaks*. Oxford Science Publications, Clarendon Press, Oxford, 1987.

[9] R. Balescu, M. Vlad, and F. Spineau: Phys. Rev. E **58** (1998) 951.

[10] K. Dyabilin, R. Klíma, I. Ďuran, J. Horáček, M. Hron, P. Pavlo, J. Stöckel, and F. Žáček: Czech. J. Phys. **51** (2001) 1107.

[11] A.J. Lichtenberg and M.A. Lieberman: *Regular and chaotic dynamics*, 2nd edition. Springer-Verlag, New York, 1992.

[12] F.F. Chen: *Introduction to Plasma Physics*. Plenum Press, New York, 1977.

Particle diffusion in a system of magnetic islands in tokamaks in fully Hamiltonian approach

L. Krlín

Institute of Plasma Physics, Acad. Sci. of the Czech Republic,
Za Slovankou 3, 141 00 Prague 8, Czech Republic
e-mail: krlin@ipp.cas.cz

P. Cahyna

Institute of Theoretical Physics, Faculty of Mathematics and Physics, Charles University,
V Holešovičkách 2, 180 00 Prague 8, Czech Republic
e-mail: pavel.cahyna@st.mff.cuni.cz

Received 26 April 2006

Particle dynamics in a system of magnetic islands is studied. It is shown that fully Hamiltonian description of particle dynamics yields results different from those obtained in field lines description.

PACS: 52.65.Cc, 52.25.Gj
Key words: tokamaks, magnetic islands, deterministic chaos, drift

1 Introduction

Idea of ergodic divertor awoke an interest in stochastic behavior of magnetic field lines in some magnetic systems. The first discussion of this phenomenon goes back to Rosenbluth et al. [1]. Intensive studies of ergodic divertors for Tore Supra and Textor proved the effectiveness of this method for the extraction of undesirable ions from the plasma. The method consists in the chaotization of magnetic lines which are close to the first wall, and, consequently, in the chaotization of particles, coupled to the field line system.

Chaotization is here performed by means of an artificial resonant generation of a set of mutually overlapping magnetic islands at rational surfaces. The chaotization of field lines is then a result of non–integrability of the dynamics of field lines in such magnetic systems.

It is of some interest to compare the threshold for the chaotic field lines geometry and particles behavior in such chaotic field line system. Generally, it is expected that a particle remains close to its field line. There are two reasons why particles may not follow it. Both are caused by the fact that Hamiltonian description of particles trajectories (as a more exact solution of particle dynamics) is close to the field line system only for the homogeneous magnetic field. For a non–homogeneous magnetic field, important drifts appear and force the particle to move far from the field line. (First informations appeared in [2]). Secondly, in a full Hamiltonian approach, the particle exhibits Larmor motion. This could form a nonlinear coupled system with the perturbation of the magnetic field which creates the magnetic islands.

Such coupling could possibly lead to effects which the field line description or drift approximation could not describe.

In the paper, both effects are discussed. For a set of used parameters, the effect of the drift in non–homogeneous magnetic field dominates. The effect of mutual influence of the Larmor motion and the field of magnetic islands was for our parameters not recognizable.

We consider the case when magnetic islands appear as a perturbation of the basic magnetic field of a tokamak, generated resonantly at some rational surfaces. We assume that the amplitudes of magnetic islands can be changed in some region. The basic drift is caused by the curvature of toroidal field lines. To realize the effect of this drift, we compare this dynamics with an equivalent case without the effect of the curvature (and, therefore, without this drift) in an equivalent cylindrical approximation.

First results of our study appeared in the paper [2]. There, we discussed the dynamics of particles, influenced in the tokamak magnetic field by one magnetic island. We found there that the effect of the vertical drift, caused by the curvature of the toroidal magnetic field lines is very important and changes a bit the contemporary expectations. That paper also contains a more thorough discussion and proofs of the facts that we briefly summarize in the next section.

Our present paper can be considered as a continuation of [2]. The goal is to extend the study of the dynamics of particles in the tokamak magnetic field to the case two magnetic islands, which has important qualitative differences compared to the case of one island. We also explored the range of parameters (especially the perpendicular and parallel energies) more systematically.

Our paper is organized as follows: Section 2 summarizes the formalism used, Section 3 describes the models investigated and the method used and Section 4 describes the results obtained.

2 Hamiltonian description of field lines and particles

It is a long known fact that magnetic field lines in a toroidal geometry (such as that of a tokamak) can be described by equations formally identical to the Hamilton equation of motion [3, 4]:

$$\frac{\mathrm{d}\psi}{\mathrm{d}\zeta} = -\frac{\partial F}{\partial \theta^*};\ \frac{\mathrm{d}\theta^*}{\mathrm{d}\zeta} = \frac{\partial F}{\partial \psi}\,. \tag{1}$$

Here, the poloidal flux F represents the Hamiltonian, the intrinsic poloidal angle θ^* and the toroidal flux ψ are the conjugate position and momentum and the toroidal angle ζ has the role of time. The poloidal and toroidal fluxes can be identified with components of the vector potential: $A_{\theta^*} = \psi$ and $A_\zeta = -F$.

(For a more thorough discussion of the above stated facts we refer e.g. to the previous paper [2].)

In an equilibrium configuration, F depends only on ψ as $\frac{\mathrm{d}\psi}{\mathrm{d}F} = q$, where q is the safety factor. The equations (1) are then integrable and magnetic surfaces

originate. For internal (turbulence) or external (divertors) reasons, the field can be perturbated. Such perturbation can be expressed by adding a term δF to the Hamiltonian:

$$F(\psi,\theta,\zeta) = F_0(\psi) + L\delta F(\psi,\theta^*,\zeta)\,, \tag{2}$$

L is a dimensionless parameter expressing the magnitude of the perturbation.

The added perturbation can cause nonintegrability of the Hamiltonian, with the possibility of appearance of deterministic chaos. For the study of chaos, it is convenient to decompose δF in a Fourier series:

$$\delta F(\psi,\theta^*,\zeta) = \sum_{(m,n)} \delta F_{m,n}(\psi)\cos(m\theta^* - n\zeta + \phi_{m,n})\,. \tag{3}$$

Every term in the series can resonate with a value of q equal to m/n, creating a a chain of magnetic islands. Chaotic regions usually appear first at the separatrix surface which separates the island from the magnetic surfaces around it.

For the case of magnetic surfaces with a circular cross–section, the θ^* and ψ coordinates are related to the toroidal coordinate system (ζ,θ,r) as: $\theta^*(\theta,r) = \theta - r/R_0\sin\theta$ and $\psi(r) = B_0 r^2/2$.

A charged particle in this magnetic field moves according to a Hamiltonian

$$\begin{aligned} H(\mathbf{p},\mathbf{q}) &= \frac{1}{2M}\left((p_\zeta + eF)^2 g^{\zeta\zeta} + (p_\theta - e\psi(1 - r/R_0\cos\theta))^2 g^{\theta\theta}\right) + \\ &\quad + \frac{1}{2M}\left(p_r + e\psi\frac{\sin\theta}{R_0}\right)^2\,, \end{aligned} \tag{4}$$

where (p_ζ, p_θ, p_r) are the generalized momentum conjugate to (ζ,θ,r) and g^{ii} are components of the metric tensor. The equations of motion can be obtained by differentiating the Hamiltonian. This has been done explicitly in [2].

3 Methods used for comparing field lines and particle trajectories

We integrated numerically the differential equations of the field line and the canonical equations of a charged particle. The intersections of field lines and trajectories of gyration centers of particles with a poloidal plane were plotted. The resulting figures were used for the comparison of field line and particle behavior.

The calculations were done for a model of the magnetic field with two Fourier components of the perturbation, one with $m = 3$ and $n = 1$ and the other with $m = 4$ and $n = 1$. This perturbation gives two magnetic islands, located at the value of $q = 3$ and $q = 4$, because there the field lines are resonant with the perturbation. In the poloidal cross–section, they appear as two chains of three and four island structures encircling the minor axis of the torus. The perturbation δF depends quadratically on the radial coordinate r. The corresponding perturbation of $\mathbf{B}$ then grows linearly from the minor axis towards the edge. The expression for the perturbation is then

$$\delta F(\psi,\theta^*,\zeta) = \psi\left(\cos(4\theta^* - \zeta) + \cos(3\theta^* - \zeta)\right)\,. \tag{5}$$

This perturbation was chosen to be as simple as possible, while having specific properties from the point of view of the chaos theory. It is known to lead to chaotic behavior of field lines, which manifests itself mainly in the separatrix regions of the island chains. It is also known that a transition to a global chaos can occur, where the field lines starting at one island chain can reach the area of the other island chain. This happens approximately when the perturbation is so large that the islands chains become wide enough for their stochastic separatrix regions to overlap. This is called the *Chirikov criterion*. As this result holds for field lines, we were interested if there are significant differences for particle trajectories.

In the previous paper [2], we also used a perturbation with only one Fourier component. It leads to an integrable Hamiltonian for the field lines, because a canonical transformation can transform it to a system equivalent to a pendulum. This makes such a system an interesting point for comparison of field line and particle dynamics, because the field lines do not show chaotic behavior, while for particles, the possibility of nonintegrability and chaos can not be ruled out.

The actual parameters used for the computations were: major radius $R_0 = 0.4$ m, minor radius $a = 0.1$ m, and toroidal magnetic field at the minor axis $B_0 = 1$ T. Those are the parameters of the CASTOR tokamak (see e.g. [5]). The edge value of q was 8. The particle mass and charge were chosen equal to those of a singly–ionized ion of carbon. For a numerical solution of a particle performing cyclotron motion, the time step must be sufficiently smaller than the Larmor gyration period. We chose 1/12 of the Larmor period $2\pi/\omega_c$ as the maximum integration time step. The accuracy of computation was checked by comparing the final energy to the original values. For an exact solution, they would be equal, as the particle Hamiltonian is conservative. For both field lines and particles, we obtained 20 000 intersections with the poloidal plane for every initial condition.

As a characteristic property of charged particle motion is the drift of the gyration center relative to the field lines, we were interested in estimating the contribution of this effect to differences in chaotization of field lines and particles. Because the drift is caused by the curvature of the field lines in the toroidal geometry and by the radial gradient of the magnetic field [6], we developed a cylindrical model with periodic boundary conditions which neglects the curvature. In this model, the torus is replaced by a straight cylinder. As there is no drift due to curvature and field gradient, any observed differences would be caused by other characteristics of the particle motion, such as the the cyclotron motion.

4 Results

First two figures (Fig. 1, Fig. 2) compare the dynamics of field lines and particles for two values of the stochasticity parameter L: $L = 0.0007$ and $L = 0.0025$ in the cylindrical approximation. For those values, we did not find a significant difference in chaotization, which is small for the smaller value of L and important for the larger value for both field lines and particles. This shows so far that in this approximation, which neglects the drift but not the cyclotron motion, the diffusion of the magnetic

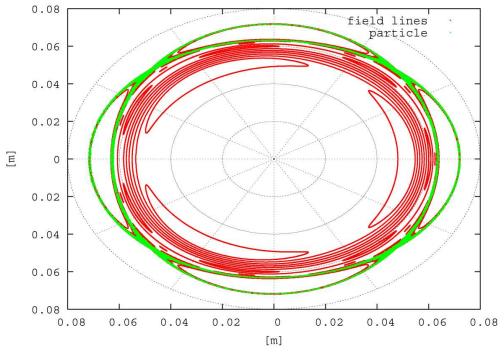

Fig. 1. Trajectory of a particle with parallel and perpendicular energies of 20 eV (green) and field lines (red) in the cylindrical approximation

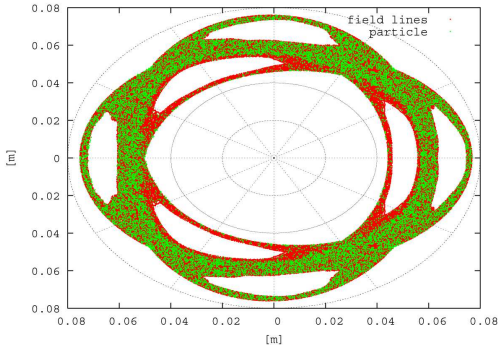

Fig. 2. Same as in Fig. 1, $L = 0.0025$

field lines is a sufficient approximation for the estimation of the diffusion of particles. The impact of the interaction of the two magnetic islands on the particle motion is here similar to the impact on field lines, at least for the parameters investigated.

The following figures (Fig. 3, Fig. 4) show the results from the toroidal model with two magnetic islands. In Fig. 3, the stochasticity of the field lines is limited

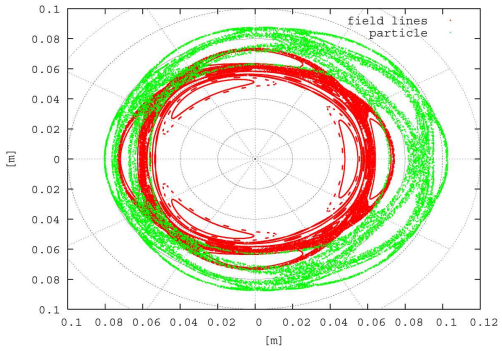

Fig. 3. Trajectory of a particle with parallel and perpendicular energies of 5 eV (green) and field lines (red) in the toroidal model, $L = 0.0014$

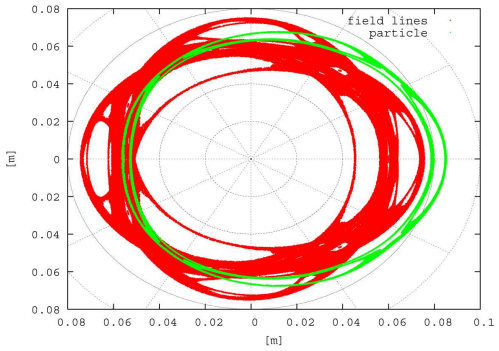

Fig. 4. Trajectories of particles with parallel energy 8 eV and perpendicular energy 16 eV (green) and field lines (red) in the toroidal model, $L = 0.002$

to the area around the separatrix, because the parameter L is not large enough for the islands to overlap. Contrary to this, the particle trajectory fills a large stochastic region which extends to the edge of torus. A similar result has been already obtained in the model with one magnetic island in [2]. In that case the

field lines are not chaotic at all due to the integrability of the Hamiltonian, while the particle trajectory shows the same behavior as shown here. This shows that the cause of this effects is not the interaction of magnetic island chains. We did not find such result in the cylindrical approximation. We therefore believe that this effect is caused by the interaction of the drift with magnetic island(s).

Fig. 4 shows the impact of increased drift velocity. If the particle energy is increased, the magnitude of the drift also increases. At a certain point, the large chaotic area disappears and the particle trajectories starting near the separatrix do not diverge significantly from it. We confirmed the results for multiple initial conditions and values of L in both the one island and two islands models. An example is shown in Fig. 4. Here the parameter L is large enough for the two islands to overlap and to create a single large stochastic area of field lines, like in Fig. 2. Contrary to this, the particle motion (shown for three initial conditions near the separatrix of the outer island chain) does not show such stochasticity.

5 Summary

We found that in a cylindrical approximation (which excludes the effect of the curvature of the toroidal magnetic field lines), the stochasticity regime of field lines and particle stochasticity agree. The expected nonlinear effect of mutual influence on the dynamics of particles, trapped in one island by the field of the second island was not recognizable. The discussion of the same dynamics, but in the tokamak field, brings very interesting phenomena. Namely, in the case of moderate vertical drift, the effect of particle stochasticity clearly dominates over the effect of stochasticity of magnetic field lines. On the contrary, for large vertical drift, we found the regime of strong stochasticity of magnetic field lines, which is accompanied by a negligible stochasticity of particles. More activity in this area to examine a broader set of parameters is necessary.

This research has been supported by the Grant agency of the Academy of Sciences of the Czech Republic, grant No. IAA100430502.

We thank the referee for constructive suggestions on the text.

References

[1] M. N. Rosenbluth, R. Z. Sagdeev, J. B. Taylor, G. M. Zaslavskii: Nucl. Fusion **6** (1966) 207.

[2] P. Cahyna, L. Krlín: Czech. J. Phys. **56** (2006) 367.

[3] J. H. Misguich, J. D. Reuss, D. Constantinescu, G. Steinbrecher, M. Vlad, F. Spineau, B. Weyssow, R. Balescu: *EUR–CEA–FC Report 1724*. Cadarache, 2002.

[4] P. Ghendrih, H. Capes, F. Nguyen, A. Samain: Contrib. Plasma Phys. **32** (1992) 179.

[5] K. Dyabilin, R. Klíma, I. Ďuran, J. Horáček, M. Hron, P. Pavlo, J. Stočkel, F. Žáček: Czech. J. Phys. **51** (2001) 1107.

[6] F. F. Chen: *Introduction to Plasma Physics*. Plenum Press, New York, 1977.

*34th EPS Conference on Plasma Phys. Warsaw, 2 - 6 July 2007 ECA Vol.**31F**, P-4.044 (2007)*

Interaction of particles with systems of magnetic islands and edge turbulence in tokamaks in fully Hamiltonian approach

P. Cahyna[1,2], L. Krlín[2], R. Pánek[2], M. Kurian[1]

[1] *Institute of Theoretical Physics, Faculty of Mathematics and Physics, Charles University, Prague 8, Czech Republic*

[2] *Institute of Plasma Physics, v.v.i., Acad. Sci. of the Czech Republic, Prague 8, Czech Republic*

Introduction

It is generally accepted that generation of transport barriers is connected with existence of a radial electric field and with the localization of the barrier in the region of rational magnetic surfaces. Moreover, stochastization of magnetic field lines around rational surfaces plays the key role behind the concepts of ergodic divertor and ELM mitigation by magnetic field perturbation [1]. Magnetic islands are generated just at the rational surfaces, thus it is interesting to investigate all features accompanying their existence.

Our contribution is based on numerical simulations from the first principles. Our goal is to compare the chaotic behavior of particles (ions) in a system of magnetic islands and to examine the differences between chaotization of magnetic field lines and particle trajectories.

Methods and results

We have taken the perturbation of equilibrium magnetic field which creates either one magnetic island chain at $q = 4$ or two island chains at $q = 4$ and $q = 5$. For the former, the field lines are regular everywhere, but particles can behave chaotically [2]. The latter case can lead to chaotic behavior of field lines because of island overlap.

The canonical equations of particle motion resulting from the full Hamiltonian with this perturbed field were integrated numerically for 20000 revolutions around the major axis and the intersections with the poloidal plane were plotted. (See [2] for details.) Other parameters are those of the CASTOR tokamak, and charge and mass of a deuterium ion, to compare with the case of carbon ions from our previous work.

We have confirmed that our former result of a single island leading to stochastization of particle trajectories (originally shown for carbon ions) is also valid for deuterium ions. To determine how this effect depends on particle parameters, we did numerous calculations with varying perpendicular and parallel energy. We then classified the Poincaré plots as strongly stochastic (where the large chaotic sea appears) or weakly stochastic (when it does not). The results are shown in Fig. 1. We see that strong stochasticity sometimes disappears apparently randomly.

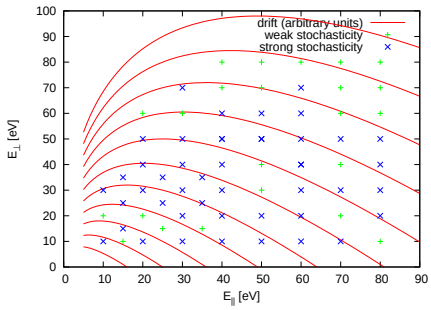

Figure 1: Initial conditions (perpendicular and parallel energy) which cause the motion of deuteron to be strongly stochastic (blue) or weakly stochastic (green), and lines of constant amplitude of drift (red).

We believe that this is caused by sensitivity to initial conditions and roundoff errors. However, in a certain region of parameters stochasticity disappears consistently. This happens for large values of drift, whose amplitude, proportional to

$$\sqrt{E_\parallel} + \frac{E_\perp}{2\sqrt{E_\parallel}}$$

is also drawn in Fig. 1. Thus the drift not only drives the stochastization, as shown in [2], but for larger values suppresses it, as well.

When a second mode of perturbation was added, we discovered a surprising effect. With only one mode of perturbation, we chose the parameters so that particle trajectory fills a large stochastic sea. With the second mode of perturbation and all other parameters identical, this stochastic sea disappeared. On the contrary, field lines are stochastic in the case of two modes and regular in the case of one mode, as expected. (Fig. 2) This disappearance of the particle chaos after the addition of a second magnetic island can probably be explained by the phase of this second ($m = 5$) island, which has an O-point at the right (low field) side, see the plot of field lines (red). The phase of the $m = 5$ island structure seen in the plot of particles (green) is opposite - the X-point is at the right side. When the $m = 5$ magnetic island is added, it probably cancels the effect of chaos because of its opposite phase (blue).

We also calculated the diffusion coefficient of the particle motion in the stochastic sea created by one magnetic island. We have computed the variance, i.e. the mean square distance from the initial point for multiple trajectories:

$$S(t) = \frac{1}{N}\sum_{i=1}^{N}(x_i(t) - x_i(0))^2$$

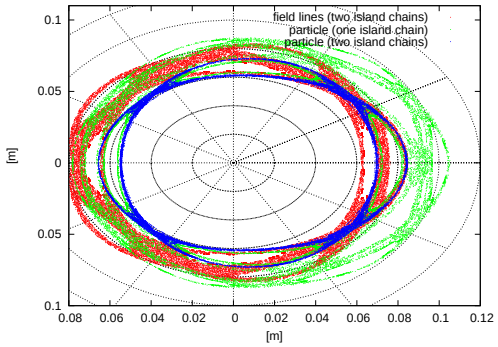

Figure 2: Intersections of field lines with the poloidal plane in the case of two island chains (red), intersections of particle gyration center for the same case (blue) and for only one island chain (green).

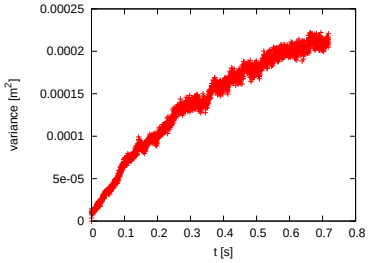

Figure 3: Time evolution of the mean square displacements from the initial position for a group of particle trajectories, for the case of chaotic motion in one magnetic island.

If the variance depends linearly on time (regular diffusion), its time derivative is the diffusion coefficient: $D = \mathrm{d}S(t)/\mathrm{d}t$. The time dependence of this variance is shown in Fig. 3. For short times, it is linear, indicating a random-walk diffusion with a diffusion coefficient with an order of magnitude of $5.10^{-4}\,\mathrm{m}^2.\mathrm{s}^{-1}$.

Further effects influence the dynamics besides magnetic islands; the most important ones being collisions and edge plasma turbulence. To estimate the latter effect, we model the action of the turbulence by means of a time-independent electrostatic potential, periodical in both the poloidal angle and the radial coordinate. We used a cylindrical configuration for simplicity, disregarding the curvature of the tokamak. Our focus was set on the diffusion of once-ionized carbon in the radial direction.

We therefore consider the potential in the form

$$V = U_0 \cos(kr) \cos\left[m\left(\theta - \frac{z}{R_0 q(r)}\right)\right].$$

The choice of k and m stems from the following physical considerations. Given that a lot of phenomena in plasma occur on the scale of millimeters, the parameter k is set to $1000\,\mathrm{m}^{-1}$. Then m is chosen to give a similar scale in the poloidal direction. The introduction of the safety factor q ensures that the potential remains constant on the unperturbed field lines. The amplitude of the potential U_0 is in range $0 - 100\,\mathrm{V}$.

Numerical simulations show that the addition of the potential has a dramatic impact on the value of radial diffusion coefficient. Firstly, the coefficient rises significantly with the magnitude of the potential. Secondly, the presence of the potential significantly increases the value of the diffusion coefficient from the unperturbed case.

$U[V]$	$D[\mathrm{m}^2.\mathrm{s}^{-1}]$
10	2.2
15	5.5
25	13.9
40	17.1

Table 1: Dependence of radial diffusion coefficient on the potential amplitude.

Conclusion

We have investigated cases where field lines are chaotic, while the particle motion is not and vice versa, and found nontrivial dependencies on particle and perturbation field parameters. We note that a similar investigation of ion motion in the perturbed field of the TEXTOR DED has been described in [3]. In the case where we computed diffusion coefficient, we have found that its value is rather low. It is an open question if in a different regime a diffusion important enough to have a tangible impact on the plasma would appear. We are currently investigating the impact of an additional electrostatic potential similar to [4]. Preliminary results show that such potential has a strong impact on diffusion of carbon ions, with diffusion coefficients exceeding $10\,\mathrm{m}^2.\mathrm{s}^{-1}$.

Acknowledgments

This work was supported by Grant Agency of the Academy of Sciences of the Czech Republic, Grant no. IAA 100430502.

References

[1] M. Bécoulet *et al.*, Nucl. Fusion **45**, 1284 (2005)

[2] P. Cahyna, L. Krlín, Czech. J. Phys. **56**, 367 (2006)

[3] S. S. Abdullaev, A. Wingen, K. H. Spatschek, Physics of Plasmas **13**, 042509 (2006)

[4] R. Pánek *et al.*, Physica Scripta **72**, 327 (2005)

6.1 Conclusions of chapter 6

Our results show that, unlike in the case of electrostatic turbulence, the gyro motion of ions does not affect their chaotic behavior in a perturbed magnetic field and the drift approximation would be appropriate. The drift causes qualitative differences in the behavior of ions, namely the case of a single perturbation mode, which is completely regular for the field lines, exhibits significant chaotic motion of ions. The quantitative significance of this effect is unclear. The diffusion coefficient calculated in the third paper is very low (cf. section 3.2). Our simulations were however done for a very idealized situation and we do not claim that the quantitative results are representative. It may be possible that for different parameters the diffusion would be considerably higher. One possibility which should be investigated in a future work is to repeat the simulations near the separatrix in an X-point geometry. This would be relevant for the ELM suppression experiments and might yield very different results from the circular cross section geometry investigated here. It should be noted that similar topic has been investigated in parallel by other groups, see e.g. [68] where a more significant diffusion coefficient is reported for a realistic situation of the TEXTOR DED (cf. section 5.1).

While our results were obtained for ions with low energies typical for the plasma edge, it is certain that stochastic diffusion plays a significant role for fast ions. Even if they had same trajectories as slower ions, the diffusion coefficient would be higher proportionally to the velocity. Moreover the drift is more important for faster particles so the effects that we observed can be expected to be enhanced. Diffusion of fast ions resulting from the NBI heating due to a magnetic island associated with a neoclassical tearing mode (cf. section 4.1) was studied in [69]. Diffusion of α particles from the fusion reactions due to magnetic perturbations was predicted in [70]. Another class of fast particles are the so-called runaway electrons (section 9.2). The magnetic perturbation coils, in addition to controlling ELMs, may find another application in controlling the runaway electrons. Our contribution to this topic is presented in chapter 9.

Chapter 7

Preparation of RMP experiments on COMPASS

As mentioned in section 5.5, RMPs are going to be an important part of the research programme on COMPASS. To prepare for this research, we have evaluated the spectra of the existing RMP coils according to the vacuum island overlap criterion. We used the same approach as many other works which evaluate the island overlap criterion [71, 72, 73, 74, 57, 58] in order to allow a comparison. In particular, we used a version of the code ERGOS by M. Bécoulet and E. Nardon which had been used for many of those studies. Our results are presented in the following two articles. The first one [5] is an initial study and presents the background in more detail, while the second one [9], in addition to having a precised model of the COMPASS coils, explains the general guidelines of construction of the RMP coils if the resonances are to be maximized. Note that the formula for island width is not the same as in e.g. [74], but a precised version derived in [71] and reproduced here in chapter 8.

ISSN 1063-780X, Plasma Physics Reports, 2008, Vol. 34, No. 9, pp. 746–749. © Pleiades Publishing, Ltd., 2008.
Published in Russian in Fizika Plazmy, 2008, Vol. 34, No. 9, pp. 808–811.

ELECTRIC FIELDS, STRUCTURES, AND RELAXATION IN PLASMAS

Resonant Magnetic Perturbations and Edge Ergodization on the COMPASS Tokamak[1]

P. Cahyna[a], M. Bécoulet[b], R. Pánek[a], V. Fuchs[a], E. Nardon[b], and L. Krlin[a]

[a] *Institute of Plasma Physics AS CR v.v.i, Association EURATOM/IPP.CR, Prague, Czech Republic*
[b] *Association EURATOM-CEA, CEA Cadarache, F-13108, St. Paul Lez Durance, France*

Received December 14, 2007; in final form, February 18, 2008

Abstract—Results of calculations of resonant magnetic perturbation spectra on the COMPASS tokamak are presented. Spectra of the perturbations are calculated from the vacuum field of the perturbation coils. Ergodization is then estimated by applying the criterion of overlap of the resulting islands and verified by field line tracing. Results show that for the chosen configuration of perturbation coils an ergodic layer appears in the pedestal region. The ability to form an ergodic layer is similar to the theoretical results for the ELM suppression experiment at DIII-D; thus, a comparable effect on ELMs can be expected.

PACS numbers: 52.55.Fa

DOI: 10.1134/S1063780X08090080

1. INTRODUCTION

The COMPASS tokamak, now being transferred to the Institute of Plasma Physics (IPP) Prague from UKAEA Culham [1], is equipped with a unique set of saddle coils for producing resonant magnetic perturbations (RMPs). It was recently discovered on the DIII-D tokamak that RMPs can lead to complete suppression of Type-I ELMs [2]. Although the COMPASS-D tokamak operated only in H-mode with type-III ELMs in UKAEA, the design of the additional heating systems (mainly NBIs) in IPP Prague is focused on obtaining type-I ELM regime. Due to incomplete understanding of the ELM physics this prediction relies mainly on empirical (scaling) laws (e.g., the available additional power is more than two times higher then L-H threshold, $T_i \approx T_e$, etc.). The availability of a flexible set of RMP coils thus opens a way to test this ELM mitigation technique. This research topic is very relevant for ITER, as ITER will need a way to mitigate large Type-I ELMs and it will be equipped with a set of perturbation coils for this purpose. The lack of a good theoretical explanation of the experimental ELM suppression results [3] makes this research even more important. Even without obtaining Type-I ELMs, experiments on COMPASS could make valuable contributions to this research, for example by investigating plasma response to the perturbation field, braking of the plasma rotation by the perturbation or the "pump-out" effect, which is believed to be responsible for ELM mitigation. Saddle coils can also be used to investigate other effects involving RMPs, such as neoclassical tearing modes (NTMs) or mode penetration. Those effects were the main subject of study in experiments involving "saddle coils" performed during the operation of COMPASS-C (circular cross section) and COMPASS-D in UKAEA Culham [4–6]. Those studies were focused on simulation of naturally occurring error fields and thus used a toroidal mode number $n = 1$ with the main poloidal mode number $m = 2$, creating a large island in the plasma core. Another experiment with COMPASS-D saddle coils that is closer to our work is described in [7]. The authors have demonstrated an effect of a perturbation resonant at the edge on ELMs and suggested RMPs as a mechanism of ELM control. This work, however, did not include estimates of edge ergodization and island overlap.

The key effect of RMPs is creation of magnetic islands and resulting ergodization of magnetic field lines. As a part of preparations for COMPASS exploitation in IPP Prague, we have thus performed calculations of spectra of RMPs caused by saddle coils, with the objective of determining the magnetic island width and the extent of ergodic regions. Unlike most of the experiments in Culham (except [7]), we were interested in edge ergodization, so we chose a coil configuration with toroidal mode number $n = 2$ and poloidal mode numbers m, which are resonant in the region near the separatrix.

2. METHODS

The calculations with the code ERGOS follow the same principle as was used for the calculations of RMP spectra for the ELM suppression experiments on DIII-D [9], JET [10, 11], and MAST and for the design work of RMP coils for ITER [12, 13]. We use the straight field line coordinate system, with coordinates (s, θ^*, ϕ). Here, ϕ is the toroidal angle; θ^* is the straight field line

[1] The text was submitted by the authors in English.

poloidal angle which satisfies $d\theta^*/d\phi = 1/q$ along a field line, where q is the safety factor; $s = \sqrt{\psi}$ is a dimensionless radial variable that labels the magnetic surfaces; and ψ denotes the poloidal flux, normalized to value 1 at the separatrix. The transformation to the straight field line coordinate system and the magnetic surface data are obtained from predictions by the MHD equilibrium code ACCOME [14] with the help of the HELENA equilibrium reconstruction code [15].

The perturbation induced by the coils is treated as a vacuum field, calculated using the Biot–Savart law from the coil positions and currents. Only the radial component (perpendicular to magnetic surfaces—thus the s component) of the perturbation field is relevant for island formation and ergodization. For the following calculations, we need the value $b^1 \equiv \delta B^1/B^3$, where B^1 is the contravariant s component of the perturbation field and B^3 is the contravariant ϕ (toroidal) component of the equilibrium field. A Fourier transform in poloidal angle θ^* and toroidal angle ϕ is applied to b^1. The modes resulting from this Fourier transform are noted as b_{mn}, where m is the poloidal and n the toroidal mode number.

The radial half-width $\delta_{m,n}$ of an island produced by the m, n mode of perturbation in terms of the dimensionless radial variable $s = \sqrt{\psi}$ is given by the formula

$$\delta_{m,n} = \sqrt{\frac{4q^2 b_{mn}}{q' m}}. \quad (1)$$

Here, $q' \equiv dq/ds$. Formula (1) is a generalized version of the formula in [16] for the case of magnetic surfaces with a noncircular cross section. We use the expression $B^3 = B_T(R)/R$ for the toroidal contravariant component of the magnetic field, where R is the radial distance from the major axis and $B_T(R) \sim 1/R$ is the toroidal field at the position given by R.

The island described by Eq. (1) appears at a radial position where $q = m/n$ (resonance condition). We note $\Delta_{m,m+1}$ the distance (in terms of the s variable) between island chains at $q = m/n$ and at $q = (m+1)/n$. Large-scale ergodization of field lines happens when successive islands overlap, causing the ergodic regions around them to merge. This happens when the Chirikov parameter $\sigma_{Chir} = (\delta_{m,n} + \delta_{m+1,n})/\Delta_{m,m+1}$ is greater than 1. It is known that in practice ergodization happens also for values of σ_{Chir} slightly less than 1, because the criterion does not take into account secondary resonances that ease merging of ergodic regions from neighboring island chains [17].

In addition to computing the Chirikov parameter, direct integration of field lines (field line tracing) was also performed. A plot of intersections of field lines with a poloidal plane after many turns around the torus (a Poincaré plot) gives a more precise picture of magnetic islands and ergodic regions.

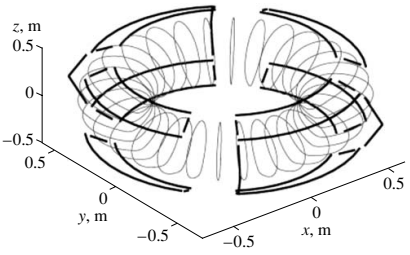

Fig. 1. Scheme of the coils used in the studied configuration, with an outline of the plasma volume.

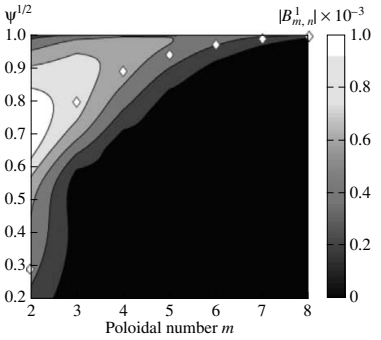

Fig. 2. Spectrum of the radial component of the perturbation field, normalized to the total field magnitude. The x-axis is the poloidal mode number m; the y-axis is the radial position $s = \sqrt{\psi}$. Diamonds show the positions of resonance surfaces with $q = m/n$.

3. RESULTS

The "saddle coils" of COMPASS are a mesh of several dozens of independently connectable coil segments on the vacuum chamber. This system is able to generate RMPs with the main toroidal number $n = 1$ or $n = 2$ due to its toroidal symmetry. To produce good edge ergodization comparable to the DIII-D experiments, we used a heuristics rule that RMP coils at the low field side are able to produce modes with the highest m to create resonances with high q. Using this rule, we chose from the numerous possible configurations the one shown in Fig. 1, which uses the outermost coil loops and has the main toroidal mode number $n = 2$. Only the $n = 2$ Fourier component of the perturbation is taken into account in the following results. The current con-

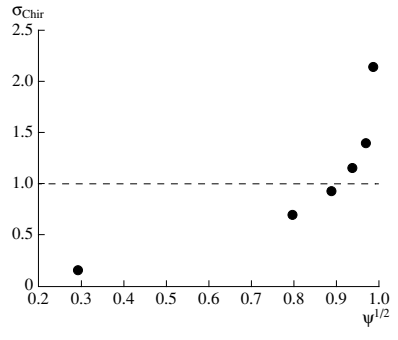

Fig. 3. Radial dependence of the dimensionless Chirikov parameter σ_{Chir}.

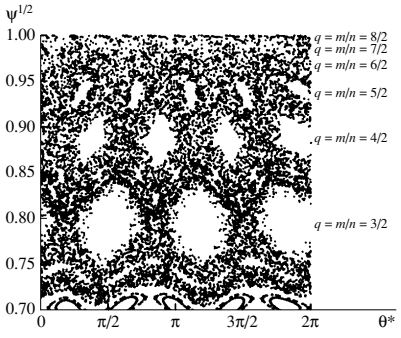

Fig. 4. Poincaré plot of field line tracing. The *x*-axis is θ*—the straight field line poloidal angle; the *y*-axis is the radial position *s*. Each dot represents an intersection of a field line with the poloidal plane.

sidered is 2 kA, which is realistically achievable with the saddle coil system. For the equilibrium a shot with NBI heating and other parameters as expected for the COMPASS exploitation in IPP Prague was chosen, using a prediction from ACCOME [18].

The resulting spectrum of the perturbation field is presented in Fig. 2. It shows the dependence of the radial perturbation component B_{mn} on the radial position and the poloidal mode number m. The rational values of the q profile $q(s) = m/n$ are shown as diamonds in the figure. The values of B_{mn} at those points determines the width of the corresponding islands.

Figure 3 shows the radial dependence of the Chirikov parameter. According to the theory, appearance of the large ergodic region is expected when $\sigma_{Chir} > 1$. This value is indicated by a horizontal dashed line. The Poincaré plot in Fig. 4 can be used to check the Chirikov criterion. The ergodic region (where the field lines densely fill a volume instead of staying on a magnetic surface) includes the island with $q = 3/2$, while the Chirikov criterion indicates that this island should not be in the ergodic region, as its $\sigma_{Chir} \approx 0.69 < 1$ (Fig. 3). The criterion thus underestimates ergodization, as explained in the previous section.

4. CONCLUSIONS

Our results show a formation of an ergodized layer in the edge region (see Fig. 4), which, according to the DIII-D [2] and JET [11] experiments, is crucial for the ELM suppression effect. If COMPASS succeeds in producing Type-I ELMs, we can expect an ELM mitigation effect of the saddle coils. Thanks to the flexibility of the saddle coil system, there is probably room for optimization of the coil configuration. More work in this area is planned.

Finally, the limitation of our calculations is that they are done by superposing the vacuum field of saddle coils with the equilibrium field. This disregards possible plasma response to the perturbation field. The impact of plasma response to the perturbation field is currently subject of intense research based on nonlinear MHD codes taking into account plasma rotation [3, 12, 13]. The main effect is expected to be the screening of RMPs by toroidal rotation due to the generation of eddy currents on resonant surfaces in response to the perturbation field [19]. However, this effect is expected to be larger in the plasma core for isolated islands and at lower resistivity (collisionality). In the edge stochastic layer where the rotation is usually smaller and resistivity larger, one could expect less screening due to the rotation. Also, the existing theory does not take into account islands overlapping (stochasticity) and large gradients of plasma parameters in the pedestal region that introduce large nonlinearity in the plasma response. At the same time, the RMPs causes plasma resonant and nonresonant braking due to the electromagnetic force [19] and neoclassical viscous force [20]. As a consequence of the plasma braking, RMPs will penetrate more. All these questions will be addressed in our future work. At the present time, however, to justify vacuum modeling results, one can rely on the experiments on DIII-D [2] and on JET [11] where the criterion of stochastization of the pedestal developed from vacuum fields was confirmed experimentally.

ACKNOWLEDGMENTS

The authors would like to thank Guido Huysmans for his help with the HELENA code. This work was supported by the Grant Agency of the Academy of Sciences of the Czech Republic, grants nos. GAAV B100430602 and GAAV A100430502.

REFERENCES

1. R. Pánek, O. Bilyková, V. Fuchs, et al., Czech. J. Phys. **56**, B125 (2006).
2. T. Evans, R. A. Moyer, J. G. Watkins, et al., J. Nucl. Mater. **337–339**, 691 (2005).
3. E. Nardon, M. Bécoulet, G. Huysmans, and O. Czarny, Phys. Plasmas **14**, 2501 (2007).
4. T. C. Hender, R. Fitzpatrick, A. W. Morris et al., Nucl. Fusion **32**, 2091 (1992).
5. R. J. Buttery, M. Volovič, C. D. Warrick, Nucl. Fusion **41**, 985 (2001).
6. A. L. Colton, R. J. Buttery, S. J. Fielding, Nucl. Fusion **39**, 551 (1999).
7. S. J. Fielding, R. J. Buttery, A. R. Field, et al., *Proceedings of the 28th EPS Conference on Controlled Fusion and Plasma Physics, Funchal*, *2001*, Paper P5.014.
8. J. Urban, V. Fuchs, R. Pánek, et al., Czech. J. Phys. **56**, B176 (2006).
9. M. Bécoulet, G. Huysmans, P. Thomas, et al., Nucl. Fusion **45**, 1284 (2005).
10. G. Agarici, M. Bécoulet, E. Nardon, et al., Fusion Eng. Design **82**, 974 (2007).
11. Y. Liang, H. R. Koslowski, P. R. Thomas, et al., Phys. Rev. Lett. **98**, 265004 (2007).
12. E. Nardon, M. Bécoulet, G. Huysmans, et al., J. Nucl. Mater. **363–365**, 1071 (2007).
13. M. Bécoulet, E. Nardon, G. Huysmans, et al., in *Proceedings of the 21st IAEA Fusion Energy Conference, Chengdu, 2006*, Paper IT/P1-29.
14. K. Tani, M. Azumi, and R. S. Devoto, J. Comput. Phys. **39**, 332 (1992).
15. G. Huysmans, J. Goedbloed, and W. Kerner, in *Proceedings of the CP90 Europhysics Conference on Computational Physics, Amsterdam*, 1990, p. 371.
16. Ph. Ghendrih, A. Grosman, H. Capes, Plasma Phys. Controlled Fusion **38**, 1653 (1996).
17. A. J. Lichtenberg and M. A. Lieberman, *Regular and Stochastic Motion* (Springer-Verlag, New York, 1983; Mir, Moscow, 1984).
18. O. Bilyková, V. Fuchs, R. Pánek, et al., Czech. J. Phys. **56**, B24 (2006).
19. R. Fitzpatrick, Phys. Plasmas **5**, 3325 (1998).
20. E. Lazzaro, R. J. Buttery, T. C. Hender, et al., Phys. Plasmas **9**, 3906 (2002).

The optimization of resonant magnetic perturbation spectra for the COMPASS tokamak

2009 Nucl. Fusion 49 055024

(http://iopscience.iop.org/0029-5515/49/5/055024)

IOP Publishing and International Atomic Energy Agency Nuclear Fusion
Nucl. Fusion **49** (2009) 055024 (7pp) doi:10.1088/0029-5515/49/5/055024

The optimization of resonant magnetic perturbation spectra for the COMPASS tokamak

P. Cahyna[1], R. Pánek[1], V. Fuchs[1], L. Krlín[1], M. Bécoulet[2], G. Huysmans[2] and E. Nardon[3]

[1] Institute of Plasma Physics AS CR v.v.i., Association EURATOM/IPP.CR, Prague, Czech Republic
[2] Association Euratom-CEA, IRFM, Cadarache, 13108, St-Paul-lez-Durance, France
[3] Euratom/UKAEA Fusion Association, Culham Science Centre, Abingdon, OX143DB, UK

E-mail: cahyna@ipp.cas.cz

Received 30 December 2008, accepted for publication 31 March 2009
Published 28 April 2009
Online at stacks.iop.org/NF/49/055024

Abstract
The COMPASS tokamak, recently transferred from UKAEA Culham to IPP Prague, is equipped with a set of saddle coils for producing controlled resonant magnetic perturbations (RMPs). In the future experimental programme of COMPASS we plan to focus on studies of RMPs, especially in view of their application as an ELM control mechanism and their considered use in ITER. In the present contribution we describe the preparatory calculations for the planned experiments. We computed the spectra of perturbations for several different equilibria predicted by MHD simulations and determined the positions and sizes of the resulting islands. It is shown how the saddle coils of COMPASS can be adapted to our equilibria to obtain good island overlap at the edge, which is believed to be a key component in the ELM mitigation effect. The techniques used for adapting the coils to achieve this result are described. Those are fairly general and could be used in the design of RMP coils on other machines.

PACS numbers: 52.55.Fa

(Some figures in this article are in colour only in the electronic version)

1. Introduction

In past years there has been a growing interest in the physics of resonant magnetic perturbations (RMPs) applied externally to a tokamak plasma. The main motivation is that they are a promising tool to control type I edge localized modes (ELMs)—an important issue for ITER. The ability of mitigating ELMs has been discovered on DIII-D [1] and subsequently confirmed by recent experiments on JET [2]. Coils to induce RMPs for ELM mitigation are proposed in the ITER design [3]. There are however still many open questions concerning the mechanism itself and related issues, and the theory of the mitigation effect is far from being complete.

The COMPASS tokamak, which is now being reinstalled in IPP Prague [4], is a device suitable for the research of magnetic perturbations. It is a tokamak with single-null divertor plasma and geometry similar to JET or ITER at a much smaller scale with the major radius of 0.56 m. Its unique feature is a rich set of 'saddle coils' to produce magnetic perturbations. Our plan is to use them to investigate the effects associated with the ELM mitigation technique. Examples of effects which should be studied are: the density pump-out or the impact of perturbations on the plasma rotation by both resonant [5, 6] and non-resonant braking [7, 8], which is especially important for ITER. If we succeed in obtaining type I ELMs on the reinstalled COMPASS thanks to the new NBI heating system, it will be also possible to study the ELM mitigation effect directly. Given that COMPASS has a similar geometry to DIII-D or JET but much smaller dimensions, experiments with RMPs on COMPASS can extend the present experience to a wider range of parameters and thus contribute to the understanding of the fundamental mechanisms of the RMP technique.

In this paper we present calculations of the perturbation field that we have done in preparation for the experiments with 'saddle coils'. We start with the analysis of spectra of the vacuum field. In this simplified model, the plasma response to the perturbation is not taken into account, the field is modelled as the plasma equilibrium field with the vacuum field from the saddle coils added. We use this approach to determine the optimal coil configuration for producing sufficient island overlap at the edge, which has been suggested to be the key for ELM mitigation [9, 10]. Knowledge of the required

configuration will be important for adjusting the coils before the COMPASS operation starts.

2. Vacuum field calculations with the code ERGOS

Nonaxisymmetric perturbations of the tokamak magnetic field are able to produce magnetic islands. One mechanism through which the perturbation field may influence the plasma is the destruction of magnetic surfaces and stochastization of the field lines. This effect is linked to the magnetic islands, because it arises when neighbouring island chains become large enough to overlap each other. The overlapping of magnetic islands at the plasma edge was proposed as the criterion for the ELM suppression effect, according to the observed correlations [9, 10]. We are therefore using the same criterion for evaluating the suitability of COMPASS for the research of the ELM suppression effect and for choosing among the configurations of the perturbation coils the one which will be optimal for this research.

In accordance with many previous works [9–12], we use the vacuum field of the perturbation coils superimposed with the equilibrium field of the plasma in the absence of the perturbation. This simple approach will be referred to as the 'vacuum approximation'. It neglects possible modification of the perturbation field by the presence of the plasma. We use this approach because of its proven ability to characterize the ELM suppression effect [9, 10], but we are aware that it might not be an accurate model of the actual magnetic field in the plasma.

The width of the magnetic islands is calculated according to the procedure described in [11, 13] in a magnetic coordinate system [14] (s, θ^*, φ), where s is a dimensionless flux surface label defined as the square root of the normalized poloidal flux ψ: $s = \sqrt{\psi}$. The poloidal and toroidal angular coordinates θ^* and φ represent a field line as a line of a constant slope: $\mathrm{d}\theta^*/\mathrm{d}\varphi = 1/q(s)$ along a field line, where $q(s)$ is the safety factor on a surface given by s. In addition, the coordinate φ is taken equal to the geometric toroidal angle, leading to the PEST coordinate system [14, 15]. The magnetic islands are produced by the contravariant radial component of the perturbation field $B^1 = \delta\vec{B} \cdot \nabla s$, $\delta\vec{B}$ being the perturbation field. Islands appear at the rational values of the safety factor q and their size is determined by the Fourier component $\tilde{b}^1_{(m,n)}$ of B^1 normalized to the toroidal contravariant component B^3 of the equilibrium field: $B^3 = \vec{B} \cdot \nabla\varphi = B_\mathrm{T}/R$, where R is the distance from the major axis. $\tilde{b}^1_{(m,n)}$ is thus defined by the equation

$$b^1(s, \theta^*, \varphi) \equiv B^1/B^3 = \sum_{m,n=-\infty}^{\infty} \tilde{b}^1_{(m,n)}(s) \exp\left[\mathrm{i}(m\theta^* + n\varphi)\right] \tag{1}$$

and can be calculated using the formula

$$\tilde{b}^1_{(m,n)}(s) = \frac{1}{2\pi} \int_0^{2\pi} \exp(-\mathrm{i}m\theta^*) \tilde{b}^1_n(s, \theta^*)\, \mathrm{d}\theta^*, \tag{2}$$

where $\tilde{b}^1_n(s, \theta^*)$ is the n toroidal Fourier component of $b^1(s, \theta, \varphi)$:

$$\tilde{b}^1_n(s, \theta^*) = \frac{1}{2\pi} \int_0^{2\pi} \exp(-\mathrm{i}n\varphi) b^1(s, \theta^*, \varphi)\, \mathrm{d}\varphi. \tag{3}$$

The resulting island is created on a resonant surface with $q = m/n$ and its half-width $\delta_{m,n}$ is given by the formula [16]

$$\delta_{m,n} = \sqrt{\frac{8q^2 \tilde{b}^1_{(m,n)}}{q'm}}, \tag{4}$$

where $q' \equiv \mathrm{d}q/\mathrm{d}s$. Those formulae are a variant of the formulae given in [11], improved to include the radial variation of the toroidal equilibrium field (B^3 in (1)) instead of using the value at the magnetic axis. This gives a more accurate result [17].

To quantify the overlap of magnetic islands on neighbouring rational surfaces with the same value of n we use the Chirikov parameter σ_Chir defined as $\sigma_\mathrm{Chir} \equiv (\delta_{m,n} + \delta_{m+1,n})/\Delta_{m,n}$ where $\delta_{m,n}$ is defined in (4) and $\Delta_{m,n}$ is the radial distance (in terms of the coordinate s) between the surfaces with $q = m/n$ and $q = (m+1)/n$. The criterion for island overlap is $\sigma_\mathrm{Chir} > 1$. (However, transition to stochasticity occurs for smaller values of σ_Chir because of secondary island chains which appear between the primary ones [18]. Islands created by perturbation modes with another toroidal number n will also facilitate the transition to stochasticity by 'filling in gaps' between the islands with one value of n [9].) The transition to stochasticity can be verified by tracing the field lines and displaying the Poincaré plot of their intersections with a chosen poloidal plane. Such a plot will clearly show the magnetic islands, the stochastic areas and remaining magnetic surfaces between them.

For actual calculations we used the code ERGOS [11], which had been previously used for the cases of DIII-D [12], JET and MAST [10] and proposed designs of the ITER RMP coils [11, 13], for example. The input to the code is the configuration of the coils (given by their geometry and current distributions) and the magnetic equilibrium. The equilibrium is needed for calculating the contravariant component B^1, for transforming to the magnetic coordinate system (s, θ^*, φ), and for knowing the profile of q and its derivative q', which are in turn needed to know the positions and sizes of the magnetic islands—equation (4). The perturbation spectra thus depend on the equilibrium.

The output of the code is the profile of σ_Chir, radial dependence of the perturbation spectrum (dependence of $\tilde{b}^1_{(m,n)}$ on s) and the Poincaré plot resulting from field line tracing in the perturbed magnetic field.

3. Techniques for spectrum optimization

Especially in the case of a new coil design or of choosing a configuration of a very flexible coil system (as it is the case of COMPASS) it is useful to have general rules which allow one to heuristically choose a good configuration. For the application we are interested in an optimal configuration maximizes the overlap of islands at the plasma edge for a given coil current (governed by technical and financial constraints).

As the island sizes are given by the value of $\tilde{b}^1_{(m,n)}$ at the radial position s where $q(s) = m/n$, they will be maximized when the maxima of $\tilde{b}^1_{(m,n)}(s)$ in the (m, s) space are located at the points where the condition $q(s) = m/n$ holds. This can be checked graphically by plotting $\tilde{b}^1_{(m,n)}(s)$ as a function of (m, s) and checking the overlap of its maxima with the safety

factor profile given by $q(s) = m/n$. This gives an indication of whether the maximal value of $\tilde{b}^1_{(m,n)}(s)$ needs to be moved to higher or lower values of m, which can be done by making the coils narrower or larger, respectively. (In this procedure n is kept constant, it is assumed that there is one dominant toroidal mode, corresponding to the toroidal symmetry of the coils.)

The resonances at the edge, where the q is high, occur for large values of m. To obtain a $\tilde{b}^1_{(m,n)}$ spectrum with a maximum at high values of m the corresponding b^1 as a function of θ^* must be narrow in the θ^* space. To achieve this it is preferable to place the coils at a position where θ^* changes slowly as a function of the geometric poloidal angle, i.e. with a steep pitch angle of the field lines. Areas near the X-points should be avoided because there the pitch angle of the field lines is low due to the small poloidal field. In addition the low-field side (LFS) is preferable to the high-field side (HFS), because the field lines are steeper at the LFS as a consequence of the toroidal geometry. Moreover the Shafranov shift of magnetic surfaces outwards causes ∇s to be maximal at the LFS which maximizes the value of b^1, being given by the contravariant radial component: $b^1 = B^1/B^3 = (\delta\boldsymbol{B}\cdot\nabla s)/(\boldsymbol{B}\cdot\nabla\varphi)$. At the same time the denominator B^3 is minimized because of the low toroidal magnetic field. All those geometric effects make the LFS the optimal place for placing the perturbation coils [16].

To estimate what are the best coil positions for a given equilibrium it is useful to display possible coil positions in a poloidal cross-section together with the mesh of (s, θ^*) magnetic coordinates. The coils produce a radial perturbation which is directed either inwards or outwards. If the coils are symmetric with respect to the midplane, there may be an 'even' configuration (where an upper coil has the same field orientation as the symmetric lower coil) or an 'odd' one (where upper and lower coils have opposite fields). To maximize the Fourier component $\tilde{b}^1_{(m,n)}(s)$ on a resonant surface with $q(s) = m/n$ the maxima and minima of the radial perturbation's main toroidal mode $\tilde{b}^1_n(s, \theta^*)$ as a function of θ^* shall correspond to maxima and minima of the function $\cos(m\theta^*)$ for an even configuration and to $\sin(m\theta^*)$ for an odd configuration[4]. This follows from the formula (2) for $\tilde{b}^1_{(m,n)}$. According to (2) the even (resp. odd) function $\tilde{b}^1_n(\theta^*)$ of a given norm which maximizes $\tilde{b}^1_{(m,n)}$ is $\cos(m\theta^*)$ (resp. $\sin(m\theta^*)$), thus we are looking for a realistic perturbation $\tilde{b}^1_n(\theta^*)$ which is close to one of those optimal ones, so it has corresponding maxima, minima and zero points. For that we display the sign of $\cos(m\theta^*)$ or $\sin(m\theta^*)$ on resonant surfaces and place the coil loops so that one direction of the field is close to areas with positive sign and other direction to areas of negative sign. The toroidal coil segments which delimit the loops in the poloidal direction shall be placed against zeros of $\sin(m\theta^*)$ or $\cos(m\theta^*)$, because at the vicinity of those segments the radial field component changes direction and thus has a zero.

Figures 1 and 2 illustrate this procedure for an example equilibrium and coil configuration (the SNT-02 equilibrium, see section 5). The radial perturbation $\tilde{b}^1_{(m,n)}$ for the best coil configuration is compared against the ideal perturbation of the form $\sin(m\theta^*)$ on a resonant surface with $q = 6/2$ $(m = 6, n = 2)$. In figure 2 $\tilde{b}^1_{(m,n)}$ is shown on this surface in a poloidal cross-section of the equilibrium. Its values are represented as displacements in the direction of the θ^* coordinate lines from the surface. In addition the positions where $\sin(m\theta^*)$ is positive or negative are displayed. To generate this perturbation the toroidal coil segments were placed as close as possible to the zeros of $\sin(m\theta^*)$, those positions are also shown in figure 2.

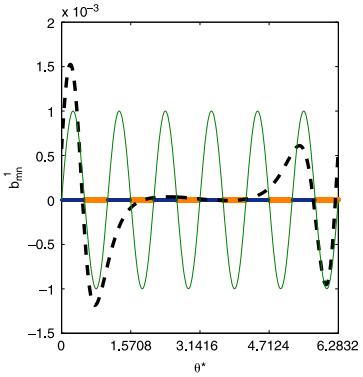

Figure 1. Example radial perturbation $\tilde{b}^1_n(\theta^*)$ (generated by the optimal coil configuration for the SNT-02 equilibrium on COMPASS) on the $m = 6$, $n = 2$ resonant surface—dashed line, with $10^{-3}\sin(m\theta^*)$ shown for comparison—full line (green online). The sign of $\sin(m\theta^*)$ is shown as narrow dark (blue online) and thick light (orange online) bands on the x-axis for positive and negative signs, respectively—this scheme is used in the following figures.

The procedure described above optimizes the perturbation on a selected resonant surface. In practice it can be observed that at the LFS the zeros of $\sin(m\theta^*)$ or $\cos(m\theta^*)$ are well aligned between different magnetic surfaces. This means that for coils at the LFS we can optimize the spectrum at a range of surfaces simultaneously, which is advantageous to obtain a good overlap of islands.

4. COMPASS RMP coils

Each of the four quadrants of the vacuum vessel of COMPASS is covered by a set of toroidal and poloidal coil segments[5] to produce RMPs. Because of the four-fold symmetry the main toroidal mode number n can be 1 or 2. (We focus on the $n = 2$ toroidal mode as the $n = 1$ one is more problematic because of locked modes [2].) There are four outer toroidal segments at each of the two opposite quadrants and five at each of the remaining two quadrants. The symmetry is only approximate because the poloidal positions of the four outer toroidal segments are different in each quadrant and there are many irregularities as the coils need to avoid the ports. The outermost toroidal segment at the outboard midplane is also present only in two opposite quadrants and is missing

[4] The coordinate θ^* is chosen to be zero at the outboard midplane, so $\cos(m\theta^*)$ and $\sin(m\theta^*)$ are even and odd functions, respectively, with respect to the midplane.

[5] They are sometimes called 'saddle coils', not to be confused with 'saddle loops' which are diagnostic coils to measure the radial magnetic flux.

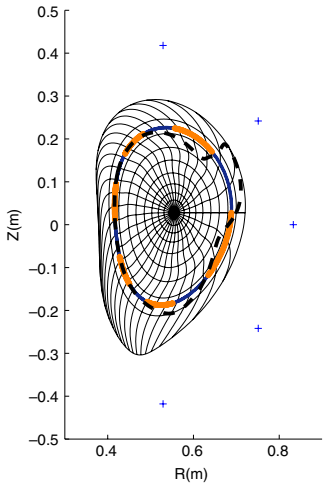

Figure 2. The graph of $\tilde{b}^1_s(\theta^*)$ (black dashed line) from figure 1 mapped to the corresponding mesh of the equilibrium magnetic coordinates, as explained in the text. The sign of $\sin(m\theta^*)$ is shown as narrow dark (blue online) and thick light (orange online) bands on the resonant surface for positive and negative signs, respectively. The positions of the toroidal coil segments that generated the perturbation are shown as crosses (blue online).

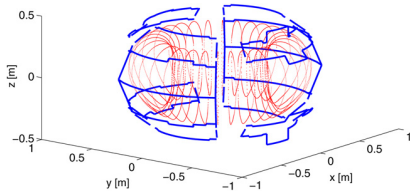

Figure 3. The outboard coils used in the studied configurations (full lines, blue online) with an outline of the plasma volume (dotted lines, red online).

from the other two quadrants because of large midplane ports (see figure 3)—that is why those two quadrants have only four outer toroidal segments instead of five. This means that a configuration avoiding the outermost segments in the two quadrants where they are present will have a better toroidal symmetry and a dominant $n = 2$ toroidal mode, while for a configuration using them the imperfect symmetry will lead to larger sidebands in addition to the main $n = 2$ toroidal mode. All the coil segments can be connected independently. In principle there is an enormous number of possibilities for the configurations distinguished by the current directions in the segments. In addition the four outer toroidal segments in each quadrant can be moved in the poloidal direction, which adds another degree of freedom in the configuration. But only a small percentage of the configurations are practical. We are looking for configurations that have a well defined toroidal mode number and use the outer (LFS) coils for the reasons given in section 3. Moreover there is a constraint that at every point where several coils meet the sum of incoming and outgoing currents from the power supplies should be zero. The bars which connect the coils to the linkboards are for all such points close to each other so if the total current in such a bundle of bars is zero, the total force from the toroidal field will be also zero, minimizing the mechanical stress [19]. It is also ensured that the bars will not create stray fields, thus we don't need to include them in the coil model. This constraint means that the coils can be effectively thought of as a sum of closed loops, with some segments shared between two loops (their current will be two times higher compared with the others).

All the above-mentioned requirements determine what coils should be used (see figure 3) and constrain the directions of their currents. The positions of the movable coil segments shall be tuned to the magnetic equilibrium using the methods described in section 3. So far we have not tried to optimize the distribution of the currents but we have always chosen identical currents in all the segments except those which are shared between two loops. The free parameters are thus the positions of the movable segments, the loops used and the orientation of the current in each loop. The current orientations determine if the configuration is 'odd' or 'even'.

5. Results for selected equilibria

To demonstrate the ability of producing overlapping islands at the edge we used several equilibria that we believe to be representative for the future operation of COMPASS. Those equilibria are predicted by the MHD code ACCOME [20], taking into account the planned neutral beam injection and lower hybrid current drive, which together produce a substantial fraction of the current [21]. The equilibria are:

- SNT-02—a high field, high current ($B = 2.1$ T, $I = 250$ kA) equilibrium with a high triangularity ($\delta = 0.5$–0.7)
- SND-02—a high field, high current equilibrium with a low triangularity ($\delta = 0.3$–0.4)
- SND-01—a low field, low current ($B = 1.2$ T, $I = 175$ kA) equilibrium with a low triangularity ($\delta = 0.3$–0.4).

The code HELENA [22] is used to produce the mapping to the magnetic coordinate system used by ERGOS.

Figure 4 shows the magnetic coordinate system of the SNT-02 equilibrium. An odd parity configuration needs to be used because it has narrower coil loops (there are two narrow coil loops above and below the midplane separated by the midplane toroidal segment, instead of one larger loop centred on the midplane in an even parity configuration), thus is able to produce the high m poloidal modes which are needed for resonances with the safety factor profile in this equilibrium. The sign of $\sin(m\theta^*)$ is shown in colour for several resonant surfaces. Also shown are the ranges of positions of the outer movable toroidal coil segments. It can be seen that to match the equilibrium the outermost possible positions shall be used. They still do not perfectly match the positions of zeros

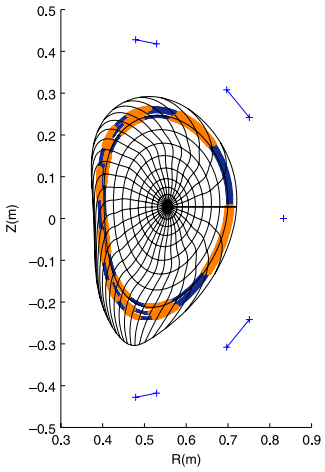

Figure 4. Magnetic coordinates for the SNT-02 case, with sgn sin($m\theta^*$) shown as in figures 1 and 2 on three resonant surfaces with $m = 7, 8, 9$. Ranges of possible positions of the four movable coil segments are shown as lines and the position of the outermost (midplane) segment as a cross outside the plasma volume (blue online).

of sin($m\theta^*$). The radial dependence of spectrum shown in figure 5 confirms these conclusions. The maxima of the spectra occur at smaller values of m than those corresponding to the q profile, which means that it would be beneficial to move the coils even more outwards to produce a narrower perturbation, if there were such a possibility. The maxima of the spectrum form a curve in the (m, s) space which is parallel to the q profile, so the same conclusion holds for all radial positions at the edge. (This confirms the conclusion about simultaneous optimizing for a range of radial positions and is a fairly generic feature of the edge perturbation spectra.) Figure 6 shows the resulting profile of the Chirikov parameter. We have shown that the available coil positions are not ideal, but despite this there is a good island overlap in the edge region for a current in the coils of 2 kA. (The coil segments that are shared between two adjacent loops will have twice as much current, i.e. 4 kA. The coils are designed for a maximum current of 5 kA.). This result can be compared with the criterion suggested in [9] on the basis of the DIII-D experiments: the region with $\sigma_{\mathrm{Chir}} > 1$ should extend to $\psi = 0.83$, or $\sqrt{\psi} \doteq 0.91$. According to figure 6 this criterion is satisfied. Figure 7 shows the resulting Poincaré plot for a current of 2 kA. The SND-02 equilibrium has similar properties as the SNT-02 one with respect to the conclusions about optimal positioning of the coils and the resulting spectrum, which is thus not shown for brevity. This is related to a similar value of q_{95} between these two. The profile of the Chirikov parameter is shown in figure 6.

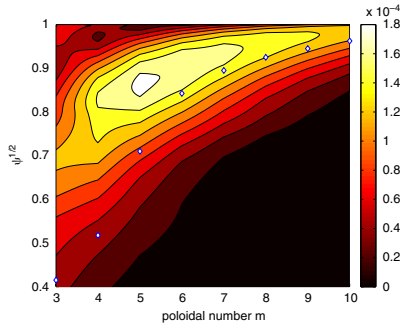

Figure 5. Spectrum of $\tilde{b}^1_{(m,n)}$ and the positions of resonances (diamonds) for the SNT-02 case.

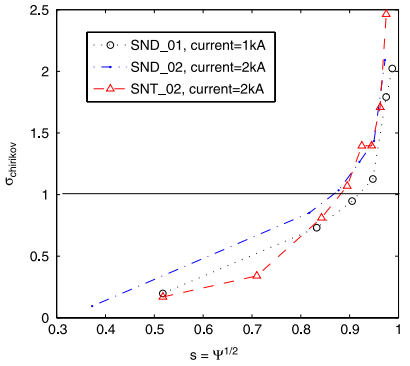

Figure 6. Radial dependence of the Chirikov parameter for the equilibria considered.

The SND-01 equilibrium has a substantially lower q_{95} than the preceding two. Zeros of sin($m\theta^*$) are much more distant poloidally which could be accommodated for by moving the coils outwards to produce a wider perturbation. It is more practical, however, to use an even parity configuration which keeps the coils at the same place but uses a large loop in the midplane for a perturbation wider in the poloidal direction. The reason is technical: while the coils are movable in principle, it is preferable to avoid readjusting them between shots because of access difficulties. It will be much easier to rewire the coils for different currents, as this is done on linkboards designed for easy reconfiguration. By avoiding the midplane coil segments we also obtain better symmetry and a stronger main $n = 2$ toroidal component. Because of the even parity the positions of the coils should be compared against zeros of cos($m\theta^*$). The sign of cos($m\theta^*$) on several resonant surfaces is shown together with the coordinate mesh on figure 8. Again the coil positions are not ideally matched to the equilibrium, but the

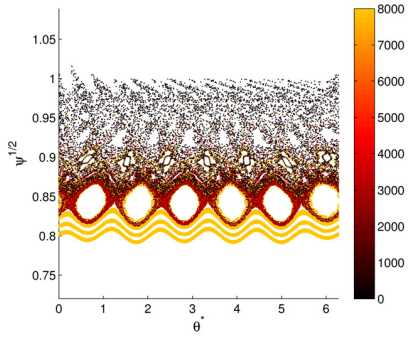

Figure 7. Poincaré plot for the SNT-02 case, coil current 2 kA. The colour of the dots represent the number of toroidal turns that the field lines need to escape beyond the separatrix.

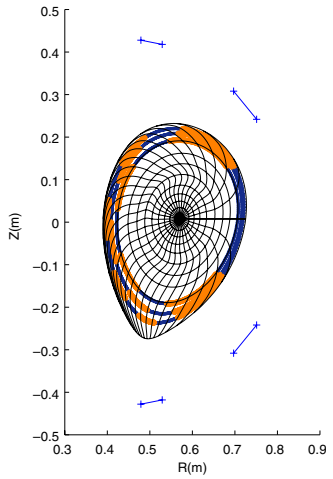

Figure 8. Magnetic coordinates for the SND-01 case, with $\operatorname{sgn}\cos(m\theta^*)$ and coil positions shown as in figure 4 for $m = 4, 5, 6$.

resulting island overlap (figure 6) is very good even at a current of 1 kA.

Our results have been so far confined to examining the coil field without taking the plasma response into account—the vacuum approximation. A complete description of the edge structures created by the external perturbation shall include the modification of the coil field by the plasma response. We may expect that the plasma rotation will screen the perturbation in the core but the pedestal region shall remain ergodized because of slower rotation and lower temperatures, as shown by analytic estimates for TEXTOR in [23] and MHD modelling for DIII-D and ITER parameters in [24]. Similar modelling shall be done for COMPASS when the relevant plasma profiles (especially toroidal rotation and temperature) are better known, either from simulations or from the upcoming experiments. As noted in [24], the situation for an H-mode plasma is further complicated by the diamagnetic effects which may be an important contribution to the screening due to steep pedestal gradients.

6. Conclusions

We have demonstrated that for a wide variety of magnetic equilibria the perturbation coils on the COMPASS tokamak are able to produce overlapping magnetic islands at the plasma edge. We are thus confident in the relevance of planned experiments with the magnetic perturbations to the research of interactions of resonant magnetic perturbations with plasma, especially the mechanism of ELM suppression. We developed methods for optimizing the coil geometry and we have used them to specify the required positions of the perturbation coils. The result will be used to configure the coils before COMPASS operation starts. It is encouraging that so far we have not found necessary to adjust the coil positions differently for different plasma parameters, which will facilitate the operation a lot.

Acknowledgments

The authors are grateful to Tom Todd for valuable discussions and to Josef Havlíček for help with creating the coil model. This work was supported by the European Communities under the contracts of Association between EURATOM and IPP.CR, CEA and UKAEA. The views and opinions expressed herein do not necessarily reflect those of the European Commission.

References

[1] Evans T.E. *et al* 2008 RMP ELM suppression in DIII-D plasmas with ITER similar shapes and collisionalities *Nucl. Fusion* **48** 024002
[2] Liang Y. *et al* 2007 Active control of Type-I edge-localized modes with $n = 1$ perturbation fields in the JET tokamak *Phys. Rev. Lett.* **98** 265004
[3] Thomas P.R. 2008 ELM physics and ELM mitigation in ITER *Proc. 22nd Int. Conf. on Fusion Energy (Geneva, Switzerland, 2008)* (Vienna, IAEA) CD-ROM file IT/1-5 and http://www-naweb.iaea.org/napc/physics/FEC/FEC2008/html/index.htm
[4] Panek R. *et al* 2006 Reinstallation of the COMPASS-D tokamak in IPP ASCR *Czech. J. Phys.* **56** B125–37
[5] Fitzpatrick R. 1998 Bifurcated states of a rotating tokamak plasma in the presence of a static error-field *Phys. Plasmas* **5** 3325–41
[6] Kikuchi Y. *et al* 2006 Forced magnetic reconnection and field penetration of an externally applied rotating helical magnetic field in the TEXTOR tokamak *Phys. Rev. Lett.* **97** 085003
[7] Shaing K.C. 2003 Magnetohydrodynamic-activity-induced toroidal momentum dissipation in collisionless regimes in tokamaks *Phys. Plasmas* **10** 1443–8
[8] Lazzaro E. *et al* 2002 Error field locked modes thresholds in rotating plasmas, anomalous braking and spin-up *Phys. Plasmas* **9** 3906–18

[9] Fenstermacher M.E. *et al* 2008 Effect of island overlap on edge localized mode suppression by resonant magnetic perturbations in DIII-D *Phys. Plasmas* **15** 056122
[10] Nardon E., Kirk A., Ben Ayed N., Bécoulet M., Cahyna P., Evans T., Huysmans G., Koslowski H.R., Liang Y., Saarelma S., Thomas P.R. and JET-EFDA Contributors 2009 ELM control by resonant magnetic perturbations on JET and MAST *J. Nucl. Mater.* doi:10.1016/j.jnucmat.2009.01.205.
[11] Bécoulet M. *et al* 2008 Numerical study of the resonant magnetic perturbations for Type I edge localized modes control in ITER *Nucl. Fusion* **48** 024003
[12] Bécoulet M. *et al* 2005 Edge localized modes control by stochastic magnetic fields *Nucl. Fusion* **45** 1284–92
[13] Nardon E. *et al* 2007 Edge localized modes control by resonant magnetic perturbations *J. Nucl. Mater.* **363–365** 1071–5
[14] Park J.K., Boozer A.H. and Menard J.E. 2008 Spectral asymmetry due to magnetic coordinates *Phys. Plasmas* **15** 064501
[15] Grimm R.C., Dewar R.L. and Manickam J. 1983 Ideal MHD stability calculations in axisymmetric toroidal coordinate systems *J. Comput. Phys.* **49** 94–117
[16] Nardon E. 2007 Edge localized modes control by resonant magnetic perturbations *PhD Thesis* Ecole Polytechnique http://www.imprimerie.polytechnique.fr/Theses/Files/Nardon.pdf
[17] Kaleck A. 1999 On island formation in a locally perturbed tokamak equilibrium *Contrib. Plasma Phys.* **39** 367–79
[18] Lichtenberg A.J. and Lieberman M.A. 1983 *Regular and Stochastic Motion* (*Applied Mathematical Sciences* vol 38) (New York: Springer)
[19] Todd T. 2008 personal communication
[20] Tani K., Azumi M. and Devoto R.S. 1992 Numerical analysis of 2D MHD equilibrium with non-inductive plasma current in tokamaks *J. Comput. Phys.* **98** 332–41
[21] Fuchs V. *et al* 2008 Heating and current drive modeling for the IPP Prague COMPASS tokamak *Proc. 35th EPS Conf. on Plasma Physics (Hersonissos, Greece)* vol 32F (ECA) P–2.098 http://epsppd.epfl.ch/Hersonissos/pdf/P2_098.pdf
[22] Huysmans G., Goedbloed J. and Kerner W. 1991 *Proc. CP90 Europhys. Conf. Computational Physics (Amsterdam, The Netherlands, 1990)* p 371
[23] Lehnen M. *et al* 2008 The DED at TEXTOR Transport and topological properties of a helical divertor *Plasma Fusion Res.* **3** S1039
[24] Bécoulet M. *et al* 2009 Physics of penetration of resonant magnetic perturbations used for Type I edge localized modes suppression in tokamaks *Nucl. Fusion* submitted

7.1 Conclusions of chapter 7

We have seen that COMPASS can present an interesting comparison to other tokamaks with the RMP capability. The possibility of switching the perturbations between even and odd parity will be important, as the dependence of the effects on the perturbation alignment with the field lines is one of the unsolved problems[1]. We plan to further increase flexibility by adding new coils with eight-fold symmetry in order to be able to produce $n = 4$ perturbations and investigate the importance of the toroidal mode number.

Besides coil enhancements, our current work on COMPASS is focused on planning of the experiments and specification of the requirements on diagnostics. COMPASS will be equipped with many diagnostics for the edge layer, for example Thomson scattering system, reciprocating probes, visible cameras and edge rotation measurements. One of diagnostics available for the first experiments are the divertor Langmuir probes. They can provide a radial profile on the divertor and observe the splitting of strike points which shall occur when RMPs are applied (cf. section 5.2). As we are interested in the problem of RMP screening by the plasma (cf. section 5.4), we should know if strike-point splitting can provide us with some information about the screening. This is the topic of the next chapter.

[1] Of course, if the creation of a stochastic layer in the vacuum approximation is the key element, the alignment shall not play a role if the resonant components are the same. This is however just a hypothesis to be verified.

Chapter 8

Divertor footprints and RMP screening

In the following papers we explore the connection between resonant magnetic perturbation and the divertor strike point splitting in spiralling patterns, called footprints. The first paper [14] deals with the vacuum approximation. It has been known that the resonant perturbation modes and the footprints can be expressed using the same function [45, 75]. We present a rigorous Melnikov function formalism and we prove that under additional assumptions on the location of the coils a formula relating the resonant perturbation modes to the footprints can be derived. In this way it is proven that magnetic islands and footprints are correlated. The question if the correlation still holds in the case when the perturbations are screened by the plasma. This is the topic of the second paper [15], which was submitted to the proceedings of the international conference on plasma surface interactions (to be published in Journal of Nuclear Materials).

Resonant magnetic perturbations and divertor footprints in poloidally diverted tokamaks

Pavel Cahyna[1,*] and Eric Nardon[2]

[1]*Institute of Plasma Physics AS CR v.v.i., Association EURATOM/IPP.CR, Prague, Czech Republic*
[2]*Association EURATOM-CEA, CEA/DSM/IRFM, CEA Cadarache, 13108 St-Paul-lez-Durance, France*

General formula describing both the divertor strike point splitting and width of magnetic islands created by resonant magnetic perturbations (RMPs) in a poloidally diverted tokamak equilibrium is derived. Under the assumption that the RMP is produced by coils at the low-field side such as those used to control edge localized modes (ELMs) it is demonstrated that the width of islands on different magnetic surfaces at the edge and the amount of divertor splitting are related to each other. Explanation is provided of aligned maxima of the perturbation spectra with the safety factor profile – an effect empirically observed in models of many perturbation coil designs.

I. INTRODUCTION

Resonant magnetic perturbations (RMPs) are being investigated as tool to control edge localized modes (ELMs), in particular their application to ITER is foreseen. The RMPs for ELM control are produced by coils whose design is specific to each tokamak. This method is reminiscent of the ergodic divertor on tokamaks Tore Supra and TEXTOR which also essentialy relies on RMPs produced by dedicated systems of coils, and many aspects are similar, especially the formation of magnetic islands on rational surfaces and possible stochastic transport when the islands overlap. However the presence of X-point in the poloidally diverted tokamaks provides some unique features: the splitting of divertor strike points, or divertor footprints – a signature of the homoclinic tangle created by the perturbation[1], and the divergence of the safety factor profile at the separatrix, due to which the number of rational surfaces even for one toroidal mode is infinite and island overlap on them is facilitated. The noncircular geometry of the plasma cross-section also complicates analytical treatment of magnetic islands, requiring cautious use of non-orthogonal coordinate systems.

Since both the homoclinic tangle and magnetic islands with the resulting stochasticity are consequences of the perturbation, it is natural to ask if there is any relation between them. It has been known that while every island chain is related to a different polodal mode of the perturbation, their sizes can be expressed by a single function – the Poincaré-type integral which also generalizes to an expression for the length of the divertor footprints[2].The present paper uses instead the more familiar formalism of the Melnikov integral[3] (a standard tool for the analysis of the homoclinic tangle) and explores the radial dependence of this function in the often encountered case of RMPs from the perturbation coils localized at the low-field side (LFS), as it is the case for most ELM control coil designs.

The paper starts with a review of the method to calculate island sizes. Care is taken to provide a formula valid in a plasma with a general aspect ratio and non-circular cross-section as this is essential for the edge pedestal region near the separatrix which is crucial for ELM control. It is shown how the island sizes are determined by a function whose definition is not affected by the coordinate singularity on the separatrix, and which we call the Melnikov-like function. The homoclinic tangle and divertor footprints are then explained together with the method of Melnikov integral for determining analytically the divertor footprints length. A particularily simple expression is given for the case when the perurbation has only one dominant toroidal mode. The relation between Melnikov integral and the Melnikov-like function is explained. Then we restrict our treatment to the case of perturbation localized on the LFS. Under this assumption the relation between modes at the different surfaces is derived and it is shown how does the divertor footprint length relate to the sizes of magnetic islands at the edge.

II. WIDTH OF MAGNETIC ISLANDS IN A REALISTIC GEOMETRY

A. Expression using the resonant modes of the perturbation

Nonaxisymmetric magnetic perturbations of a tokamak magnetic field produce chains of magnetic islands on magnetic surfaces with low-order rational values of the safety factor q. Those islands are created by resonances of the perturbation field $\delta\vec{\mathbf{B}}$ with the unperturbed field lines on the rational surface. To express these resonances we use a magnetic coordinate system[4] (s, θ^*, φ) where s is a flux surface label, θ^* the poloidal coordinate and φ the toroidal coordinate. The angular coordinates θ^*, φ are chosen as in the PEST coordinates[5] and the radial coordinate s is defined as square root of the normalized poloidal magnetic flux ψ_N: $s = \sqrt{\psi_N}$, in accordance with previous works (e.g. Refs. 6,7). The coordinate φ is simply the geometric toroidal angle and the coordinate system has the property that $\theta^* = o\varphi/q(s) + \text{const.}$ along a field line, where o represents the orientation of the magnetic field: $o = 1$ for the left-handed field and

$o = -1$ for the right-handed field[17]. The islands are created by the (m, n) Fourier component $\tilde{b}^1_{(m,n)}$ of the normalized perturbation $\delta b^1 \equiv B^1/B^3$, where $B^1 \equiv \delta\vec{\mathbf{B}} \cdot \nabla s$ is the contravariant s component of the perturbation and $B^3 \equiv \vec{\mathbf{B}} \cdot \nabla\varphi$ is the contravariant φ component of the equilibrium field. The Fourier transform is taken with respect to the θ^* and φ coordinates, thus we have

$$\delta b^1 = \sum_{m,n=-\infty}^{\infty} \tilde{b}^1_{(m,n)} \exp\left[\mathrm{i}(m\theta^* - n\varphi)\right] \tag{1}$$

and the Fourier harmonics can be obtained as

$$\tilde{b}^1_{(m,n)} = \frac{1}{(2\pi)^2} \oint \exp[-\mathrm{i}(m\theta^* - n\varphi)]\delta b^1 \,\mathrm{d}\theta^* \,\mathrm{d}\varphi. \tag{2}$$

A Fourier component is resonant with the unperturbed field lines when $q = om/n$. The values $\tilde{b}^1_{(m,n)}$ are complex, and as δb^1 is real, the following relation for the complex conjugate holds: $\left(\tilde{b}^1_{(m,n)}\right)^* = \tilde{b}^1_{(-m,-n)}$. An alternative to (1) is a representation using purely real coefficients:

$$\delta b^1 = \sum_{m=-\infty,n=1}^{\infty} b^1_{(m,n)} \sin(m\theta^* - n\varphi + \chi_{mn}) \tag{3}$$

$$b^1_{(m,n)} = 2|\tilde{b}^1_{(m,n)}| \tag{4}$$

$$\chi_{mn} = \arg \tilde{b}^1_{(m,n)} \tag{5}$$

Widely used formulae exist for determining the width of magnetic islands from the Fourier spectrum of the perturbation[6,8]. They are typically derived in a cylindrical geometry where the toroidal curvature is not being taken into account (the toroidal magnetic field is considered constant), thus B^3 in the expression for δb^1 is approximated by its value at the magnetic axis. As noted in Ref 9, this leads to an error in estimating the island width. In the example of TEXTOR and its dynamic ergodic divertor (DED), the island size was overestimated because the DED coils are located at the high-field side, thus the actual value of B^3 is larger and δb^1 is smaller than in the cylindrical approximation. For the ergodic divertor of Tore Supra, which was located at the low-field side, the island sizes were underestimated. It should be noted that while the toroidal field magnitude B_T varies with the radial distance R from the major axis as $B_\mathrm{T} \propto 1/R$, for the contravariant component the dependence is stronger: $B^3 \propto 1/R^2$.

Moreover the cylindrical formula for island widths uses r (the distance from the magnetic axis) as a radial coordinate and thus is valid only in a situation where the magnetic surfaces have circular and concentric cross-sections. In divertor tokamaks we are far from this geometry, especially in the edge region near the separatrix which is the most important when perturbations are used as an ELM control mechanism. We thus need a formula which would be usable in a general geometry, with a varying toroidal field and noncircular flux surfaces, using for example the coordinate s as a general flux surface label instead of r.

To derive this formula we introduce new coordinates $\chi \equiv \theta^* - n/m\varphi$ and $\overline{s} \equiv s - s_0$ where s_0 is the flux label of the resonant surface where $q = m/n$. The differential equation of the field line are

$$\frac{\mathrm{d}s}{\mathrm{d}\varphi} = \frac{B^1}{B^3} \tag{6}$$

$$\frac{\mathrm{d}\theta^*}{\mathrm{d}\varphi} = \frac{1}{q} \tag{7}$$

Using the coordinates χ and $\overline{s}$ and the relation

$$\frac{\mathrm{d}\chi}{\mathrm{d}\varphi} = \frac{1}{q} - \frac{n}{m} \tag{8}$$

the equation (6) becomes

$$1/q - n/m \,\mathrm{d}\overline{s} = B^1/B^3 \,\mathrm{d}\chi \tag{9}$$

Keeping only the resonant part of the perturbation, thus substituting B^1/B^3 by $b^1_{(m,n)} \sin(m\chi + \chi_{mn})$, we obtain

$$1/q - n/m \,\mathrm{d}\overline{s} = b^1_{(m,n)} \sin(m\chi + \chi_{mn}) \,\mathrm{d}\chi \tag{10}$$

Using a linear approximation of the left side, we obtain

$$\left.\frac{\mathrm{d}q^{-1}}{\mathrm{d}\overline{s}}\right|_{q=m/n} \overline{s} \,\mathrm{d}\overline{s} \approx b^1_{(m,n)} \sin(m\chi + \chi_{mn}) \,\mathrm{d}\chi \tag{11}$$

This equation can be easily integrated to obtain an algebraic equation for field lines:

$$\overline{s}^2 \approx \frac{2q^2 b^1_{(m,n)}}{q'm}[\cos(m\chi + \chi_{mn}) + C] \tag{12}$$

where $q' \equiv \mathrm{d}q/\,\mathrm{d}s$ at the resonant surface and C is an integration constant. The choice $C = 1$ corresponds to the island separatrix whose maximum radial excursion is the island half-width δ, given by the formula

$$\delta = \sqrt{\frac{4q^2 b^1_{(m,n)}}{q'm}} \tag{13}$$

An alternative to this approach is to use a Hamiltonian approach where the field lines are interpreted as trajectories of a Hamiltonian dynamical system whose Hamilton function is the poloidal flux and the perturbation is represented as a perturbed Hamiltonian (flux). This approach has been used in many theoretical works. We briefly review it in the appendix A and prove its equivalence to the approach described above. It should be emphasized that the hamiltonian approach automatically includes correctly the effects of toroidal geometry and non-circular cross-section – no corrections are necessary. It is however still important to have a correct formula using the perturbed magnetic field (13), because this is the approach usually used in numerical studies of perturbation coil designs, as the perturbed field can be readily calculated from the coil geometry by the Biot-Savart formula. We will also see that the harmonics of the perturbed field are directly related to the Melnikov function.

B. Expression using Melnikov-type integral

The coordinate system (θ^*, s) on a poloidal plane has a singularity at the separatrix. It is useful to define a value characterizing magnetic islands which, unlike $\tilde{b}^1_{(m,n)}$, will not use the θ^* coordinate, so it will stay well-defined even at the separatrix.

We start by defining a coordinate ϕ which will be used instead of θ^*. We follow a procedure used in the definition of the separatrix map and the Melnikov integral[3,10]. For every magnetic surface the point on the outboard midplane has $\phi = 0$. Following a field line parameterized by the toroidal angle φ from this point, we assign to any other point on the field line the value $\phi = \varphi$. Thus ϕ of a given point is the toroidal angle needed to reach it by following a field line from the outboard midplane. Since the field line returns to the same poloidal position after making q toroidal turns, the range of the coordinate ϕ needed to cover a magnetic surface in the poloidal plane is $(-q\pi, q\pi)$ where the endpoints of this interval are identified with each other. Together with a flux surface label such as s we obtain a coordinate system on the poloidal plane. The separatrix is a special case: it is covered by $\phi \in (-\infty, \infty)$ since q is infinite on the separatrix, and the X-point corresponds to $\phi = \pm\infty$. In this case ϕ is called a *homoclinic coordinate*[3]. As on a field line $\varphi = oq\theta^* + \text{const.}$ and $\theta^* = 0$ on the outboard midplane where $\phi = 0$, the relation between θ^* and ϕ is $\phi = oq\theta^*$. Using this relation, the definition (2) of $\tilde{b}^1_{(m,n)}$ can be rewritten as

$$\tilde{b}^1_{(m,n)} = \frac{1}{oq(2\pi)^2} \int_{-q\pi}^{q\pi} \int_0^{2\pi} \exp\left[-\mathrm{i}\left(o\frac{m}{q}\phi - n\varphi\right)\right] \delta b^1 \,\mathrm{d}\varphi \,\mathrm{d}\phi \tag{14}$$

If we define a toroidal perturbation Fourier mode $\tilde{b}^1_n$ as

$$\tilde{b}^1_n(\phi) = \frac{1}{2\pi} \int_0^{2\pi} \exp(\mathrm{i}n\varphi) \delta b^1(\phi, \varphi) \,\mathrm{d}\varphi \tag{15}$$

we may write (14) as

$$\tilde{b}^1_{(m,n)} = \frac{1}{o2\pi q} \int_{-q\pi}^{q\pi} \exp\left[-\mathrm{i}o\left(\frac{m}{q}\phi\right)\right] \tilde{b}^1_n(\phi) \,\mathrm{d}\phi \tag{16}$$

On resonant surfaces with $q = om/n$ this may be simplified to

$$\tilde{b}^1_{(m=onq,n)} = \frac{1}{o2\pi q} \int_{-q\pi}^{q\pi} \exp(-\mathrm{i}n\phi) \tilde{b}^1_n(\phi) \,\mathrm{d}\phi \tag{17}$$

($\tilde{b}^1_n$, $\tilde{b}^1_{(m,n)}$ and δb^1 all depend also on the magnetic surface, this was omitted from the expressions above for brevity). In (17) there appears a complex Melnikov-like function $\tilde{S}_n(s)$ given by

$$\tilde{S}_n(s) \equiv \int_{-q\pi}^{q\pi} \exp(-\mathrm{i}n\phi) \tilde{b}^1_n(s, \phi) \,\mathrm{d}\phi, \tag{18}$$

defined using the coordinate ϕ which does not have a singularity at the separatrix, so the definition can be extended to the separatrix:

$$\tilde{S}_n(s = 1) \equiv \int_{-\infty}^{\infty} \exp(-\mathrm{i}n\phi) \tilde{b}^1_n(s = 1, \phi) \,\mathrm{d}\phi. \tag{19}$$

The function $\tilde{S}_n$ fulfills our requirement: it can replace $\tilde{b}^1_{(m,n)} = \tilde{S}_n/(o2\pi q)$ and is defined using values which remain regular at the separatrix. The island width (13) can be expressed using $\tilde{S}_n$ instead of $\tilde{b}^1_{(m,n)}$:

$$\delta = \sqrt{\frac{4|\tilde{S}_n|}{n\pi q'}}. \tag{20}$$

The only remaining divergent term in (20) is the shear q' which grows to infinity at the separatrix. This dependence is physical: its consequence is that island width has a zero limit at the separatrix.

III. DIVERTOR FOOTPRINTS

Since the particle and heat transport are mostly parallel to field lines, the patterns of particle and heat flux to the divertor plates can be expected to be related to the divertor magnetic footprints, i.e. the patterns of intersections of field lines with the divertor. Field lines which carry heat and particle fluxes from inside the plasma are those with a high connection length, i.e. the number of toroidal turns following the field line in the plasma before it reaches the wall again.

Since the field lines can be interpreted as trajectories of a Hamiltonian dynamical system with the toroidal angle in the role of the time, methods of the theory of Hamiltonian systems can be used. A concept especially useful for the study of divertor footprints is the one of invariant manifolds[1]. An invariant manifold is a surface in the phase space of the dynamical system which remains invariant by the time evolution of the system, thus a trajectory with an initial point on the invariant manifold is constrained to remain on it[3]. In our case the trajectories are field lines and one example of invariant manifolds are the magnetic surfaces of the toroidally symmetric tokamak equilibrium. A particularly interesting case of invariant manifolds are the stable and unstable manifolds of hyperbolic fixed points. A stable manifold is formed by field lines asymptotically approaching the fixed point, while the unstable manifold is formed by field lines asymptotically leaving the fixed point. The definition depends on the direction in which the field lines are followed. If we follow them in the opposite direction, the stable manifold becomes unstable and vice versa. In plasma equilibria the hyperbolic fixed points are called X-points and are associated with the poloidal divertor or with magnetic islands. An example of invariant manifolds to a fixed point is the separatrix of a toroidally symmetric configuration with a poloidal divertor. Here the stable

and unstable manifolds coincide to form the separatrix. When a perturbation appears, the separatrix splits into the stable and unstable manifolds which no longer coincide, but intersect transversally infinitely many times. Close to the X-point in the direction from which the field lines approach it (the stable direction) the stable manifold is close to the unperturbed separatrix, but the unstable manifold wildly oscillates, creating lobes that become longer and narrower when the X-point is approached[1]. In the direction of field lines leaving the X-point (the unstable direction) we obtain a similar picture with the roles of the stable and unstable manifolds reversed. This complex structure is called a homoclinic or heteroclinic tangle. An important property of the invariant manifolds is that field lines can't cross them, because field lines can't intersect. Invariant manifolds thus act as boundaries for the field lines. Field lines originating in the hot plasma core are contained inside the invariant manifolds of the X-point and the only way they can reach the divertor targets is when the lobes of the (un)stable manifolds near the X-point intersect the target plates[11]. By tracing the intersection of the manifolds with the plates one obtains curves which delimit the region connected to the plasma core, characterized by mostly high connection length in the laminar plot. Those divertor footprints typically take the form of long spiralling bands, each band corresponding to the intersection of a protruding lobe of a stable or unstable manifold with the divertor.

The divertor footprints have a complicated inner structure and not all points inside the manifolds have high connection length. Some of them are connected to the opposite divertor plate after two poloidal turns by laminar flux tubes which do not penetrate deeply under the separatrix. The points with high connection lengths are the images of invariant manifolds of the X-points of the inner island chains[11]. This fine structure was studied in detail in[12]. Here we focus on the on the overall shape of the divertor footprints which is given by the invariant manifolds of the divertor X-point and is better experimentally accessible.

The length of the spiral can be characterized by the maximum value of s reached, i.e. the value s_{tip} at its tip. The difference $\Delta s_{\max}$ of s_{tip} and the separatrix value $s = 1$ expresses the radial distance on the divertor plate between the footprint's tip and the unperturbed strike point, which lies at the intersection of the unperturbed separatrix with the divertor plate. The unstable manifold[18] is the footprint's boundary and so the footprint's tip is the point on the manifold which is the most distant from the unperturbed separatrix, the distance in terms of s being $\Delta s_{\max}$. The value $\Delta s_{\max}$ thus quantifies the magnitude of the separatrix splitting.

To estimate the separation between the unperturbed separatrix and the unstable manifold we will follow two field lines – one in the unperturbed field, lying on the separatrix, and the other in the perturbed field, lying on the unstable manifold. They are parameterized by the toroidal angle φ. Let us choose them so that they are initially (in the vicinity of the X-point which they approach asymptotically when followed backwards in φ) close to each other. The parametric equations of the perturbed field line are

$$s = s'(\varphi) \tag{21}$$
$$\phi = \phi'(\varphi). \tag{22}$$

For the unperturbed field line they can be written explicitely using the definition of ϕ and the fact that the unperturbed field line lies on the separatrix where $s = 1$:

$$s = s(\varphi) = 1 \tag{23}$$
$$\phi = \phi(\varphi) = \varphi - \phi_0 \tag{24}$$

where the constant ϕ_0 determines the toroidal phase: it is the toroidal angle of the point where the field line crosses the outboard midplane.

The rate of change of s along the perturbed field line is

$$\frac{\mathrm{d}s'}{\mathrm{d}\varphi} = \delta b^1(s'(\varphi), \phi'(\varphi), \varphi) \tag{25}$$

If the perturbed field line does not deviate significantly as a result of the perturbation, we may use a first-order perturbative approximation and evaluate b^1 on the unperturbed field line:

$$\frac{\mathrm{d}s'}{\mathrm{d}\varphi} = \delta b^1(s = 1, \phi(\varphi), \varphi) \tag{26}$$

The deviation Δs of the perturbed field line from the unperturbed one after a full poloidal turn is given by the integral of (26):

$$\Delta s(\phi_0) = \int_{-\infty}^{\infty} \delta b^1(s = 1, \phi(\varphi) = \varphi - \phi_0, \varphi)\,\mathrm{d}\varphi \tag{27}$$

or using ϕ as the parameter:

$$\Delta s(\phi_0) = S(\phi_0) \equiv \int_{-\infty}^{\infty} \delta b^1(s = 1, \phi, \phi + \phi_0)\,\mathrm{d}\phi. \tag{28}$$

Note that $\Delta s(\phi_0)$ is a function of the toroidal phase ϕ_0 and may be zero: this happens when the unstable manifold intersects the unperturbed separatrix.

The function S defined by the integral (28) is closely related to the Melnikov function M:

$$M(\phi_0) = \int_{-\infty}^{\infty} \delta b^{\psi}(s = 1, \phi, \phi + \phi_0)\,\mathrm{d}\phi = \frac{\mathrm{d}\psi}{\mathrm{d}s} S(\phi_0) \tag{29}$$

where $\delta b^{\psi}(s = 1, \phi, \phi + \phi_0) = \frac{\mathrm{d}\psi}{\mathrm{d}s} b^1(s = 1, \phi, \phi + \phi_0)$ is the contravariant component of δB with respect to the ψ coordinate. The only difference between M and S is that S gives the change of s while M gives the change of ψ[3].

If there is only one toroidal mode $\tilde{b}^1_n(\phi)$ of the perturbation [cf. equation (15)], the function S can be replaced by a single complex number $\tilde{S}_n(s=1)$:

$$\begin{aligned} S(\phi_0) &= \int_{-\infty}^{\infty} \delta b^1(s=1,\phi,\phi+\phi_0)\,\mathrm{d}\phi \\ &= \int_{-\infty}^{\infty} 2\Re\left\{\exp[-\mathrm{i}n(\phi+\phi_0)]\tilde{b}^1_n(s=1,\phi)\right\}\mathrm{d}\phi \\ &= 2\Re\left[\exp(-\mathrm{i}n\phi_0)\int_{-\infty}^{\infty}\exp(-\mathrm{i}n\phi)\tilde{b}^1_n(s=1,\phi)\,\mathrm{d}\phi\right] \\ &= 2\Re\left[\exp(-\mathrm{i}n\phi_0)\tilde{S}_n(s=1)\right] \end{aligned} \tag{30}$$

$\tilde{S}_n(s=1)$ is defined by the equation (19), which also naturally extends the definition of $\tilde{S}_n(s)$ to the domain $s<1$. Analogously the value $\tilde{M}_n(s) \equiv \frac{\mathrm{d}\psi}{\mathrm{d}s}\tilde{S}_n(s)$ can be used to express the Melnikov function M as a single number $\tilde{M}_n(s=1)$.

The value $\Delta s_{\max}$ is the maximum deviation of the unstable manifold: $\Delta s_{\max} = \max_{\phi_0}\Delta s(\phi_0)$. Using $\tilde{S}_n(s=1)$ it is expressed as

$$\Delta s_{\max} = 2|\tilde{S}_n(s=1)| \tag{31}$$

The island widths and the magnitude of separatrix splitting, and consequently the length of the divertor footprints, are given by a single function $\tilde{S}_n(s)$: the island widths by its values at $s<1$ and the magnitude of splitting by the value at $s=1$.

It has been already known that island widths and the magnitude of splitting can be described by a signle radial function[2]: the Poincaré-type integral R_n which is an integral of the modes of the perturbed poloidal flux H_1 (cf. (A8)) instead of the perturbed field $\tilde{b}^1_n$. It can be shown that $\tilde{M}_n = \epsilon n R_n$ so for a single toroidal mode of the perturbation our formalism of the Melnikov-like functions S or M is equivalent to the Poincaré-type integral approach. The reference 2 gives also other results expressed in terms of the function R_n such as the width of the stochastic layer and the field line diffusion coefficient which can be also simply reformulated using Melnikov-like functions.

IV. SPECIFIC FORM OF THE MODES OF A LOCALIZED LOW-FIELD SIDE PERTURBATION

In the previous sections we introduced the Melnikov-like function $\tilde{S}_n$ and showed how it expresses both the sizes of the magnetic islands and the sizes of the divertor footprints. This is not sufficient to relate the sizes of the footprints to the sizes of the islands unless the radial dependence of $\tilde{S}_n$ is known. In this section an approximative form of this dependence at the edge will be given for the special case of external magnetic perturbations imposed by coils located at the low-field side. The motivation for this case is the use of such coils as an ELM control mechanism[13] where the the coils are supposed to impact the edge region where the ELMs originate.

We will use a simplified model of the perturbed magnetic field where the perturbation is localized at the low field side where the field line pitch angle $\mathrm{d}\varphi/\,\mathrm{d}\theta$ (θ being the geometric poloidal angle) is assumed to be constant poloidally and radially. This is a realistic assumption for the edge region near the separatrix which is our region of interest. We will note the local pitch angle q_1: $q_1 = \mathrm{d}\varphi/\,\mathrm{d}\theta = \mathrm{const}$. The variation of the safety factor is assumed to be caused only by the variation of the pitch angle in the regions where the perturbation is negligible: the high-field side and especially the X-point. This requires the perturbation coils to be placed sufficiently far from the X-point region.

Along a field line in the low field side region we have

$$\theta^* = o\varphi/q = oq_1\theta/q. \tag{32}$$

It follows that the ϕ function has a simple dependence on θ in this region:

$$\phi = q_1\theta. \tag{33}$$

The $\overline{m}$ Fourier component of the perturbation w.r.t the geometric poloidal angle θ is defined as

$$\tilde{b}'^1_{(\overline{m},n)} = \frac{1}{2\pi}\int \exp(-\mathrm{i}\overline{m}\theta)\tilde{b}'^1_n(\theta)\;\mathrm{d}\theta \tag{34}$$

where $\tilde{b}'^1_n(\theta)$ is the n toroidal Fourier component of $\delta b^1(\theta,\varphi)$ considered as a function of θ:

$$\tilde{b}'^1_n(\theta) \equiv \tilde{b}^1_n(\phi(\theta)). \tag{35}$$

We will now find the relation between the Fourier components $\tilde{b}^1_{(m,n)}$ and $\tilde{b}'^1_{(\overline{m},n)}$. We are neglecting the perturbation outside the region where the Eq. (33) holds which allows to express $\tilde{b}^1_{(m,n)}$ [Eq. (16)] in terms of the θ coordinate:

$$\tilde{b}^1_{(m,n)} = \frac{q_1}{o2\pi q}\int_{-\pi}^{\pi}\exp\left[-\mathrm{i}o\left(\frac{mq_1}{q}\theta\right)\right]\tilde{b}'^1_n(\theta)\,\mathrm{d}\theta \tag{36}$$

Equations (36) and (35) finally give simple relations between $\tilde{b}^1_{(m,n)}$ and $\tilde{b}'^1_{(\overline{m},n)}$:

$$\tilde{b}^1_{(m,n)} = \frac{q_1}{q}\tilde{b}'^1_{(mq_1/q,n)} = \frac{q_1}{q}\tilde{b}'^1_{(nq_1,n)} \tag{37}$$

and

$$\tilde{b}'^1_{(\overline{m},n)} = \frac{q}{q_1}\tilde{b}^1_{(\overline{m}q/q_1,n)}.$$

From those it can be seen why the maxima and minima of the spectrum $\tilde{b}^1_{(m,n)}$ in (m,s) space form "ridges" and "valleys" aligned with the q profile, as can be seen e.g. for the proposed ITER designs in Ref. 7 (Fig. 15c therein) and noted for DIII-D in Ref. 14 (see Fig. 1b therein). The Fourier component w.r.t. $\theta^* - \tilde{b}^1_{(m,n)}$ –

is given by Eq. (37). Assuming that the Fourier component of the perturbation w.r.t. θ – $\tilde{b}'^1_{(\overline{m},n)}$ – does not change significantly between different magnetic surfaces, the only radial dependence is the inverse proportionality to q which is the same for all the poloidal modes. If $\tilde{b}^1_{(m,n)}$ has the maximum on one surface with $s = s_1$ for $m = m_{\max}(s_1)$, on other resonant surface with $s = s_2$ it will have also maximum for $m = m_{\max}(s_2)$ equal to $m_{\max}(s_1)q(s_2)/q(s_1)$ so maxima will be aligned with the q profile which is given in the (m, s) space as the set of points satisfying $m = nq(s)$.

Using these resuls the an approximate radial dependence of $\tilde{b}^1_{(m,n)}$ can be found. The radial dependence of the geometric poloidal Fourier component $\tilde{B}^r_{\overline{m}}$ of the radial perturbation $B^r \equiv \delta\vec{\mathbf{B}} \cdot \vec{\mathbf{e}}_r$ (with $\vec{\mathbf{e}}_r$ being the unit vector perpendicular to the magnetic surfaces) is[15] $\tilde{B}^r_{\overline{m}} \propto r^{\overline{m}-1}$. The contravariant s component B^1 is given by $B^1 = B^r \partial s/\partial r$. Assuming that $\partial s/\partial r$ and B^3 do not depend significantly on the poloidal angle in the area with a non-negligible perturbation, the geometric poloidal Fourier component of the normalized contravariant perturbation is given by

$$\tilde{b}'^1_{(\overline{m},n)} \propto r^{\overline{m}-1} \frac{\partial s}{\partial r} \frac{1}{B^3}. \tag{38}$$

The radial dependence of $\tilde{b}^1_{(m,n)}$ is given by the formula (37) where Eq. (38) can be used to substitute for $\tilde{b}'^1_{(mq_1/q,n)}$.

For resonant modes we may use the Melnikov-like function instead. From Eqs. (33), (18) and (34) it follows that

$$\tilde{S}_n(s) = \frac{q_1}{o2\pi} \tilde{b}'^1_{(nq_1,n)} \tag{39}$$

The radial dependence of $\tilde{S}_n(s)$ can be obtained from Eqs. (38) and (39):

$$\tilde{S}_n(s) \propto q_1 r^{nq_1-1} \frac{\partial s}{\partial r} \frac{1}{B^3} \tag{40}$$

At a sufficiently narrow edge region the right-hand side is not strongly radially dependent, so we may expect the values of $\tilde{S}_n(s)$ on different resonant surface to be strongly correlated. Note that (40) and this conclusion applies also to the value on separatrix $\tilde{S}_n(s = 1)$, which is thus the limit of $\tilde{S}_n(s)$ at the resonant surfaces approaching the separatrix, because (40) does not contain discontinuous terms.

V. CONCLUSION

We derived a generalized formula for analytic estimation of width of magnetic islands which does not rely on a simplified cylindrical geometry, but instead takes into account toroidal toroidal geometry and arbitrary (i.e. noncircular) cross-section of magnetic surfaces. This makes it especially suitable for estimating the edge ergodization in an X-point tokamak geometry, where the edge region is substantially different from a cylindrical approximation. The formula is based on the perturbed magnetic field and we demonstrated its equivalence to formulae expressed in terms of the perturbed poloidal flux. We then formulated assumptions about the form of the perturbed magnetic field which correspond to the perturbations typically used inmo the ongoing effort to control ELMs with magnetic perturbations on a range of tokamaks. Namely, we suppose that the perturbation acts mostly in a region away from the X-point, where the pitch angle of the field lines does not have a significant radial variation in the region of interest, which is the edge zone near the separatrix. This assumption is valid for the coils used for ELM control experiments in most tokamaks, as well as the proposed coils for ITER. Using this assumption we then derived more concrete results about the perturbation harmonics which determine the island sizes. We demonstrated that all the resonant harmonics are correlated. Our result expresses formally the alignment of the maxima and minima of the perturbation spectra with the safety factor profile, which is often observed in the calculations of perturbation harmonics. We also show that the quantity which determines the island sizes is also directly linked to the Melnikov integral and thus determines the extent of the footprints on the divertor plates.

Our results show that by using coils on low field side it is not possible to create significantly diffferent resonant perturbations on different rational surfaces. Maximizing the resonant mode on one surface also leads to maximization of resonant modes on other surfaces. This is advantageous if one wants to optimize the coil system for maximum island overlap and stochastization. If one rather wants to study the effect on perturbation on each surface separately it might be more advantageous to choose a different position of the coils, as it is the case for the new perturbation coils on DIII-D. Maximizing the island overlap will also lead to maximization of divertor footprints due to the relation between island sizes and the Melnikov integral.

As our method is restricted to a LFS-localized perturbation, the results do not apply to a perturbation field created inside the plasma itself, e.g. a locked mode. In this case the relation between magnetic islands and the divertor footprints may be much less constrained.

Acknowledgments

This work was partly supported by the European Communities under the contracts of association between EURATOM, IPP.CR and CEA. The views and opinions expressed herein do not necessarily reflect those of the European Commission.

Appendix A: Hamiltonian representation of field lines and magnetic islands

In the theory of hamiltonian dynamical systems (see Ref. 16), the formula for the island width is derived using the hamiltonian description of field line dynamics, with the poloidal flux function in the role of the hamiltonian and the toroidal angle in the role of time (see e.g. Ref. 2). The hamiltonian is defined as

$$H = A_\varphi = RA_{\hat{\varphi}} \tag{A1}$$

where A_φ is the covariant toroidal component of the vector potential and $A_{\hat{\varphi}} = \vec{\mathbf{A}} \cdot \hat{\vec{\mathbf{e}}}_\varphi$ is the physical component, with $\hat{\vec{\mathbf{e}}}_\varphi$ being the unit basis vector in the toroidal direction. A convenient choice of canonical coordinates is the action-angle representation, where the action is the toroidal flux Φ and the angle is θ^*. The Hamiltonian equations are:

$$\frac{\mathrm{d}\theta^*}{\mathrm{d}\varphi} = \frac{\partial H}{\partial \Phi} \tag{A2}$$

$$\frac{\mathrm{d}\Phi}{\mathrm{d}\varphi} = -\frac{\partial H}{\partial \theta^*} \tag{A3}$$

In the equilibrium case H is a function of poloidal position only and is independent on the toroidal angle φ. Moreover, Φ and θ^* being action-angle variables, they are chosen so that H is only a function of Φ and Eq. (A3) is identically zero. A nonaxisymmetric perturbation is represented by the addition of a small term $\epsilon H_1(\Phi, \theta^*, \varphi)$ to the hamiltonian, which can then be written as

$$H(\Phi, \theta^*, \varphi) = H_0(\Phi) + \epsilon H_1(\Phi, \theta^*, \varphi). \tag{A4}$$

H_0 is the equilibrium part, which can be identified with the unperturbed poloidal flux ψ. The perturbed part $\epsilon H_1(\Phi, \theta^*, \varphi)$ corresponds to a perturbation $\delta A_\varphi(\Phi, \theta^*, \varphi)$ of A_φ. The equilibrium part has the property

$$\frac{\mathrm{d}H_0}{\mathrm{d}\Phi} = \frac{\mathrm{d}\psi}{\mathrm{d}\Phi} = \frac{1}{q} \tag{A5}$$

which reduces Eq. (A2) to the form (7). (We assume that the perturbation term $\epsilon \frac{\mathrm{d}H_1(\Phi,\theta^*,\varphi)}{\mathrm{d}\Phi}$ is negligible in comparison with the equilibrium term $1/q$ and can be neglected.) The equation (6) can be derived from (A3) by expressing the perturbed field δb^1 using the perturbed potential δA_φ. This expression is

$$\delta b^1 = -\frac{\mathrm{d}s}{\mathrm{d}\psi}\frac{1}{q}\frac{\partial \delta A_\varphi}{\partial \theta^*}. \tag{A6}$$

The derivative $\frac{\mathrm{d}s}{\mathrm{d}\varphi}$ can be expressed as

$$\frac{\mathrm{d}s}{\mathrm{d}\varphi} = \frac{\mathrm{d}s}{\mathrm{d}\psi}\frac{\mathrm{d}\psi}{\mathrm{d}\Phi}\frac{\mathrm{d}\Phi}{\mathrm{d}\varphi} = \frac{\mathrm{d}s}{\mathrm{d}\psi}\frac{1}{q}\frac{\mathrm{d}\Phi}{\mathrm{d}\varphi}. \tag{A7}$$

From Eqs. (A6) and (A7) it follows that Eq. (6) is equivalent to (A3).

It is useful to decompose the perturbed potential in Fourier modes, analogously to the decomposition (1) of δb^1:

$$\delta A_\varphi = \epsilon H_1 = \epsilon \sum_{m,n=-\infty}^{\infty} \tilde{H}_{(m,n)} \exp\left[\mathrm{i}(m\theta^* - n\varphi)\right] \tag{A8}$$

$$= \epsilon \sum_{m,n} H_{(m,n)} \cos(m\theta^* - n\varphi + \chi_{mn}) \tag{A9}$$

From (1), (A8) and (A6) we obtain the relation between $\tilde{b}^1_{(m,n)}$ and $\tilde{H}_{(m,n)}$:

$$\tilde{b}^1_{(m,n)} = -\frac{\mathrm{d}s}{\mathrm{d}\psi}\frac{1}{q}\mathrm{i}m\epsilon\tilde{H}_{(m,n)} \tag{A10}$$

$$b^1_{(m,n)} = \frac{\mathrm{d}s}{\mathrm{d}\psi}\frac{1}{q}m\epsilon H_{(m,n)}. \tag{A11}$$

The half-width of islands measured in terms of the action variable (toroidal flux Φ) is[16]:

$$\delta_\Phi = 2q\sqrt{\frac{\epsilon H_{(m,n)}}{\frac{\mathrm{d}q}{\mathrm{d}\Phi}}} \tag{A12}$$

In a linear approximation, the half-width in terms of s is related to δ_Φ by the relation $\delta_s = \frac{\mathrm{d}s}{\mathrm{d}\Phi}\delta_\Phi$. Moreover, $\frac{\mathrm{d}q}{\mathrm{d}\Phi} = \frac{\mathrm{d}s}{\mathrm{d}\Phi}q'$ and $\frac{\mathrm{d}s}{\mathrm{d}\Phi} = \frac{\mathrm{d}s}{\mathrm{d}\psi}\frac{1}{q}$, so using Eq. (A11) we see that the expressions (A12) and (13) are equivalent.

* Electronic address: cahyna@ipp.cas.cz

[1] T E Evans, R K W Roeder, J A Carter, B I Rapoport, M E Fenstermacher, and C J Lasnier. Experimental signatures of homoclinic tangles in poloidally diverted tokamaks. *Journal of Physics: Conference Series*, 7:174–190, 2005.

[2] S. S. Abdullaev, M. Jakubowski, M. Lehnen, O. Schmitz, and B. Unterberg. On description of magnetic stochasticity in poloidal divertor tokamaks. *Phys. Plasmas*, 15(4):042508, 2008.

[3] S. Wiggins. *Introduction to applied nonlinear systems and chaos*. Number 2 in Texts in Applied Mathematics. Springer-Verlag, New York Berlin Heidelberg, 1996.

[4] J.K. Park, A. H. Boozer, and J. E. Menard. Spectral asymmetry due to magnetic coordinates. *Phys. Plasmas*, 15(6):064501, 2008.

[5] R. C. Grimm, R. L. Dewar, and J. Manickam. Ideal MHD stability calculations in axisymmetric toroidal coordinate

systems. *J. Comput. Phys.*, 49(1):94–117, Jan 1983.

[6] M. Bécoulet, G. Huysmans, P. Thomas, P. Ghendrih, E. Nardon, A. Grosman, X. Garbet, W. Zwingman, R. Moyer, T. Evans, M. Schaffer, and A. Leonard. Edge localized modes control by stochastic magnetic fields. *Nucl. Fusion*, 45(11):1284–1292, 2005.

[7] M. Bécoulet, E. Nardon, G. Huysmans, W. Zwingmann, P. Thomas, M. Lipa, R. Moyer, T. Evans, V. Chuyanov, Y. Gribov, A. Polevoi, G. Vayakis, G. Federici, G. Saibene, A. Portone, A. Loarte, C. Doebert, C. Gimblett, J. Hastie, and V. Parail. Numerical study of the resonant magnetic perturbations for Type I edge localized modes control in ITER. *Nucl. Fusion*, 48(2):024003, 2008.

[8] Wesson. *Tokamaks*, chapter 7.2, pages 354–356. Clarendon, Oxford, 3 edition, 2004.

[9] A. Kaleck. On island formation in a locally perturbed tokamak equilibrium. *Contrib. Plasma Phys.*, 39(4):367–379, 1999.

[10] G. M. Zaslavsky. *Hamiltonian chaos and fractional dynamics*, chapter 6.2, pages 76–78. Oxford University Press, 3 edition, 2005.

[11] A. Wingen, T. E. Evans, and K. H. Spatschek. Footprint structures due to resonant magnetic perturbations in DIII-D. *Physics of Plasmas*, 16(4):042504, 2009.

[12] A. Wingen, T.E. Evans, and K.H. Spatschek. High resolution numerical studies of separatrix splitting due to non-axisymmetric perturbation in DIII-D. *Nuclear Fusion*, 49(5):055027, 2009.

[13] T.E. Evans, M.E. Fenstermacher, R.A. Moyer, T.H. Osborne, J.G. Watkins, P. Gohil, I. Joseph, M.J. Schaffer, L.R. Baylor, M. Bécoulet, J.A. Boedo, K.H. Burrell, J.S. deGrassie, K.H. Finken, T. Jernigan, M.W. Jakubowski, C.J. Lasnier, M. Lehnen, A.W. Leonard, J. Lonnroth, E. Nardon, V. Parail, O. Schmitz, B. Unterberg, and W.P. West. RMP ELM suppression in DIII-D plasmas with ITER similar shapes and collisionalities. *Nucl. Fusion*, 48(2):024002, 2008.

[14] I. Joseph, T.E. Evans, A.M. Runov, M.E. Fenstermacher, M. Groth, S.V. Kasilov, C.J. Lasnier, R.A. Moyer, G.D. Porter, M.J. Schaffer, R. Schneider, and J.G. Watkins. Calculation of stochastic thermal transport due to resonant magnetic perturbations in DIII-D. *Nucl. Fusion*, 48(4):045009, 2008.

[15] R. Fitzpatrick and T. C. Hender. Effect of a static external magnetic perturbation on resistive mode stability in tokamaks. *Phys. Plasmas*, 1(10):3337–3355, 1994.

[16] A.J. Lichtenberg and M.A. Lieberman. *Regular and stochastic motion*, volume 38 of *Applied Mathematical Sciences*. Springer-Verlag, New York, Heidelberg, Berlin, 1983.

[17] The orientation of the magnetic field depends on the relative orientation of plasma current and toroidal field: parallel in a right-handed field case, antiparallel in a left-handed field case.

[18] Or the stable manifold, depending on which strike point we consider – the inner or the outer one.

P1-41

Model for screening of resonant magnetic perturbations by plasma in a realistic tokamak geometry and its impact on divertor strike points

P. Cahyna[a*], E. Nardon[b] and JET EFDA Contributors[c]

[a]*Institute of Plasma Physics AS CR v.v.i., Association EURATOM/IPP.CR, Prague, Czech Republic*
[b]*Association EURATOM-CEA, CEA/DSM/IRFM, CEA Cadarache, 13108 St-Paul-lez-Durance, France*
[c]*See the Appendix of F. Romanelli et al., Proceedings of the 22nd IAEA Fusion Energy Conference 2008, Geneva, Switzerland*

Abstract

This work addresses the question of the relation between strike-point splitting and magnetic stochasticity at the edge of a poloidally diverted tokamak in the presence of externally imposed magnetic perturbations. More specifically, ad-hoc helical current sheets are introduced in order to mimic a hypothetical screening of the external resonant magnetic perturbations by the plasma. These current sheets, which suppress magnetic islands, are found to reduce the amount of splitting expected at the target, which suggests that screening effects should be observable experimentally.

JNM keywords: Theory and Modelling, Plasma properties, Plasma-Materials Interaction

PSI-19 Keywords: Divertor, Edge pedestal, Magnetic Topology, Power deposition, Stochastic boundary

PACS: 52.40.Hf, 52.55.Fa, 52.55.Rk

***Corresponding author address: Institute of Plasma Physics AS CR v.v.i., Za Slovankou 1782/3**

182 00 Prague 8 Czech Republic

***Corresponding author E-mail: cahyna@ipp.cas.cz**

Presenting author: Pavel Cahyna

Presenting author e-mail: cahyna@ipp.cas.cz

Introduction

An axisymmetric, single null, poloidally diverted tokamak has two strike-lines where the plasma hits the divertor targets: one on the high field side (HFS) and one on the low field side (LFS). In the presence of a non-axisymmetric magnetic perturbation, these strike-lines are replaced by spiralling patterns [1]. If an experimental profile (e.g. D_α or infrared [IR]) is taken along the radial direction at a given toroidal location, the strike-points are then observed to split. Such a splitting is for instance commonly observed during locked modes [2]. In the presence of external resonant magnetic perturbations (RMPs) a splitting may also be expected. On DIII-D, the splitting is observed during Edge Localised Mode (ELM)-suppressed discharges using n=3 perturbations from the I-coils [3,4]. It is important to notice that the splitting is seen much more clearly on particle flux (D_α) profiles than on heat flux (IR) profiles, at least in low collisionality experiments [3] (at high collisionality, the splitting is however clearly observed on the heat flux [4]). Recently, DIII-D also reported on splitting observations (both on heat and particle fluxes) in L-mode plasmas [5]. JET (using the Error Field Correction Coils (EFCCs)) and MAST (using n=3 perturbations from the ELM control coils [6]) find consistent effects on the heat flux profiles: the splitting is observed in L-mode but not in H-mode [7].

In the field of ELM control by RMPs from perturbation coils, one major question is to know whether the RMPs stochastize the magnetic field at the edge of the plasma, as assumed by the vacuum modelling. Studies based on the vacuum field assumption [8] have led to a design criterion for the considered ITER ELM control coils [9]. However, two important elements cast doubt on the stochastization of the magnetic field. The first one is the absence of a degradation of the electron temperature gradient in the edge transport barrier, which would be expected in the presence of a stochastic field [10]. The second one is the strong rotational screening effect [11,12] found in simulations of the DIII-D ELM suppression experiments [13,14]. On the other hand the RMPs can also become amplified by the interaction with MHD modes [15] – an effect which works against rotational screening [16].

In this paper, we analyse the possible consequences of the rotational screening (without taking into account the possibility of amplification by MHD modes) on the strike-point splitting in order to assess whether screening effects may explain the absence of a clear splitting of the heat flux profiles in some experiments, in particular in the DIII-D, JET and MAST H-mode discharges referred to above.

Modelling and theoretical understanding of the strike-point splitting

Under a non-axisymmetric perturbation the magnetic separatrix splits into two surfaces: the stable and unstable manifolds of the X-point. The stable (resp. unstable) manifold is the set of field lines that asymptotically approach the X-point when followed in the direction of (resp. opposite to) the magnetic field. The manifolds are of interest to experiments because they delimit the first passage through the wall of field lines arriving from the plasma core. Their intersections with the divertor plates thus define areas (divertor footprints) where high heat and particle fluxes are carried from the plasma core along the field lines [17]. Those areas take typically the form of spirals of high temperature and particle recycling around the original (unperturbed) divertor strike point.

The divertor footprints can be visualized by plotting a map of the connection length on the divertor plates (a laminar plot) [18]. The connection length is the distance (measured as the number of toroidal turns) needed to reach the wall again by following a field line starting at a given position. Field lines with large connection lengths remain in the plasma for many turns and carry high fluxes from the hot plasma core. The extent of the footprint can be approximated analytically using the Melnikov function [19] whose maximum is the difference of ψ between the unperturbed strike point and the tip of the footprint [20]. When the perturbation has one dominant toroidal mode further simplification is possible and the difference of ψ can be expressed using a single number – the one-mode Melnikov integral $\tilde{M}_n$ [20].

An example of the laminar plot and the stable manifold is shown on Figure 1 (left plot) for an equilibrium predicted for the COMPASS tokamak [21] in the case of a magnetic field of 1.2 T, low triangularity, single-null (SND) geometry and heating by one co-injected neutral beam [22]. The n=2 perturbation is imposed by the existing perturbation coils whose description can be found in [23].

Physics-motivated method for taking screening currents into account

Coordinate system and resonant field components

We use an (s, φ, θ^*) system of equilibrium coordinates, where $s \equiv \left|(\psi - \psi_{axis})/(\psi_{sep} - \psi_{axis})\right|^{1/2}$ (with ψ the poloidal magnetic flux), φ the geometric toroidal angle and θ^* the corresponding straight field line poloidal angle (i.e. such that $\left|d\varphi/d\theta^*\right| = \text{const} = q$ along a field line, with q the safety factor).

Magnetic islands are known to arise from the component of the magnetic perturbation which is perpendicular to the equilibrium flux surfaces. We characterise the latter by the quantity

$b^1 \equiv \vec{B}\cdot\vec{\nabla}s/\vec{B}\cdot\vec{\nabla}\varphi$. It can be shown that its Fourier components b^1_{mn} are directly related to the half-width of the magnetic islands and moreover they are related to the Melnikov integral [24], more precisely proportional to a function which is a generalization of the one-mode Melnikov integral $\widetilde{M}_n$ (the Melnikov-like function) [20] or equivalently the Poincaré integral [25]. At the same time the radial extent of the invariant manifolds (estimated by the Melnikov integral) gives the lower bound of the stochastic layer width because the intersections of the invariant manifolds (the homoclinic tangle) create themselves a thin stochastic layer. The actual stochastic layer can be much wider than this lower bound because it is formed also by the overlap of the magnetic islands [24].

Model of the screening currents

Without loss of generality, we consider one toroidal mode *n* of the screening currents in the plasma. A generic current can be represented a Fourier sum of these modes which are independent thanks to the toroidal symmetry.

Screening currents are modelled under the following assumptions:

1) They are radially localised on infinitesimally thin layers around the resonant surfaces: $\vec{j} = \sum_{q\in S}\delta\left(s - s_{q,n}\right)\vec{j}_{q,n}$, where δ is the Dirac delta function and S is the set of rational values of the safety factor which define the screening surfaces: $q = m/n$ for integer *m* and the given toroidal mode number *n*. The corresponding values of the radial coordinate *s* are noted as $s_{q,n}$.

2) They are parallel to the equilibrium field lines: $\vec{j}_{q,n} = j_{q,n}/B_{eq}\cdot\vec{B}_{eq}$.

3) They are divergence-free: $\vec{\nabla}\cdot\vec{j} = 0$, which implies that $\alpha_{q,n} \equiv j_{q,n}/B_{eq}$ is constant on a field line.

The first assumption corresponds to the fact that the current density is generally localised in a thin layer around the resonant surface [11,12,26]. The second assumption follows from the fact that the screening currents are induced to oppose the radial perturbation and to create a radial screening field perpendicular to the field lines a parallel current is needed. The third assumption expresses quasi-neutrality.

The angular dependence of $\alpha_{q,n}$ has the form of one Fourier mode:

$$\alpha_{q,n}\left(\theta^*,\varphi\right) = \Re\left(\beta_{mn}\exp\left[\mathrm{i}\left(m\theta^* + n\varphi\right)\right]\right) \qquad (1)$$

with $m = qn$, where the toroidal dependence is the consequence of working with one toroidal mode, while the poloidal dependence follows from the third requirement: $\alpha_{q,n}$ constant on

field lines. β_{mn} is a complex quantity containing both the amplitude and phase of $\alpha_{q,n}$. Thus, the screening current density can be expressed as a linear combination of base currents $\vec{j}_{mn,0}$

$$\vec{j} = \Re\left(\sum_{m;m/n\in S} I_{mn} \vec{j}_{mn,0} \right), \tag{2}$$

with coefficients $I_{mn} \equiv \beta_{mn} B_{ref} / j_{ref}$ and the base currents

$$\vec{j}_{mn,0}(s,\theta^*,\varphi) \equiv \frac{j_{ref}}{B_{ref}} \delta(s - s_{q,n}) \exp\left[i(m\theta^* + n\varphi) \right] \cdot \vec{B}_{eq} . \tag{3}$$

B_{ref} / j_{ref} is an arbitrary value expressing the choice of base current amplitudes (and thus the normalization of I_{mn}) relative to the magnetic field strength.

Coupling matrix

We calculate the field $\vec{B}_{mn,0}$ created by the base resonant current $\vec{j}_{mn,0}$. The numerical method approximates $\vec{j}_{mn,0}$ by discrete helical current filaments on the screening surface and calculates their vector potential on a flux surface aligned mesh. It avoids the mesh points which are too close to the screening surface and uses instead an interpolation in order that the discrete approximation of currents not cause an error. $\vec{B}_{mn,0}$ is then obtained as the curl of the interpolated vector potential, which gives all its components and automatically satisfies the condition of zero divergence. The corresponding b^1 component, denoted $b_0^{1,mn}$, is then Fourier transformed at each resonant surface $q = m'/n'$ in order to obtain the resonant components $b_{m'n',0}^{1,mn}$. Thus, $b_{m'n',0}^{1,mn}$ designates the resonant part, on the $q = m'/n'$ surface, of the b^1 created by a resonant current $\vec{j}_{mn,0}$ located at the $q = m/n$ surface. Thanks to the toroidal symmetry of the field equations in $b_{m'n',0}^{1,mn}$ we have $n = n'$, otherwise $b_{m'n',0}^{1,mn} = 0$.

The plasma response field corresponding to the total current $\vec{j}$ as given by Eq. (2) is $\vec{B}_{\text{plasma}} = \Re\left(\sum_{m;m/n\in S} I_{mn} \vec{B}_{mn,0} \right)$ whose resonant b^1 components are $b_{m'n,\text{plasma}}^1 = \sum_m b_{m'n,0}^{1,mn} \cdot I_{mn} / 2$ and $b_{-m'-n,\text{plasma}}^1 = \sum_m \left(b_{m'n,0}^{1,mn} \cdot I_{mn} \right)^* / 2$. The RHS is the product of the matrix $b_{m'n,0}^{1,mn}$ with subscripts m and m', which we call the coupling matrix, by the current vector I_{mn}.

Calculation of the screened field by inversion of the coupling matrix

To determine the coefficients I_{mn} one needs an assumption about the character of the plasma response, i.e. if it amplifies or screens the perturbation and by what amount. In the following we assume an efficient screening which completely eliminates magnetic islands at the rational surfaces in the pedestal region, i.e. the resonant Fourier components b^1_{mn} of the total magnetic field are zero.

The procedure to obtain the screened field begins with the calculation of the coupling matrix, for a given choice of the set of screening surfaces *S*. Independently, the vacuum RMP spectrum $b^1_{m'n',\mathrm{vac}}$ is calculated from the coil geometry. The screening current distribution I^{screen}_{mn} is obtained by solving $\sum_m b^{1,mn}_{m'n,0} \cdot I^{screen}_{mn} = -2b^1_{m'n,\mathrm{vac}}$, i.e. by inverting the coupling matrix. The full, screened field $\vec{B}_{full}$ is then obtained as $\vec{B}_{full} = \vec{B}_{vac} + \Re\left(\sum_m I^{screen}_{mn} \vec{B}_{mn,0}\right)$. It is easy to verify that its resonant Fourier components $b^1_{mn,full}$ on rational surfaces with $q = m/n \in S$ satisfy the property $b^1_{mn,full} = 0$ up to the error introduced by the numerical method.

If the set *S* consists of only one screening surface, the coupling matrix is trivial, with one element. The screening currents for each surface alone are given by using only the diagonal terms of the coupling matrix: $I^{screen}_{mn,\mathrm{diag}} = -2\, b^1_{mn,\mathrm{vac}} \big/ b^{1,mn}_{mn,0}$. If more screening surfaces are considered, the currents I^{screen}_{mn} on each one required to cancel the resonant components may be different than for one surface alone due to off-diagonal components of the coupling matrix. This effect can be quantified by the ratio between I^{screen}_{mn} calculated using the full matrix and $I^{screen}_{mn,\mathrm{diag}}$. If for example the ratio is lower than 1, it means that the perturbation field from different screening surfaces reinforce each other and smaller currents are required for screening than if screening were due only to one surface. This is the case for all the examples described in the next subsection, where we present actual values of this ratio. This is one of the geometry effects neglected in cylindrical models such as [13,14,27] where the coupling matrix is always diagonal.

Numerical examples

We chose two cases to illustrate the method and to show the effect of screening on footprints: the COMPASS case described above and an equilibrium from an ELM control experiment on JET with n=2 perturbation of the EFCCs [7] (shot #79729 at 19.38s). For both cases we first calculate the screening field needed to cancel the perturbation on a single surface ($q = 4/2$ for

COMPASS, $q = 5/2$ for JET). In those cases the coupling matrix is trivial, with one element. Then we calculate the screening field choosing four screening surfaces with $q = 4/2,...,7/2$ for COMPASS, $q = 5/2,...,8/2$ for JET. The n=2 mode of the screening field b^1_{screen} as a function of θ^* on the outermost screening surface is shown on Figure 2 for the four cases (each equilibrium with one and four screening surfaces). The screening field of one screening surface is distributed all over the resonant surface, due to the helical structure of the screening current, while for four screening surfaces the screening field is mostly localized on the LFS. Both COMPASS and JET show this effect. It shall be noted that the vacuum field is also localized at the LFS because of the position of the coils in both tokamaks, so the screening field of four currents is more similar to the vacuum field than the field of a single current. The ratio $I^{screen}_{m=5n=2} / I^{screen}_{m=5n=2,\text{diag}}$ for JET is 0.63, for COMPASS $I^{screen}_{m=4n=2} / I^{screen}_{m=4n=2,\text{diag}}$ is 0.72, with similar and generally decreasing values for other surfaces.

The numerical error in determining the screening current amplitudes was estimated by increasing four times the resolution of the discretization of the screening currents. The largest change was observed for the outermost surface (6.3% for COMPASS, 8.3% for JET). The error decreases for the inner surfaces down to 0.1% for COMPASS, 0.2% for JET at the innermost surface.

Impact of screening currents on the splitting

For the $b^{1,mn}_0$ field created by the resonant current $\vec{j}_{mn,0}$ we may compute the one-mode Melnikov integral at the separatrix which we will note $\widetilde{M}^{mn}_0$. The total Melnikov integral which estimates the splitting from all the screening currents and the vacuum field is

$$\widetilde{M}_n = \widetilde{M}_{n,vac} + \sum_{m;m/n\in S} I^{screen}_{mn} \widetilde{M}^{mn}_0 \qquad (4)$$

The ratio of the footprint extent measured in terms of ψ for the screened vs. the vacuum field is given by $\left|\widetilde{M}_n\right| / \left|\widetilde{M}_{n,vac}\right|$. Table 1 lists this value for the COMPASS and JET cases as a function of the choice of screening currents, and Figure 3 shows the same data.

In both cases a significant reduction of the footprints is predicted by the Melnikov integral when four screening currents are considered. To confirm this we plotted the stable manifold and a laminar plot around the inner strike point for COMPASS for the screened field and the stable manifold for the vacuum field for comparison (Figure 1, right plot). The stable manifold forms the boundary of the footprints as expected and indeed shows a clear reduction in comparison to the vacuum stable manifold. The difference of ψ (normalized to the poloidal

flux at the separatrix) between the footprint tip and the base is 6.8 10^{-3}, while the Melnikov integral method predicts 5.3 10^{-3}. The inaccuracy of the Melnikov method is significantly lower (relative error below 1/10) for the other cases in the table which do not include the outermost (m=7) screening surface. Similar result was found for the JET case (laminar plots are shown in [7]): the actual difference is 3.4 10^{-3}, while the Melnikov integral method predicts 3.6 10^{-3}. The outermost (m=8) surface can also lead to a large error in the Melnikov integral estimation, especially with the m=8 surface alone, where the Melnikov integral predicts reduction of footprints by a factor of 0.89, while the actual reduction is 0.56.

Discussion and conclusions

We developed a model of the plasma response currents on resonant surfaces and the resulting field, based on the realistic geometry of poloidally diverted tokamak plasmas and thus appropriate for the region near the separatrix, which is crucial for the ELM mitigation by external perturbations and also for the impact of perturbations on the divertor strike points (strike point splitting). To compute the screening currents we used the assumption of complete screening of resonant modes in the edge region, because we do not simulate the plasma response self-consistently. This is justified by earlier results indicating that the resonant modes of the perturbation will be suppressed by strong gradients in the pedestal region [13,14]. As we do not directly couple our model with these results yet, we performed a scan of different possible combinations of screening currents. In future work we plan to use the results of self-consistent MHD models to determine the set of screening surfaces and the screening factors, which will also allow for incomplete screening. The reason for this approach is that those MHD models use a cylindrical geometry in which the effect on the divertor strike points can't be represented, and our model fills this gap. While there are MHD codes (e.g. NIMROD [16], M3D [28] and JOREK [29]) using a realistic geometry which thus can model the strike points themselves (as shown for JOREK in [29]) without needing our model, they have limitations in the physics included (lack of realistic resistivity) which justifies the interest of our approach.

The resulting screened field was used to model magnetic footprints on the divertor by tracing the field lines. For two example cases (single-null equilibria of COMPASS and JET with $n = 2$ perturbations) we have shown notable differences in comparison with the vacuum field. The screening significantly reduces the spiralling patterns of field lines coming from inside the plasma. The spirals are shortened along their axis, the position of the axis is not affected. Reducing the coil current in a vacuum model has a similar impact. Comparison with experimental observation of strike point splitting could be thus used for validating the starting

assumption about the screening. Coupling with MHD models will also enable us to do scans of the dependence of strike point splitting on the collisionality (and thus resistivity) and rotation, which are both important parameters for the screening effect, and compare the results with experiments. It can be expected that higher collisionality and slower rotation will reduce the screening and enhance the footprints. The discussion of experimental results is however more complicated than a simple comparison with the predicted magnetic footprints because of the deformation of flux surfaces beyond the separatrix. The field of the screening currents decays quickly outside of the separatrix and at the same time the field of the coils increases as they are approached. Even if the screening reduces significantly the splitting of the perturbed separatrix, for the flux surfaces in the scrape-off layer the screening can be then expected to be less efficient and their distortion to remain. The particles in the scrape-off layer would follow those distorted surfaces. This shows that it is necessary to distinguish between particle and heat flux and that the presence of splitting of the particle flux does not necessarily imply the absence of screening. Indeed, as mentioned in the Introduction, in the DIII-D low collisionality experiments the splitting of particle flux and heat flux are different. Transport modelling using the vacuum perturbation failed to explain this observation [30] and it will be thus interesting to repeat it for the screened field as calculated by our model to see if the screening can provide an explanation.

The reduction of footprints can be efficiently estimated by the Melnikov integral method, but it is sometimes inaccurate when a screening current very close to the separatrix is included, probably because of the strong variation of the screening field while the Melnikov method (a first-order perturbation method) needs the perturbation field to be slowly varying in the vicinity of the separatrix.

The reduction of footprints can be qualitatively understood from the fact that the screening field is mostly localized at the LFS, just as the field of the coils. It can be shown that for a LFS-localized perturbation field the Melnikov integral which estimates the splitting is linked to the values of the Melnikov-like function on the resonant surfaces which is proportional to the resonant modes of the perturbation [20]. Thus eliminating the resonant modes shall also mostly eliminate the Melnikov integral and splitting. It shall be noted that for a single screening surface the field is not at all localized so this reasoning does not apply. Indeed, we have seen that a single screening surface reduces the Melnikov integral only weakly.

Our model is designed to represent one significant feature of the plasma response to the perturbations – the surface screening currents localized at resonant surfaces. The ideal MHD models assume them so the opening of magnetic islands is prevented [15], while the resistive

MHD models predict them self-consistently. There are however other ways of plasma reaction to the perturbation, namely coupling to MHD modes which can provide amplification of the applied perturbation [15,16,31], especially important at high β [32], and those are not represented in our approach.

Acknowledgements

We thank V. Fuchs for providing the COMPASS magnetic equilibrium used in the simulations. The access to the MetaCentrum computing facilities provided under the research intent MSM6383917201 is appreciated. This work, supported by AS CR #AV0Z20430508, MSMT #7G09042 and #LA08048 and by the European Communities under the contracts of Association between EURATOM and IPP.CR and CEA was carried out within the framework of the European Fusion Development Agreement. The views and opinions expressed herein do not necessarily reflect those of the European Commission.

References

[1] N.Pomphrey and A.Reiman, Phys.Fluids B **4** (1992) 938

[2] T.E. Evans et al., J. Nucl. Mater. **220-222** (1995) 235

[3] O. Schmitz et al., Plasma Phys. Control. Fusion **50** (2008) 124029

[4] T.E. Evans et al., J. Nucl. Mater. **363-365** (2007) 570

[5] O. Schmitz et al., this issue

[6] E. Nardon et al., Plasma Phys. Control. Fusion **51** (2009) 124010

[7] E. Nardon et al., this issue

[8] M.E. Fenstermacher et al., Phys. Plasmas **15** (2008) 056122

[9] R. Hawryluk et al., Nucl. Fusion **49** (2009) 065012

[10] A.B. Rechester and M.N. Rosenbluth, Phys. Rev. Lett. **40** (1978) 38

[11] R. Fitzpatrick, Nucl. Fusion **33** (1993) 1049

[12] R. Fitzpatrick, Phys. Plasmas **5** (1998) 3325

[13] M.F. Heyn et al., Nucl. Fusion **48** (2008) 024005

[14] E. Nardon et al., Nucl. Fusion **50** (2010) 034002

[15] J.K. Park, et al., Phys. Plasmas **16** (2008) 056115

[16] V. Izzo and I. Joseph, Nucl. Fusion **48** (2008) 115004

[17] T. E. Evans et al., J. Phys.: Conf. Ser. **7** (2005) 174

[18] A. Wingen et al., Phys. Plasmas **16** (2009) 042504

[19] S. Wiggins, "Introduction to applied nonlinear systems and chaos", Texts in Applied Mathematics 2, Springer-Verlag, New York Berlin Heidelberg, 1996

[20] P. Cahyna and E. Nardon, "Resonant magnetic perturbations and divertor footprints in poloidally diverted tokamaks", arXiv:1005.3663 [physics.plasm-ph]

[21] R. Pánek et al., Czech. J. Phys. **56** (2006) B125-37

[22] J. Urban et al., Plasma Phys. Control. Fusion **52** (2010) 045008

[23] P. Cahyna et al., Nucl. Fusion **49** (2009) 055024

[24] I. Joseph et al., Nucl. Fusion **48** (2008) 045009

[25] S.A. Abdullaev et al., Phys. Plasmas **15** (2008) 042508

[26] R.D. Hazeltine and J.D. Meiss, "Plasma Confinement", Dover, Mineola, New York, 2003, Section 7.4

[27] M. Bécoulet et al., Nucl. Fusion **49** (2009) 085011

[28] H.R. Strauss et al., Nucl. Fusion **49** (2009) 055025

[29] G.T.A. Huysmans et al., Plasma Phys. Control. Fusion **51** (2009) 124012

[30] H. Frerichs et al., Nucl. Fusion **50** (2010) 034004
[31] M. Lanctot et al., Phys. Plasmas **17** (2010) 030701
[32] H. Reimerdes et al., Nucl. Fusion **49** (2009) 115001

Tables

COMPASS	m=4	m=4,5	m=4,5,6	m=4,5,6,7
$\left\|\widetilde{M}_2\right\|/\left\|\widetilde{M}_{2,vac}\right\|$	0.73	0.54	0.45	0.27
JET	m=5	m=5,6	m=5,6,7	m=5,6,7,8
$\left\|\widetilde{M}_2\right\|/\left\|\widetilde{M}_{2,vac}\right\|$	0.69	0.50	0.30	0.26

Table 1 One mode Melnikov integral of the screened perturbation normalized to the Melnikov integral of the vacuum perturbation, for different choices of the screening currents. $\left|\widetilde{M}_{2,vac}\right|$ is 2.00 10^{-2} for COMPASS, 1.38 10^{-2} for JET, relative to the poloidal flux at the separatrix.

Figure captions

Figure 1 Laminar plot of the connection length (as a number of toroidal turns) on the divertor of COMPASS near the HFS strike point with a vacuum (left) and screened (right) perturbation field. White line: The stable manifold of the vacuum perturbation field. Black line: the stable manifold of the screened perturbation field.

Figure 2 Poloidal dependence of the real part of the n=2 component of the relative perturbation field b^1 at the q=5/2 resonant surface for JET, shot #79729 and q=4/2 for COMPASS. Fields of one screening current (full lines) and four screening currents (dashed lines) are shown.

Figure 3 The relative Melnikov integral $\left|\widetilde{M}_2\right|/\left|\widetilde{M}_{2,vac}\right|$ from Table 1 as a function of the number of screening surfaces: from one at the q=5/2 resonant surface for JET, shot #79729 and q=4/2 for COMPASS, up to four of them.

Figures

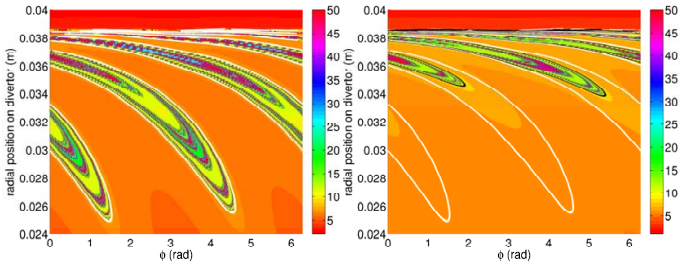

Figure 1 Laminar plot of the connection length (as a number of toroidal turns) on the divertor of COMPASS near the HFS strike point with a vacuum (left) and screened (right) perturbation field. White line: The stable manifold of the vacuum perturbation field. Black line: the stable manifold of the screened perturbation field.

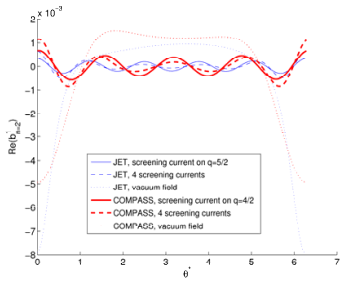

Figure 2 Poloidal dependence of the real part of the n=2 component of the relative perturbation field b^1 at the q=5/2 resonant surface for JET, shot #79729 and q=4/2 for COMPASS. Fields of one screening current (full lines) and four screening currents (dashed lines) are shown.

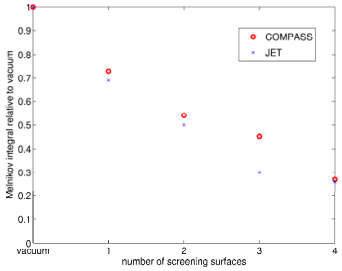

Figure 3 The relative Melnikov integral $\left|\widetilde{M}_2\right|/\left|\widetilde{M}_{2,vac}\right|$ from Table 1 as a function of the number of screening surfaces: from one at the q=5/2 resonant surface for JET, shot #79729 and q=4/2 for COMPASS, up to four of them.

8.1 Conclusions of chapter 8

We have seen that the length of footprints is correlated with the resonant perturbation modes from external coils in the vacuum approximation. The question now is how the overall shape of footprints is affected by the perturbation strength (i.e. the current in the perturbation coils). It turns out that only the length of the footprints varies while their shape is unchanged. We plan to enhance the first paper with an analytical derivation of this result and then publish it in a journal.

This result extends even to the case with screening of RMPs by the plasma. If the RMPs are screened, the footprints are substantially reduced. There however must be several resonant surfaces with the screening currents which make the screening field look more like the vacuum field, i.e. localized on the LFS. Investigation of why this is the case is postponed to a future work. This results presents an interesting possibility of diagnosing the screening of RMPs. The interpretation of experimental results is of course more complicated, as discussed in the conclusion of the second paper, and we plan to extend our field line tracing with true plasma transport simulations which shall be able to predict better the experimental results.

Chapter 9

Disruptions and runaway electrons

9.1 Disruptions

A major disruption is an abrupt plasma termination event causing the release of all the plasma stored energy. Major disruptions are triggered by MHD instabilities, which are in turn caused by crossing the MHD stability limits (such as the Troyon beta limit), growth of MHD modes (such as mode locking) and radiative instability, caused by crossing the density limit and/or impurity accumulation. The MHD instabilities cause a rapid loss of the plasma thermal energy to the wall in a phase called the *thermal quench*. The associated redistribution (flattening) of the current profile causes the plasma current to momentarily rise because of the decrease of the inductance. The decreased temperature however increases the resistivity and the current decays, accompanied by a rise of the loop voltage. This phase is called *current quench*. During the current quench the magnetic energy of the plasma poloidal field is released.

Elongated plasmas are intrinsically vertically unstable. When the vertical control fails (e.g. reaching current limit following a challenge) the plasma moves vertically leading to a *Vertical Displacement Event (VDE)*. In addition, loss of vertical control also occurs during quench as the consequence of the rapid change of plasma parameters with which the feedback control cannot cope.

The increased loop voltage during the current quench leads to a formation of a beam of relativistic electrons, called *runaway electrons (REs)* with very little interactions with the rest of the plasma (see the next section 9.2). The current carried by runaway electrons does not encounter resistance, in

contrast to the thermal plasma current, so it is not affected by the increase of resistivity after the thermal quench. A large fraction of the plasma current can be eventually converted to the current of the RE beam. When the thermal plasma current have decayed, the RE current remains, forming a plateau of the total plasma current.

Disruptions pose a threat to a tokamak for multiple reasons:

- The thermal energy released during the thermal quench may cause damage to the plasma facing components, in a manner similar to large ELMs.
- The magnetic energy is released during the current quench part as eddy currents in the conductive tokamak structures and part in radiation. During a VDE the plasma also touches the wall and part of the plasma poloidal current now must pass through the wall, known as *halo current*. The eddy currents and halo currents cause mechanical stresses in in-vessel components the support structure.
- When the runaway electron beam eventually hits the wall due to the loss of plasma equilibrium, its energy is deposited in a localized manner, which may cause damage to the plasma facing components of the wall.

The energies associated with disruptions are summarized in Table 9.1. For ITER they are much larger than for the present tokamaks, making ITER disruptions a serious concern.

	JET	ITER
thermal energy	< 12 MJ	< 350 MJ
poloidal magnetic energy	< 60 MJ	< 1300 MJ
RE current	1 MA	10 MA
energy of the RE beam	0.5 MJ	20 MJ

Table 9.1: Disruption parameters for JET and ITER. From [76]

9.2 Runaway electrons

The electron collision frequency decreases with their velocity v_e as $\nu \propto v_e^{-3}$ [77]. The drag on the moving electron caused by the collisions also decreases with v_e. When the electron is being accelerated by the electric field, above a certain critical velocity the drag drops below the accelerating electric force and the electron velocity increases more and more, eventually

to relativistic energies. Such electrons are called runaways. As the velocity can't overcome the speed of light, there is a critical electric field, below which runaway formation is prevented, as the critical velocity is above the speed of light.

The electrons can become runaways by several means which lead to obtaining a velocity above the critical value [78]: Dreicer, hot tail and avalanche mechanisms. The last one requires an existing runaway population which gets multiplied as the RE collide with thermal electrons and give them energies above the critical value. The initial RE population can be created by the first two mechanisms, in ITER Compton scattering by γ rays and decay of tritium will also contribute. The dominant mechanism of RE production in ITER disruptions will be the avalanche mechanism, leading to a multiplication of the original RE population by a factor of 2×10^{16} [79].

Runaways can be suppressed by increasing the density which increases the collision rate and thus the critical electric field. If the critical electric field is greater than the actual electric field, the REs are not produced. For the electric field of the ITER current quench the required electron density is above $10^{22}\,\mathrm{m}^{-3}$ [79], which requires injecting massive amounts of gas at the moment of disruption. This methods has technological problems, both with achieving such densities and with the impact on wall conditioning and the vacuum systems. An alternative mechanism of runaway suppression is thus desirable.

9.3 Runaway electron mitigation by magnetic perturbations

The runaway avalanche could be suppressed if the REs were lost from the plasma at a sufficient rate. One mechanism causing such a diffusion of runaways are magnetic perturbations [80]. If the trajectories of REs become chaotic as a result of the perturbations, the REs eventually hit the wall and can't induce further secondary REs, so the avalanche is supressed. This mechanism was first confirmed experimentally on JT-60U [81] and proposed as a solution for ITER in [82]. On TEXTOR the DED (dynamic ergodic divertor) was used to generate the magnetic perturbations and it was shown that the DED was able to suppress RE generation [83]. It was also shown by numerical simulations that the RE trajectories indeed become chaotic in the DED field.

9.4 Runaway electron mitigation experiments on JET

The magnetic perturbation technique was tested on JET using the perturbation field of the EFCCs. While initial results were uncertain [84], it was then found that this had been caused only by the scatter in the data [85] and further experiments have not shown any impact of the EFCCs on REs [76].

Another type of magnetic perturbation is the toroidal field variation (ripple), caused by the discrete nature of the toroidal field coils. Theoretical arguments show that RE trajectories can be influenced by the ripple [86]. JET has an unique ability of controlling the ripple, as its 32 toroidal field coils are divided in two independently powered sets of 16 coils alternating in the toroidal direction. The smallest ripple is produced if the same current is used in both sets and it increases with the difference between currents. RE control was attempted using the ripple introduced by this means. However the ripple is too weak for the theoretically envisaged mechanism to cause a diffusion of REs [76]. The experimental results are in agreement: no effect on REs was observed [76].

9.5 Simulations of runaway electron trajectories

9.5.1 Simulation setup

In order to explain the JET experimental results we performed simulations of the RE trajectories in the field of the JET EFCCs and the TF ripple. The REs were modelled as single test particles (without interactions with other particles) moving in the field of the EFCCs and the plasma. The total field was obtained as a superposition of those two. While this approach is questionable for the perturbations used to control ELMs due to the possible important influence of plasma response, here it is not supposed to be a problem, as the plasma resistivity after the thermal quench is high and its rotation and gradients are low.

The drift approximation was used and the relativistic drift equations of motion were obtained from the relativistic drift hamiltonian given in [87]. The same hamiltonian had been used by the TEXTOR team in [83]. We hovewer did not use the mapping approach used in [83] to avoid its complexity and we instead integrated the equations of motion of the gyrocenter using the standard Runge-Kutta scheme. The equations of motion and the integrator

were derived by R. Papřok [13]. The accuracy was checked by a comparison with trajectories obtained from a full hamiltonian (including the Larmor motion) and by checking the conservation of energy.

The simulations for the ripple field were done using only the full hamiltonian, as the drift hamiltonian [87] relies on a toroidally symmetric toroidal field, so it can't be applied in this situation. The time step had to be chosen significantly smaller than the Larmor period in order to represent accurately the Larmor motion.

The field of the EFCCs was calculated by the ERGOS code using the Biot-Savart's law. The toroidal field was assumed to have a perfect $1/R$ dependency in order to simplify the calculations. In the case of the toroidal field ripple the toroidal field was instead calculated by the Biot-Savart's law from the model of the toroidal coils kindly provided by D. Howell. The poloidal field was reconstructed by the EFIT code from a typical JET shot at a moment of a disruption. The poloidal field is the main source of uncertainity. The EFIT code, being intended for reconstructiong the plasma equilibrium, is not suited to the reconstruction of field during a disruption. Moreover it needs an assumption on the plasma current profile, which is not well known during a disruption. For this reason two different current profiles were chosen: one fairly flat, with a parabolic radial dependency of current density, another with a centrally peaked current density. The latter corresponds to the situation where most of the plasma current is already being carried by the RE beam. The differences in current profiles manifest themselves in the profiles of the safety factor q. The simulations were also done with an equilibrium corresponding to a moment before the thermal quench.

9.5.2 Results

The results are presented in the form of Poincaré plots, showing for each initial condition 2000 passages of the electron's gyrocenter through the poloidal plane. The initial positions are chosen on the oudboard midplane in a range from the magnetic axis outwards. The energies are in the range of RE energies in JET disruptions: 5 MeV, 10 MeV and 20 MeV.

The first studied configuration is all four EFCCs in a $n = 1$ configuration, that is, the current polarities and the radial perturbation field are arranged as $++--$ around the torus. The current of the EFCCs is 1.3 kA, or 20.8 kA turns. Results are shown in Figs 9.1–9.3.

The second configuration is $n = 1$, with only two opposite coils used, i.e. polarities are $+0-0$. The current is 2 kA, or 32 kA turns. Results are shown in Figs 9.4–9.6.

The third configuration is $n = 2$, with alternating currents of the coils in

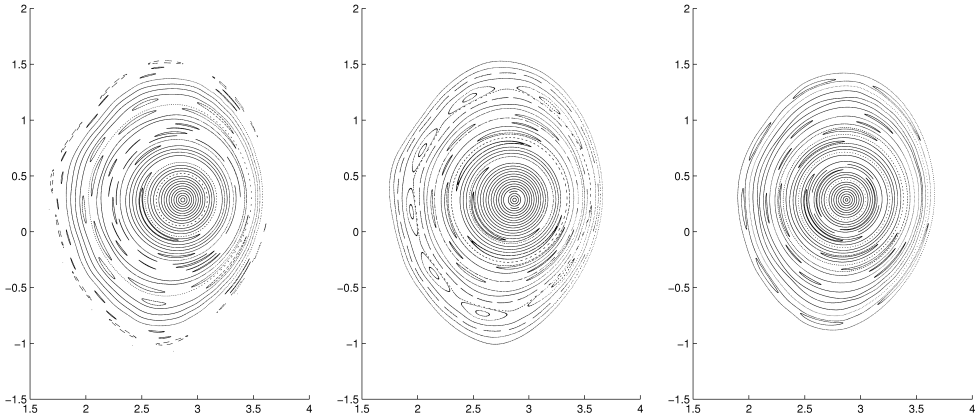

(a) 5 MeV (b) 10 MeV (c) 20 MeV

Figure 9.1: Poincaré plots of runaway trajectories (black) for the $n = 1$ configuration of all the four EFCCs, 1.3 kA current, peaked current equilibrium, JET shot #75352. Color lines are the flux surfaces of the equilibrium.

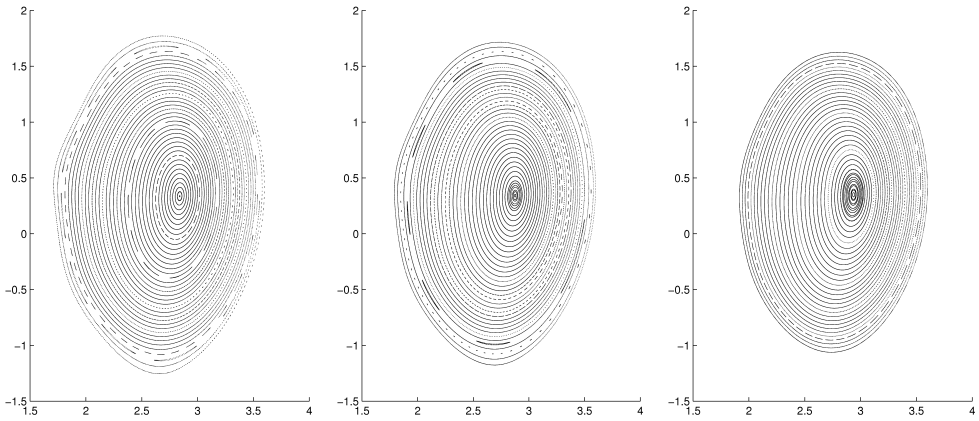

(a) 5 MeV (b) 10 MeV (c) 20 MeV

Figure 9.2: Poincaré plots for the parabolic current profile equilibrium of the shot #75352, other parameters are same as in Fig. 9.1.

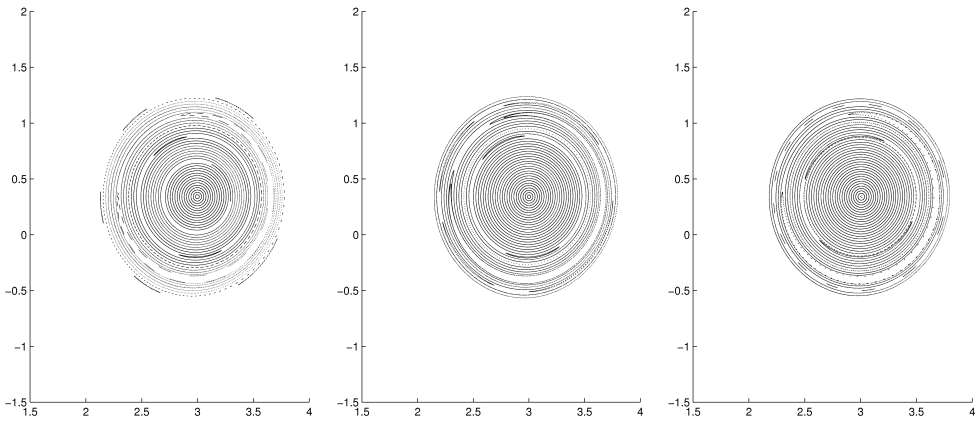

(a) 5 MeV (b) 10 MeV (c) 20 MeV

Figure 9.3: Poincaré plots for the pre-disruption equilibrium of the shot #75352, other parameters are same as in Fig. 9.1.

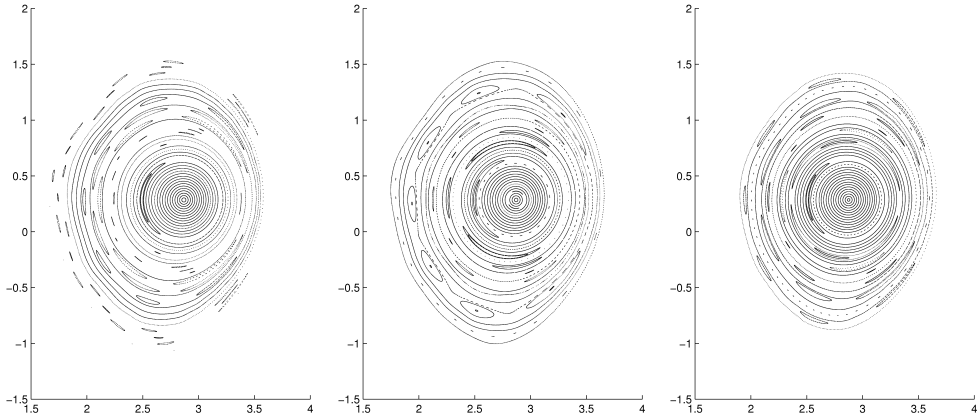

(a) 5 MeV (b) 10 MeV (c) 20 MeV

Figure 9.4: Poincaré plots of runaway trajectories for the $n = 1$ configuration of two EFCCs, 2 kA current, peaked current equilibrium, JET shot #75352.

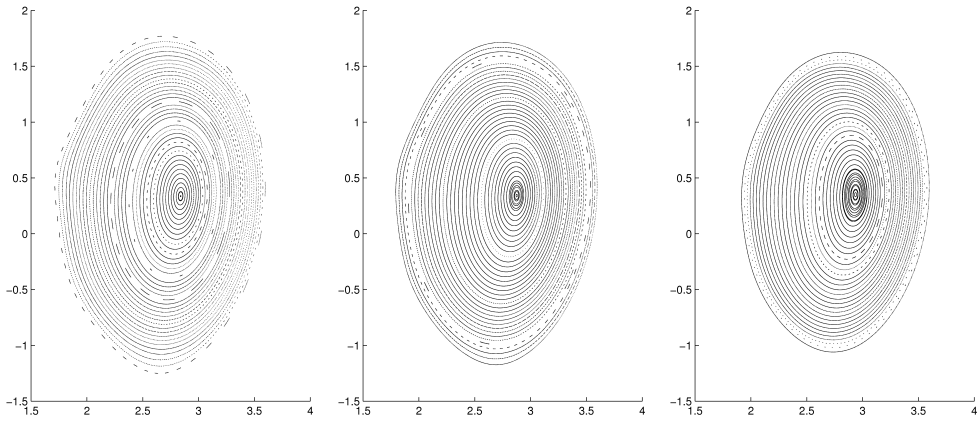

(a) 5 MeV (b) 10 MeV (c) 20 MeV

Figure 9.5: Poincaré plots for the parabolic current profile equilibrium of the shot #75352, other parameters are same as in Fig. 9.4.

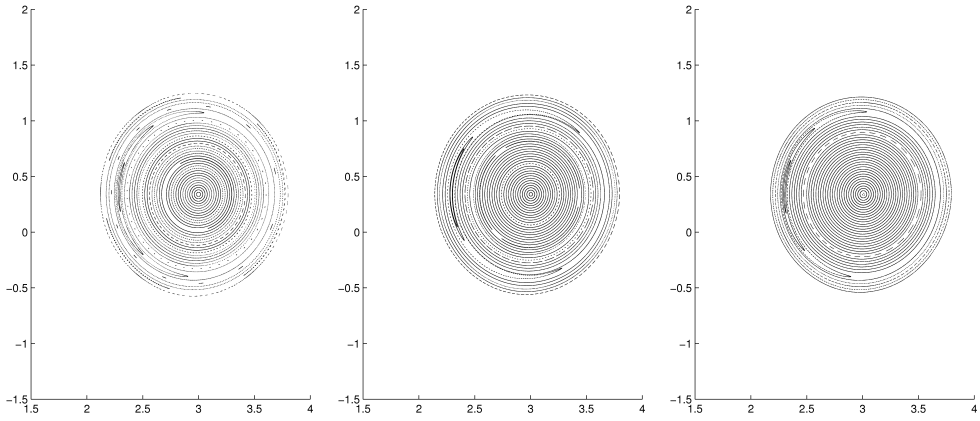

(a) 5 MeV (b) 10 MeV (c) 20 MeV

Figure 9.6: Poincaré plots for the pre-disruption equilibrium of the shot #75352, other parameters are same as in Fig. 9.4.

a $+-+-$ scheme. The current is 3 kA, or 48 kA turns. Results are shown in Figs 9.7–9.9.

Finally, we did a simulation with the ripple field, which was produced by a current of 63.6 kA in one set of toroidal field and 31.8 kA in the other, corresponding to a 1.2% outer midplane ripple. The results for the pre-disruption equilibrium are shown in Fig 9.10. For the other equilibria the results were very similar and are not shown.

9.5.3 Conclusions

All the Poincaré plots show regular KAM surfaces, sometimes alternating with island areas that are too narrow to overlap. No stochastic transport takes place. The equilibria are however very different. The peaked equilibrium has the most significant islands because its safety factor passes through the low-order rational numbers. In contrast, for the flat profile equilibrium, the q profile is high so high poloidal mode numbers m are needed for resonance. Those modes are weak in the spectrum of the EFCCs, because the EFCCs are large coils with a wide perturbation, dominated by low m modes in the Fourier space. The $n = 2$ perturbation requires for resonances poloidal modes with a twice as high m for the same q profile than the $n = 1$ perturbation. It is not surprising that the $n = 2$ results show lesser islands than the $n = 1$ results.

Those results explain the experimental observation that REs are not affected by EFCCs nor TF ripple on JET. We tried apparently the most favorable configuration $n = 1$ with the peaked equilibrium and increased the coil current in the simulation to a speculative[1] value of 6 kA, or 96 kA turns to see if this would be enough to produce the desired effect. Results are shown in Fig. 9.11. We can see that stochastic regions start to appear, however they don't yet merge in a global stochastic "sea" and good KAM surfaces persist especially in the center, where a realistic RE beam would be located. This degree of perturbation would still not be enough to cause RE losses by itself, but it may enhance runaway losses caused by other mechanism, such as the magnetic turbulence [88]. This mechanism has however reduced efficiency for the high RE energies considered, because the displacement of drift orbits of the REs relative to the flux surfaces causes the turbulence, if radially localized, to be averaged out on the RE orbit [88].

Installation of a new set of perturbation coils for ELM control on JET is currently being considered. Those coils would be located much closer to the

[1] This value will however be soon achievable thanks to the foreseen changes in the EFCC power supplies.

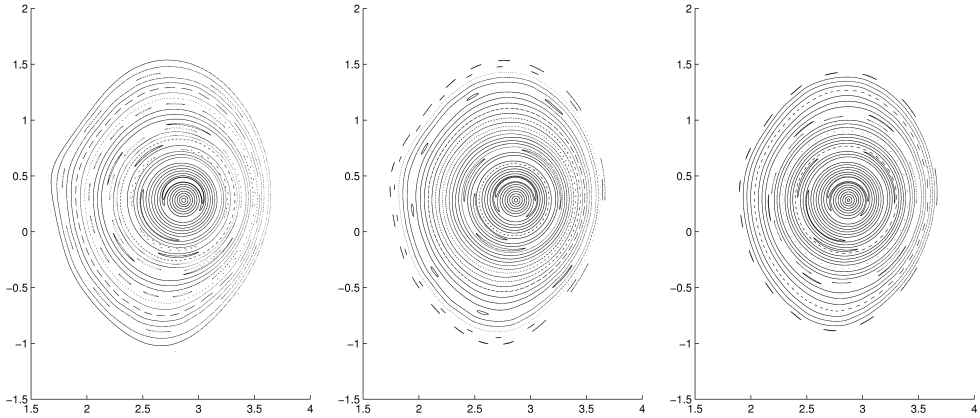

(a) 5 MeV (b) 10 MeV (c) 20 MeV

Figure 9.7: Poincaré plots of runaway trajectories for the $n = 2$ configuration of four EFCCs, 3 kA current, peaked current equilibrium, JET shot #75352.

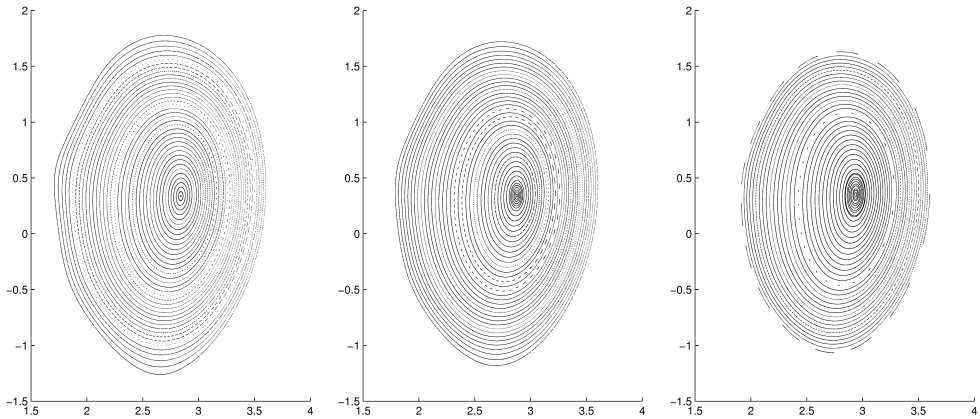

(a) 5 MeV (b) 10 MeV (c) 20 MeV

Figure 9.8: Poincaré plots for the parabolic current profile equilibrium of the shot #75352, other parameters are same as in Fig. 9.7.

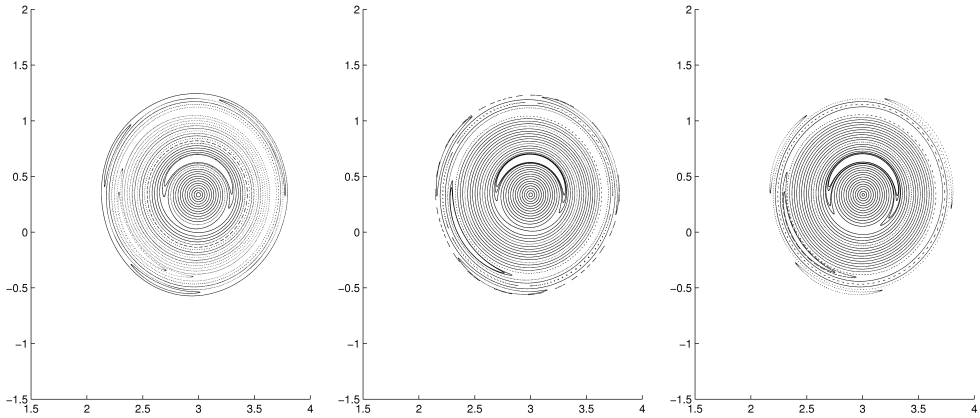

(a) 5 MeV (b) 10 MeV (c) 20 MeV

Figure 9.9: Poincaré plots for the pre-disruption equilibrium of the shot #75352, other parameters are same as in Fig. 9.7.

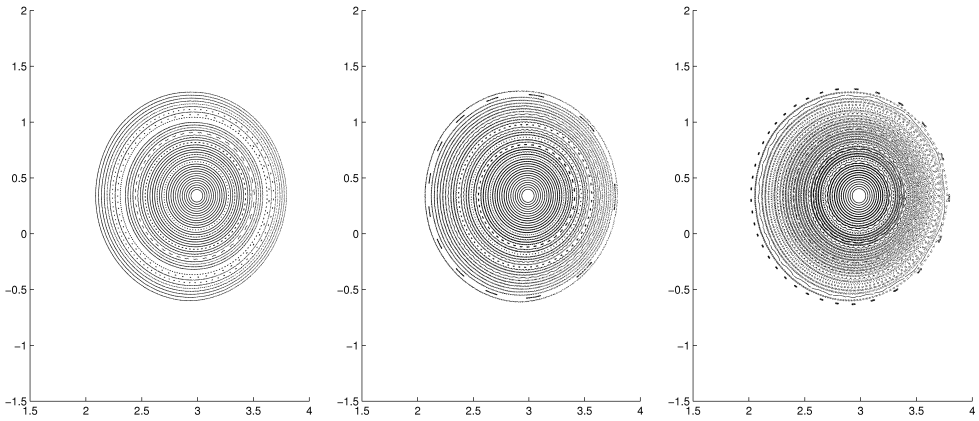

(a) 5 MeV (b) 10 MeV (c) 20 MeV

Figure 9.10: Poincaré plots of runaway trajectories for the toroidal field ripple, pre-disruption equilibrium, JET shot #75352.

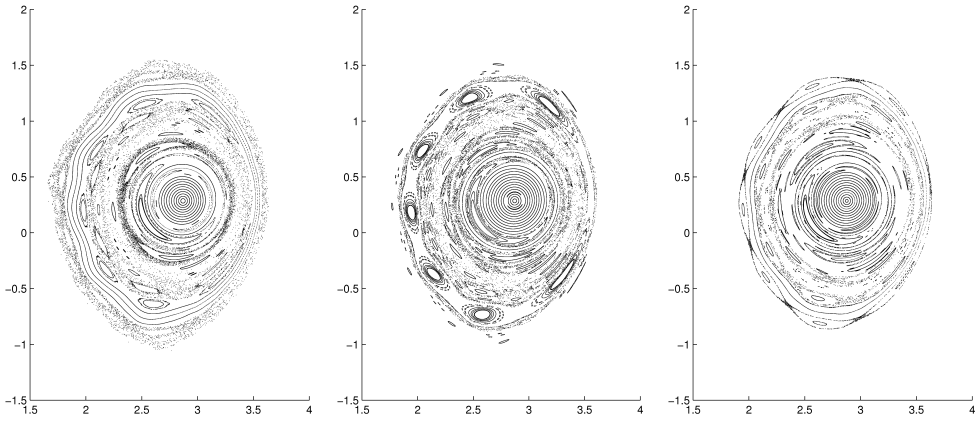

(a) 5 MeV (b) 10 MeV (c) 20 MeV

Figure 9.11: Poincaré plots for the peaked current equilibrium of the shot #75352, with a $n = 1$ configuration of all the four EFCCs and a speculative current of 6 kA.

plasma and be much smaller, thus being able to produce higher m modes. A priori such coils may be better suited for RE mitigation than the existing EFCCs. Our calculation shall be repeated for this coil design to check if it is indeed the case. Eventually, such calculations need to be done also for ITER with the planned ELM control coils which may find a second use as a tool for RE control.

Chapter 10

Conclusions

The study of resonant magnetic perturbations in tokamaks is an exceptional topic. It combines the mathematics of the dynamical systems with diverse physical phenomena ranging from single particle motion to magnetohydrodynamics, and at the same time presents important opportunities for applications. It is unique in the way how the abstract mathematical notions, formulated in the geometry of the phase space, translate very directly to observable physical quantities. Indeed, the phase space of the hamiltonian formulation of field lines is here the physical space inside the tokamak and many of the abstract structures that we know from figures in the mathematical textbooks can be directly observed with the tokamak diagnostics, even seen on cameras.

The present thesis has touched many topics of this field. The most important achievements according to the author's opinion are:

- The comparison of chaotic behavior of field lines and particle trajectories have yielded interesting results and the work has continued in the calculations of trajectories of runaway electrons in the JET tokamak. The chaotic behavior is actually absent in this case, the important point is that this result is in agreement with experimental observations. Other groups predicted chaotic behavior for other cases (e.g. TEXTOR) and this was also backed by experiments, so we may suppose that this modelling is the right approach and we may use it for evaluating future coil designs.

- Establishing of a solid basis for the COMPASS experiments with RMPs. The availability of the RMP coils, the X-point geometry, ability to enter H-mode, neutral beam injection, and diagnostics focused on the edge (together with the rich magnetic diagnostics) make COMPASS a

suitable machine for RMP studies. Conducting the COMPASS experiments will be one of our next major tasks.

- The experience gained with optimizing the RMP spectra has lead to formulation and publication of design guidelines for RMP coils which find use in the design of other future experiments.

- We have rigorously formulated the correlation of magnetic islands at different surfaces and magnetic footprints. A model for the screening currents in the plasma has been developed and it was found that screening reduces the footprints substantially, presenting an interesting research opportunity, among others for COMPASS. The model of screening can be used to implement the screening predicted by cylindrical plasma response models in a realistic geometry. Example uses that we foresee are:

  - calculations of the neoclassical toroidal viscosity,
  - transport simulations in the screened perturbation field.

  The second topic will be another major area of future research, as it can give more concrete results for comparison with experiments.

Last but not least, it is the author's hope that the present thesis will serve as an useful reference for future students of this topic.

Appendix A

Integrability of hamiltonian dynamical systems

This appendix summarizes the needed results of classical mechanics and chaos theory of hamiltonian dynamical systems. It follows mostly the monographs [89, 38, 90].

A.1 Basic notions

A hamiltonian system with n degrees of freedom is described by n pairs of variables (p_i, q_i) and hamiltonian function H. Its dynamics is given by the canonical equations

$$\frac{\mathrm{d}q_i}{\mathrm{d}t} = \frac{\partial H}{\partial p_i} \tag{A.1}$$

$$\frac{\mathrm{d}p_i}{\mathrm{d}t} = -\frac{\partial H}{\partial q_i} \tag{A.2}$$

If the hamiltonian is time-independent, it is a conserved quantity (an *integral of motion*) and is called *autonomous*.

If the system has n integrals of motion $F_1, \ldots, F_n$ (one of them is the hamiltonian H) which satisfy the condition of having zero Poisson brackets

$$\{F_i, F_j\} = 0$$

(we say that the functions $F_1, \ldots, F_n$ are *in involution*), one may perform a canonical transformation into new momenta I_i and positions θ_i, where the I_i are functions of $F_1, \ldots, F_n$ only and so are also integrals of motion. The hamiltonian depends only on I_i. The variables θ_i are called *angles* and I_i

actions. Canonical equations for those variables have a simple form

$$\frac{\mathrm{d}\theta_i}{\mathrm{d}t} = \frac{\partial H}{\partial I_i} \equiv \omega_i(I_1, \ldots, I_n) \tag{A.3}$$

$$\frac{\mathrm{d}I_i}{\mathrm{d}t} = -\frac{\partial H}{\partial q_i} = 0. \tag{A.4}$$

This is the Liouville-Arnold theorem whose proof can be found in [89]. Systems with this property are called *integrable* and their time evolution is simple: the values of actions I_i stay constant and define a n-dimensional hypersurface on which the trajectory of the system remains. The angles θ_i evolve independently on each other with constant velocities ω_i which depend on the choice of the hypersurface. As we assume that the system is constrained to remain in a bounded area of the phase space, the positions θ_i are angular coordinates: $\theta_i + 2\pi$ describe the same point as θ_i. The hypersurfaces of constant actions have thus the topology of a torus (a Cartesian product of n circles, each of them parametrized by one of the coordinates θ_i) and they are called *invariant tori*.

Autonomous systems with one degree of freedom are always integrable, because one integral of motion is sufficient, and this is the hamiltonian. Systems with more degrees of freedom or a time-dependent hamiltonian are not necessarily integrable. The case of a time-dependent hamiltonian can be reduced to an autonomous one with one added degree of freedom by the following procedure. To the original variables (p_i, q_i) we add a pair of canonical variables $-E$ and t (t is the time in the original nonautonomous system) and we introduce a new hamiltonian $\bar{H}(p_i, q_i, -E, t) \equiv H(p_i, q_i, t) - E$ and a new time variable τ. The canonical equations on the *extended phase space* $(p_i, q_i, -E, t)$ are then

$$\frac{\mathrm{d}q_i}{\mathrm{d}\tau} = \frac{\partial \bar{H}}{\partial p_i} = \frac{\partial H}{\partial p_i} \tag{A.5}$$

$$\frac{\mathrm{d}p_i}{\mathrm{d}\tau} = -\frac{\partial \bar{H}}{\partial q_i} = -\frac{\partial H}{\partial q_i} \tag{A.6}$$

$$\frac{\mathrm{d}t}{\mathrm{d}\tau} = -\frac{\partial \bar{H}}{\partial (-E)} = 1 \tag{A.7}$$

$$\frac{\mathrm{d}(-E)}{\mathrm{d}\tau} = -\frac{\partial \bar{H}}{\partial t} = -\frac{\partial H}{\partial t} \tag{A.8}$$

According to the equation (A.7) the time τ of the new system is identical to the time t of the old system up to an additive constant. The equations (A.5) and (A.6) are then equivalent to the equations (A.1) and (A.2) of the

old system and the equation (A.8) expresses that E is equal to the energy H of the new system. (In the new system t and $-E$ are however formally independent variables.) The new system is thus completely equivalent to the old one. The new hamiltonian $\bar{H}$ is an integral of motion, as it does not explicitly depend on the new time variable τ. We can thus without loss of generality restrict ourselves to the study of autonomous systems.

A.2 Weakly nonintegrable systems

Weakly nonintegrable systems are those with a hamiltonian which differs from an integrable one $H_0(\vec{\mathbf{I}})$ by a nonintegrable part, considered as a small perturbation. In the action-angle variables the hamiltonian has the form

$$\frac{\mathrm{d}\theta_i}{\mathrm{d}t} = \frac{\partial H_0(\vec{\mathbf{I}})}{\partial I_i} + L\frac{\partial H_1(\vec{\mathbf{I}},\vec{\theta})}{\partial I_i} \tag{A.9}$$

$$\frac{\mathrm{d}I_i}{\mathrm{d}t} = -L\frac{\partial H_1(\vec{\mathbf{I}},\vec{\theta})}{\partial \theta_i} \tag{A.10}$$

L is a parameter determining the amplitude of the nonintegrable perturbation. The reason for nonintegrability is the dependence of the perturbation on angles $\vec{\theta}$.

We will now study the case of an autonomous system with two degrees of freedom. This case may arise as an equivalent formulation of the case of one degree of freedom and a time-dependent hamiltonian of the form

$$H(I,\theta,t) = H_0(I) + LH_1(I,\theta,t) \tag{A.11}$$

where is again separated the integrable part H_0 and the nonintegrable perturbation LH_1. As this system is close to one with one degree of freedom, it is sometimes called "system with $1\frac{1}{2}$ degrees of freedom".

Let us return to the formalism where the system is considered as autonomous with two degrees of freedom. We may write the perturbation H_1 in the form of a Fourier series in angles $\vec{\theta} = (\theta_1, \theta_2)$:

$$H_1(\vec{\mathbf{I}},\vec{\theta}) = \sum_{l_1,l_2} \widehat{H}_{1\vec{\mathbf{l}}} e^{2\pi\vec{\mathbf{l}}\cdot\vec{\theta}} \tag{A.12}$$

$\vec{\mathbf{l}} = (l_1, l_2)$ is a pair of integers.

H is still an integral of motion, so the motion is restricted onto a surface of constant H — *energy surface*. The question now is if the motion on this surface is qualitatively different from the integrable case where the surface is further divided by the invariant tori of a lower dimension onto which the motion is restricted.

A.2.1 One perturbation mode

We shall first investigate the case where the series (A.12) has only two complex conjugate (in order to have a real sum) terms, so $H_1(\vec{\mathbf{I}}, \vec{\theta}) = 2\widehat{H}_{1\vec{\mathbf{I}}}(\vec{\mathbf{I}}) \cos(l_1\theta_1 + l_2\theta_2)$. We may perform a canonical transformation into new (primed) variables using a generating function

$$W(\vec{\theta}, \vec{\mathbf{I}}') = (l_1\theta_1 + l_2\theta_2)I_1' + \theta_2 I_2'$$

The new angles are given by the following relations:

$$\theta_1' = \frac{\partial W}{\partial I_1'} = l_1\theta_1 + l_2\theta_2 \tag{A.13}$$

$$\theta_2' = \frac{\partial W}{\partial I_2'} = \theta_2 \tag{A.14}$$

and the new actions are in a similar way linear combinations of the old actions. The hamiltonian is then not a function of θ_2', only of θ_1':

$$H_1(\vec{\mathbf{I}}', \vec{\theta}') = 2\widehat{H}_{1\vec{\mathbf{I}}}(\vec{\mathbf{I}}') \cos\theta_1' \tag{A.15}$$

Thanks to θ_2' being a cyclical coordinate and I_2' an integral of motion this pair of variables can be eliminated. The system is thus effectively a system with one degree of freedom, which is integrable.

The influence of the perturbation is most important when it is constant on a trajectory — the frequencies are in a resonance with the perturbation. This happens when the expression $\vec{\mathbf{l}} \cdot \vec{\theta} = l_1\theta_1 + l_2\theta_2 = \theta_1'$ is constant. For the unperturbed system this would occur when the condition $l_1\omega_1 + l_2\omega_2 = 0$ is satisfied (for a general number of degrees of freedom $\vec{\mathbf{l}} \cdot \vec{\omega} = 0$). Let us note the value of $\vec{\mathbf{I}}'$ in corresponding to the resonance as $\vec{\mathbf{I}}_0'$ (with components I_{10}', I_{20}') and the difference from I_{10}' as p, i.e. $I_1' = I_{10}' + p$. The hamiltonian expanded to second order around $\vec{\mathbf{I}}_0'$ has the form

$$H(\vec{\mathbf{I}}', \vec{\theta}') = H_0(\vec{\mathbf{I}}') + \left.\frac{\partial H}{\partial I_1'}\right|_{\vec{\mathbf{I}}_0'} p + \frac{1}{2}\left.\frac{\partial^2 H_0}{\partial {I_1'}^2}\right|_{\vec{\mathbf{I}}_0'} p^2 + 2L\widehat{H}_{1\vec{\mathbf{I}}}(\vec{\mathbf{I}}_0') \cos\theta_1' \tag{A.16}$$

The second partial derivative of H_1 has been neglected in the second order approximation, as it is multiplied by L, which is itself small. $\left.\frac{\partial H}{\partial I_1'}\right|_{\vec{\mathbf{I}}_0'}$ is the time derivative of θ_1' which is zero by assumption (this is the resonance condition). The remaining terms are the one quadratic in p and the perturbation term, which together form a hamiltonian analogous to the one of a pendulum:

$$H(\vec{\mathbf{I}}', \vec{\theta}') = H_0(\vec{\mathbf{I}}_0') + \frac{1}{2}\left.\frac{\partial^2 H_0}{\partial {I_1'}^2}\right|_{\vec{\mathbf{I}}_0'} p^2 + 2L\widehat{H}_{1\vec{\mathbf{I}}}(\vec{\mathbf{I}}_0') \cos\theta_1' \tag{A.17}$$

The system thus can be, analogously to the pendulum, in three regimes: rotation, libration and the limit case of separatrix motion. Of special significance are the fixed points, i.e. the constant values of variables I_1' and θ_1'. They are the solutions of equations

$$\begin{aligned} 0 &= \frac{\mathrm{d}\theta_1'}{\mathrm{d}t} = \frac{\partial H}{\partial I_1'} \\ &= \frac{\partial H_0}{\partial I_1'} + 2L\frac{\partial \widehat{H}_{1\vec{\mathrm{I}}}}{\partial I_1'}\cos\theta_1' \qquad \text{(A.18)} \\ 0 &= \frac{\mathrm{d}I_1'}{\mathrm{d}t} = -\frac{\partial H}{\partial \theta_1'} \\ &= 2L\widehat{H}_{1\vec{\mathrm{I}}}\sin\theta_1', \qquad \text{(A.19)} \end{aligned}$$

the equation (A.19) has solutions $\theta_1' = 0, \pi \pmod{2\pi}$. One solution is the elliptic fixed point, or *O-point*, around which the phase trajectories have the form of ellipses — it corresponds to the case of small amplitude of a pendulum. The second solution is a hyperbolic fixed point, or *X-point*, where the separatrices cross and around which the trajectories deviate hyperbolically — it corresponds to the upper unstable equilibrium position of a pendulum. We can distinguish them by linearizing the equations (A.18), (A.19) at the vicinity of the fixed point. The linearized right hand sides can be considered as one linear vector map. If its eigenvalues are two complex conjugate numbers, the fixed point is elliptic. If they are two real numbers, it is hyperbolic and the eigenvectors are tangent to the incoming and outgoing separatrices.

For the values of action far from the resonance the rotation regime is similar to the unperturbed trajectories — the invariant tori are only weakly affected by the perturbation. Qualitatively, as the variable θ_1' is changing fast (the system is far from the resonance where θ_1' changes slowly), it is possible to average the perturbation (A.17) over this variable. The hamiltonian is then equal to the unperturbed one — the average of the perturbation is zero.

A.2.2 General perturbation

A general perturbation (A.12) is a sum of terms, which must form complex conjugate pairs in order to have a real result. It is thus a sum of the perturbations from the previous subsection for different values of $\vec{\mathrm{I}}$. To every $\vec{\mathrm{I}}$ corresponds a value of the resonant frequencies $\vec{\omega}$. If those resonances are sufficiently far away from each other, we may apply the foregoing method for every resonance separately, as we have seen that a perturbation mode can be eliminated by averaging far away from its resonance. If we draw in a cross-section through the phase space for constant θ_2 and I_2 the passages of

the trajectory through this plane (parametrized by θ_1 and I_1) will show as chains of "islands". Every chain is formed by alternating elliptic and hyperbolic fixed points and the separatrix between them. The number of islands in a chain is equal to the number l_1 from the equation (A.13) because in the coordinates (I_1', θ_1') the island is only one. Such a section through the phase space is an example of *Poincaré section*.

Every island chain is to some extent influenced by other modes of the perturbation. The separatrix is the most sensitive. In the exact case of a simple pendulum (corresponding to one perturbation mode), the separatrix is formed by trajectories leaving the unstable fixed point (i.e. asymptotically approaching it when followed backwards in time) and trajectories approaching this fixed point. The first set of trajectories forms a surface called the *unstable manifold* of the fixed point, while the latter forms the *stable manifold* of the fixed point[1]. When the pendulum motion is perturbed (by adding a second mode of the perturbation), those manifolds do not coincide anymore to form a separatrix, but intersect each other in a complicated pattern, called the *homoclinic tangle*. The homoclinic tangle guides the trajectories, because they can not cross the invariant manifolds (as trajectories can not cross each other). It can be proven [90] that the motion in the tangle is *chaotic*, meaning that it is sensitive to initial conditions (a small difference in initial conditions exponentially increases). In this way a chaotic layer around the original separatrix forms. (Sometimes it is interchangeably called *stochastic* or *ergodic* although strictly speaking those words are not synonymous.)

A.2.3 The fate of invariant tori

If the values of actions are such that the system is far from resonances, then averaging over the fast varying angles we reach the conclusion that the dynamics should not be much different from the integrable case. This statement is rigorously formulated in the *KAM theorem*. This theorem states that the invariant tori (which in the unperturbed system correspond to the conserved actions) remain even in the weakly nonintegrable system (for sufficiently weak perturbation) and are only deformed by the perturbation. Those tori present impermeable barriers for the trajectories in the phase space[2], so they sepa-

[1] Both are examples of *invariant manifolds* formed by trajectories. Invariant manifolds are called so because, consisting of trajectories, they are invariant under the time evolution of the system. A basic example are the invariant tori (section A.1).

[2] This is valid for two degrees of freedom, where the phase space has dimension four, the hypersurface of constant energy has the dimension three and two-dimensional tori partition it into disconnected regions. For more degrees of freedom even the presence of invariant tori does not prevent large changes of the values of actions — this is called

rate the regions where the condition of sufficient distance from resonances is not satisfied and a stochastic layer is formed.

A simple criterion for the disappearance of the last KAM torus separating two island chains was given by Chirikov. It says that the torus exists if the width of those chains is such that they do not overlap. In the opposite case the stochastic layers around the islands merge in a large stochastic region — the transition to global stochasticity occurs. If the dynamics near resonances is approximated by the one of a pendulum, the width of the island and thus the transition to global stochasticity can be estimated analytically.

The Chirikov criterion can be precised by considering the finite width of the stochastic layer, which is moreover enhanced by island chains around secondary resonances.

When the perturbation is strong enough to have destroyed the last KAM torus, this torus is replaced by a discrete set of invariant points. It has a structure of the Cantor set and is called *Cantorus*. Cantorus is a partial obstacle for trajectories — thanks to its discontinuity they can cross it, but their diffusion is slowed.

A.2.4 Poincaré map

If we make a section through the phase space defined as a surface of constant value of one of the angle variables (let it be $\theta_2 = 0$), the result will be a hypersurface of dimension $2n - 1$. By using one value of energy one may eliminate another variable, e.g. I_2, as its value is determined by the energy and the values of other variables. The resulting hypersurface of dimension $2n - 2$ is parametrized by variables $I_1, \theta_1, I_3, \theta_3, \ldots, I_n, \theta_n$ and is called a Poincaré section. Phase trajectories periodically pass through it and their intersections with it are isolated points. The map which to any point in this section with the value $\theta_2 = 0$ assigns the following intersection of the trajectory with the section, i.e. with $\theta_2 = 2\pi$, is called the Poincaré map. The evolution of the system is then described by iterations of this map, which generate further and further points in the section for the chosen trajectory.

The advantage of the Poincaré map is an easy visualization. For a system with two degrees of freedom the Poincaré section is two-dimensional and can be easily plotted. If the system originated as a system with one degree of freedom and a time-dependent hamiltonian, it is practical to choose as the coordinate θ_2 the one which corresponds to the time t of the original system. Then the coordinates of the Poincaré section are the canonical coordinates of the original system and the Poincaré section represents the state of the

Arnold diffusion.

system at given time instants.

If the system is integrable, every trajectory remains on an invariant torus. The intersection of this torus with the surface of section is a torus of lower dimension, for a two-dimensional torus a circle. For a chosen initial point its images under the Poincaré map after a sufficient number of iterations draw this circle. In a similar way the KAM tori in the weakly nonintegrable case will show as more or less deformed curves (topological circles). On the other hand, if the initial point lies in a stochastic region, by iterations of the Poincaré map we obtain points densely filling a certain area. This way one can by plotting the Poincaré section for suitable initial conditions and a sufficient number of iterations find the stochastic regions and KAM tori.

The decomposition of the perturbation in harmonic components determines for weakly nonintegrable systems the shape of a Poincaré plot. On the section we will find island chains for every resonance, as described in the section A.2.2. These are for a sufficiently weak perturbation separated by curves corresponding to the KAM tori.

Author's Bibliography

[1] Cahyna, P. and Krlin, L. *Full hamiltonian description of the interaction of particles with magnetic islands in tokamak*. Czechoslovak Journal of Physics, **56**, 367 (2006).

[2] Krlin, L. and Cahyna, P. *Particle diffusion in a system of magnetic islands in tokamaks in fully hamiltonian approach*. Czechoslovak Journal of Physics, **56**, B111 (2006).

[3] Cahyna, P., Krlin, L., Panek, R., and Kurian, M. *Interaction of particles with systems of magnetic islands and edge turbulence in tokamaks in fully hamiltonian approach*. In *Proceedings of the 34th EPS Conference on Plasma Physics*, vol. 31F of *Europhysics Conference Abstracts*, pp. P–4.044. 2007.

[4] Cahyna, P., Panek, R., Fuchs, V., Krlin, L., Becoulet, M., and Nardon, E. *Field ergodization by external coils on the COMPASS tokamak*. In *WDS'07 Proceedings of Contributed Papers: Part II - Physics of Plasmas and Ionized Media* (edited by Safrankova, J. and Pavlu, J.), pp. 240–245. Matfyzpress, Prague, 2007.

[5] Cahyna, P., Bécoulet, M., Pánek, R., Fuchs, V., Nardon, E., and Krlin, L. *Resonant magnetic perturbations and edge ergodization on the COMPASS tokamak*. Plasma Physics Reports, **34**, 746 (2008).

[6] Shaing, K. C., Cahyna, P., Becoulet, M., Park, J.-K., Sabbagh, S. A., and Chu, M. S. *Collisional boundary layer analysis for neoclassical toroidal plasma viscosity in tokamaks*. Physics of Plasmas, **15**, 082506 (2008).

[7] Shaing, K. C., Sabbagh, S. A., Chu, M. S., Becoulet, M., and Cahyna, P. *Effects of orbit squeezing on neoclassical toroidal plasma viscosity in tokamaks*. Physics of Plasmas, **15**, 082505 (2008).

[8] Becoulet, M., Huysmans, G., Garbet, X., Nardon, E., Howell, D., Garofalo, A., Schaffer, M., Evans, T., Shaing, K., Cole, A., Park, J.-K., and Cahyna, P. *Physics of penetration of resonant magnetic perturbations used for Type I edge localized modes suppression in tokamaks*. Nuclear Fusion, **49**, 085011 (2009).

[9] Cahyna, P., Panek, R., Fuchs, V., Krlin, L., Becoulet, M., Huysmans, G., and Nardon, E. *The optimization of resonant magnetic perturbation spectra for the COMPASS tokamak*. Nuclear Fusion, **49**, 055024 (2009).

[10] Nardon, E., Kirk, A., Akers, R., Becoulet, M., Cahyna, P., Temmerman, G. D., Dudson, B., Hnat, B., Liu, Y. Q., Martin, R., Meyer, H., Tamain, P., Taylor, D., Temple, D., and the MAST Team. *Edge localized mode control experiments on MAST using resonant magnetic perturbations from in-vessel coils*. Plasma Physics and Controlled Fusion, **51**, 124010 (2009).

[11] Nardon, E., Kirk, A., Ayed, N. B., Bécoulet, M., Cahyna, P., Evans, T., Huysmans, G., Koslowski, H., Liang, Y., Saarelma, S., and Thomas, P. *ELM control by resonant magnetic perturbations on JET and MAST*. Journal of Nuclear Materials, **390-391**, 773 (2009). Proceedings of the 18th International Conference on Plasma-Surface Interactions in Controlled Fusion Device.

[12] Panek, R., Cahyna, P., Dejarnac, R., Fuchs, V., Havlicek, J., Horacek, J., Hron, M., Hronova, O., Janky, F., Mlynar, J., Stockel, J., Urban, J., Weinzettl, V., Zajac, J., and Zacek, F. *Status of the COMPASS tokamak reinstallation in Institute of Plasma Physics AS CR*. In *Proceedings of the 36th EPS Conference on Plasma Physics*, vol. 33E of *Europhysics Conference Abstracts*, pp. P–5.140. 2009.

[13] Paprok, R., Krlin, L., Cahyna, P., and Riccardo, V. *Motion of charged particles in perturbed magnetic fields of tokamak*. In *WDS'09 Proceedings of Contributed Papers: Part II - Physics of Plasmas and Ionized Media* (edited by Safrankova, J. and Pavlu, J.), pp. 139–143. Matfyzpress, Prague, 2009.

[14] Cahyna, P. and Nardon, E. *Resonant magnetic perturbations and divertor footprints in poloidally diverted tokamaks* (2010). `arXiv:1005.3663[physics.plasm-ph]`.

[15] Cahyna, P., Nardon, E., and JET EFDA contributors. *Model for screening of resonant magnetic perturbations by plasma in a realistic tokamak*

geometry and its impact on divertor strike points (2010). Submitted to Proceedings of the 19th International Conference on Plasma-Surface Interactions, to be published in Journal of Nuclear Materials.

[16] Duarte, A., Santos, B., Pereira, T., Carvalho, B., Fernandes, H., Neto, A., Janky, F., Cahyna, P., Písacka, J., and Hron, M. *FireSignal application node for subsystem control*. Fusion Engineering and Design, **85**, 496 (2010). Proceedings of the 7th IAEA Technical Meeting on Control, Data Acquisition, and Remote Participation for Fusion Research.

[17] Havlicek, J., Kudlacek, O., Janky, F., Horacek, J., Beno, R., Valcarcel, D., Fixa, J., Brotankova, J., Zajac, J., Hron, M., Panek, R., and Cahyna, P. *Status of magnetic diagnostics on COMPASS*. In *WDS'10 Proceedings of Contributed Papers: Part II - Physics of Plasmas and Ionized Media* (edited by Safrankova, J. and Pavlu, J.). Matfyzpress, Prague, 2010. To be published.

[18] Nardon, E., Cahyna, P., Devaux, S., Kirk, A., Alfier, A., Luna, E. D. L., Temmerman, G. D., Denner, P., Eich, T., Gerbaud, T., Harting, D., Jachmich, S., Koslowski, H., Liang, Y., Sun, Y., the MAST team, and JET EFDA contributors. *Strike-point splitting induced by external magnetic perturbations: observations on JET and MAST and associated modelling* (2010). Submitted to Proceedings of the 19th International Conference on Plasma-Surface Interactions, to be published in Journal of Nuclear Materials.

[19] Riccardo, V., Arnoux, G., Cahyna, P., Hender, T., Huber, A., Jachmich, S., Kiptily, V., Koslowski, R., Krlin, L., Lehnen, M., Loarte, A., Nardon, E., Paprok, R., Tskhakaya, D., and JET EFDA contributors. *JET disruption studies in support of ITER* (2010). Accepted in Plasma Physics and Controlled Fusion.

[20] Valcarcel, D., Duarte, A., Neto, A., Carvalho, I., Carvalho, B., Fernandes, H., Sousa, J., Sartori, F., Janky, F., Cahyna, P., Hron, M., and Panek, R. *Real-time software for the COMPASS tokamak plasma control*. Fusion Engineering and Design, **85**, 470 (2010). Proceedings of the 7th IAEA Technical Meeting on Control, Data Acquisition, and Remote Participation for Fusion Research.

Bibliography

[21] Freidberg, J. *Plasma physics and fusion energy*. Cambridge university press, 2007.

[22] Helander, P. and Sigmar, D. J. *Collisional transport in magnetized plasmas*. Cambridge university press, 2002.

[23] Wesson. *Tokamaks*. Clarendon, Oxford, 2004, 3 edn.

[24] Abdullaev, S. S. and Zaslavsky, G. M. Phys. Plasmas, **3**, 516 (1996).

[25] Park, J., Boozer, A. H., and Menard, J. E. Phys. Plasmas, **15**, 064501 (2008).

[26] Grimm, R. C., Dewar, R. L., and Manickam, J. J. Comput. Phys., **49**, 94 (1983).

[27] Freidberg, J. P. *Ideal magnetohydrodynamics*. Plenum Press, 1987.

[28] Wagner, F. Plasma Physics and Controlled Fusion, **49**, B1 (2007).

[29] Connor, J. W. and Wilson, H. R. Plasma Physics and Controlled Fusion, **42**, R1 (2000).

[30] Connor, J. W. Plasma Physics and Controlled Fusion, **40**, 191 (1998).

[31] Suttrop, W. Plasma Physics and Controlled Fusion, **42**, A1 (2000).

[32] Kirk, A., et al. Phys. Rev. Lett., **92**, 245002 (2004).

[33] Loarte, A., et al. Plasma Phys. Controlled Fusion, **45**, 1549 (2003).

[34] ITER Physics Basis Editors, et al. Nuclear Fusion, **39**, 2137 (1999).

[35] Shimada, M., et al. Nuclear Fusion, **47**, S1 (2007).

[36] Hawryluk, R., et al. Nuclear Fusion, **49**, 065012 (2009).

[37] Thomas, P. R. In *Fusion Energy 2008 (Proc. 22nd Int. Conf. Geneva)*. (Vienna: IAEA), 2008. CD-ROM file IT/1-5 and http://www-naweb.iaea.org/napc/physics/FEC/FEC2008/html/index.htm.

[38] Lichtenberg, A. and Lieberman, M. *Regular and stochastic motion*, vol. 38 of *Applied Mathematical Sciences*. Springer-Verlag, New York, Heidelberg, Berlin, 1983.

[39] Samain, A., Grosman, A., and Feneberg, W. Journal of Nuclear Materials, **111-112**, 408 (1982).

[40] Ghendrih, P., et al. Nuclear Fusion, **42**, 1221 (2002).

[41] Grosman, A., et al. Plasma Physics and Controlled Fusion, **32**, 1011 (1990).

[42] Payan, J., et al. Nuclear Fusion, **35**, 1357 (1995).

[43] Rechester, A. B. and Rosenbluth, M. N. Phys. Rev. Lett., **40**, 38 (1978).

[44] Unterberg, B., et al. Journal of Nuclear Materials, **363-365**, 698 (2007). Plasma-Surface Interactions-17.

[45] Joseph, I., et al. Nucl. Fusion, **48**, 045009 (2008).

[46] Shoji, T., et al. Journal of Nuclear Materials, **196-198**, 296 (1992).

[47] Tamai, H., et al. Journal of Nuclear Materials, **220-222**, 365 (1995).

[48] Fielding, S. J., et al. In *Proceedings of the 28th EPS Conference on Controlled Fusion and Plasma Physics*, vol. 25A of *Europhysics Conference Abstracts*, pp. 1825–1828. 2001.

[49] Grosman, A., et al. In *Proceedings of the 28th EPS Conference on Controlled Fusion and Plasma Physics*, vol. 25A of *Europhysics Conference Abstracts*, pp. 209–212. 2001.

[50] Evans, T., et al. Nucl. Fusion, **48**, 024002 (2008).

[51] Fenstermacher, M. E., et al. Phys. Plasmas, **15**, 056122 (2008).

[52] Burrell, K. H., et al. Plasma Physics and Controlled Fusion, **47**, B37 (2005).

[53] Liang, Y., et al. Phys. Rev. Lett., **98**, 265004 (2007).

[54] Kirk, A., et al. Nuclear Fusion, **50**, 034008 (2010).

[55] Tamain, P., et al. Plasma Physics and Controlled Fusion, **52**, 075017 (2010).

[56] Temple, D., et al. In *Proceedings of the 36th EPS Conference on Plasma Physics*, vol. 33E of *Europhysics Conference Abstracts*, pp. P–5.191. 2009.

[57] Suttrop, W., et al. Fusion Engineering and Design, **84**, 290 (2009). Proceeding of the 25th Symposium on Fusion Technology - (SOFT-25).

[58] Rossel, J. X., et al. Plasma Physics and Controlled Fusion, **52**, 035006 (2010).

[59] Fitzpatrick, R. Nuclear Fusion, **33**, 1049 (1993).

[60] Fitzpatrick, R. Physics of Plasmas, **5**, 3325 (1998).

[61] Heyn, M. F., et al. Nuclear Fusion, **48**, 024005 (2008).

[62] Nardon, E., et al. Nuclear Fusion, **50**, 034002 (2010).

[63] Panek, R., et al. Czech. J. Phys., **56**, B125 (2006).

[64] Urban, J., et al. Czech. J. Phys., **56**, B176 (2006).

[65] Panek, R., et al. Physica Scripta, **72**, 327 (2005).

[66] Seidl, J., et al. The European Physical Journal D - Atomic, Molecular, Optical and Plasma Physics, **54**, 399 (2009).

[67] Krlin, L., Paprok, R., and Svoboda, V. The European Physical Journal D - Atomic, Molecular, Optical and Plasma Physics, **48**, 95 (2008).

[68] Abdullaev, S. S., Wingen, A., and Spatschek, K. H. Physics of Plasmas, **13**, 042509 (2006).

[69] Gobbin, M., et al. In *Proceedings of the 34th EPS Conference on Plasma Physics*, vol. 31F of *Europhysics Conference Abstracts*, pp. P–4.073. 2007.

[70] Mynick, H. E. Physics of Fluids B: Plasma Physics, **5**, 1471 (1993).

[71] Nardon, E. *Edge localized modes control by resonant magnetic perturbations*. Ph.D. thesis, Ecole Polytechnique (2007).

[72] Nardon, E., et al. J. Nucl. Mater., **363-365**, 1071 (2007).

[73] Bécoulet, M., et al. Nucl. Fusion, **45**, 1284 (2005).

[74] Bécoulet, M., et al. Nucl. Fusion, **48**, 024003 (2008).

[75] Abdullaev, S. S., et al. Phys. Plasmas, **15**, 042508 (2008).

[76] Riccardo, V., et al. *JET disruption studies in support of ITER* (2010). Accepted in Plasma Physics and Controlled Fusion.

[77] Freidberg, J. *Plasma physics and fusion energy*, chap. 9.6 runaway electrons, pp. 207–212. Cambridge university press, 2007.

[78] Smith, H. M., et al. Plasma Physics and Controlled Fusion, **51**, 124008 (2009).

[79] Hender, T., et al. Nuclear Fusion, **47**, S128 (2007).

[80] Helander, P., Eriksson, L.-G., and Andersson, F. Physics of Plasmas, **7**, 4106 (2000).

[81] Yoshino, R. and Tokuda, S. Nuclear Fusion, **40**, 1293 (2000).

[82] ITER Physics Expert Group on Disruptions, Plasma Control, and MHD and ITER Physics Basis Editors. Nuclear Fusion, **39**, 2251 (1999).

[83] Lehnen, M., et al. Phys. Rev. Lett., **100**, 255003 (2008).

[84] Riccardo, V. Fusion Science and Technology, **53** (2008).

[85] Riccardo, V. personal communication (2009).

[86] Rax, J., et al. *New ideas in tokamak confinement*, chap. Runaway dynamics in tokamaks, p. 154. American Institute of Physics, 1992.

[87] Wingen, A., et al. Nuclear Fusion, **46**, 941 (2006).

[88] Entrop, I., et al. Phys. Rev. Lett., **84**, 3606 (2000).

[89] Arnold, V. I. *Mathematical methods of classical mechanics*. Springer-Verlag, 1989.

[90] Wiggins, S. *Introduction to applied nonlinear systems and chaos*. No. 2 in Texts in Applied Mathematics. Springer-Verlag, New York Berlin Heidelberg, 1996.